The Theory and Computational Modelling of Ultra-Light Dark Matter

Emily Rose Carter Kendall

A thesis submitted in fulfilment of the requirements for the degree of Doctor of Philosophy in Physics, The University of Auckland, 2021.

Abstract

In this thesis I investigate the theory and computational modelling of ultra-light dark matter. The concept of dark matter arose when it was realised that astronomical observations were at odds with our understanding of gravity. In particular, it was noted that the motions of astrophysical objects could not be accounted for by the gravitational influence of visible matter alone. To explain astrophysical dynamics, it was inferred that invisible or 'dark' matter must also be present in the universe, and that it must account for the vast majority of all matter. Dark matter is now a widely accepted paradigm, however, a precise description of its nature remains elusive.

In the first part of this thesis I explore the theoretical fundamentals of ultra-light dark matter, highlighting crucial differences between this model and its competitors. I then focus on the computational modelling of ultra-light dark matter. I describe a simulation tool, PyUltraLight, developed to model the evolution of astrophysical objects within the ultra-light dark matter paradigm. I present applications of this tool on galactic scales, and use these results to support the idea that ultra-light dark matter may offer a better fit to data than its competitors. Following this, I model of the collapse of ultra-light dark matter overdensities in an expanding background using AxioNyx, a code that supports adaptive mesh refinement. Finally, I use these results to identify deviations between the predictions of the ULDM model and its competitors. I discuss how such differences may prove useful in assessing the ability of each model to accurately predict the properties of observed astrophysical objects.

Acknowledgements

I wholeheartedly thank my supervisor, Professor Richard Easther, for his unwavering support and encouragement. He has allowed me academic freedom and helped me immensely to develop as a physicist. I feel extraordinarily lucky to have undertaken a PhD under his supervision.

I thank my parents, Rosemary Carter and Brett Kendall, for their love and support through all of my endeavours. Words cannot express my gratitude for such wonderful parents and role models. I also thank my sisters, Rachel and Lisa, for being my best friends and my biggest fans. I'm incredibly proud to call them my sisters. I must also thank my brothers-in-law, Jonathan Devery and James McCracken, for supporting my sisters and for bringing joy into our lives every day.

I am extremely grateful to Jim Rea, for taking a chance on me all those years ago in London, and offering me a world of opportunities I could never have imagined. Many of my achievements over the past decade are a direct result of his support and encouragement, and I feel incredibly lucky to have such an inspiring role model and friend in my life.

Thanks to Elle Musoke and Ankita Gangotra for their wit and their wisdom. They welcomed me into their fold when I was a new PhD student, and sharing my PhD journey with them has been an enormous gift. Thanks also to Nathan Musoke and Max Waddellow.

An enormous thank you to Genevieve Fitzjames for looking after me in the final months of my PhD. She resolutely dedicated herself to making sure I got out of bed, making me coffee after coffee, forcing me to eat mandarins to stave off scurvy, proofreading, and much more. She provided the friendship and support I needed to finish my PhD when my motivation was waning most, and I am truly grateful.

A special thank you to Rebecca Llewellen for inspiring my passion for physics from a young age, and for truly making learning an enjoyable experience.

The support I have received from within the academic world has been invaluable. Thanks to Nathan Musoke, Lerh Feng Low, Mateja Gosenca, Lillian Guo, Frank Wang, Shaun Hotchkiss, Jens Niemeyer, Bodo Schwabe, Jan Eldridge, Luna Zagorac, Nikhil Padmanabhan, and many others.

I also acknowledge support from a University of Auckland Departmental Schol-

arship and the Marsden Fund of the Royal Society of New Zealand. The Nectar Research Cloud and New Zealand eScience Infrastructure (NeSI) have provided computing facilities necessary for this research. I have also made extensive use of open-source software such as Python, gnuplot, Matplotlib, NumExpr, NumPy, pyFFTW, SciPy, SymPy and yt [1, 2, 3, 4, 5, 6, 7, 8].

Contents

Use of copyrighted material

JCAP

The material in Chapter 3 was previously published in JCAP [9] and is copyright Institute of Physics Publishing and SISSA Medialab. It is used under the terms of the relevant assignment of copyright. In particular, section 3:

> **3. Author Rights**
>
> **3.1** IOP and SISSA Medialab Srl grant the Named Authors the rights specified in 3.2 and 3.3.
> **3.2.2** To include the Article (all or part) in a research thesis or dissertation.

PASA

The material in Chapter 4 was previously published in PASA [10] and is copyright Astronomical Society of Australia 2020. It is used under the terms of the relevant assignment of copyright. In particular:

> Reuse in a dissertation/thesis: License Not Required.
> Permission is granted at no cost for use of content in a Master's Thesis and/or Doctoral Dissertation.

Chapter 1

Introduction and Outline

1.1 Introduction

1.1.1 The Need for Dark Matter

In the field of cosmology, we attempt to understand the origins and evolution of the universe from the Big Bang to the present day. We strive to explain the constituents of the observable universe, their interactions and evolution within a self-consistent framework. The field of cosmology has grown enormously over the past several decades due to both theoretical progress and to the development of technologies which enable evermore detailed observations of the universe around us.

At the foundation of our cosmological framework is Einstein's General Theory of Relativity [11]. General Relativity describes the mechanism by which massive objects exert gravitational influence upon one another through the distortion of spacetime. This theory has stood up to rigorous testing [12, 13, 14], and has provided novel predictions such as gravitational waves and black holes, which have since been verified with advanced scientific experiments [15, 16].

While General Relativity does suffer problematic divergences (e.g. within black holes) and has yet to be unified with quantum field theory [17], its predictive success has lead to its wide acceptance as the standard framework of the gravitational interaction within modern cosmology. An important consequence of assuming the validity of General Relativity within cosmology is that it becomes necessary to in-

clude a mass component of the universe which does not interact electromagnetically. We refer to this component as dark matter. Indeed, there are now multiple lines of evidence that dark matter outweighs baryonic matter by a ratio of approximately 5:1 [18]. In many cases the predictions of General Relativity are indistinguishable from the predictions of the Newtonian limit, and it is worth noting that dark matter is also predicted by classical Newtonian gravity.

It is important to contrast this situation to models which attempt to avoid dark matter altogether through modifications to the gravitational interaction. Often referred to as MOND (Modified Newtonian Dynamics) [19], such models have not been able to convincingly resolve the dark matter problem at all scales [20, 21, 22]. As such, the prevailing view remains that General Relativity + dark matter is indeed the correct cosmological model.

While dark matter is, by definition, invisible, its presence can be inferred through a number of other observations across a variety of scales. One important source of evidence for dark matter comes from the study of galactic rotation curves [23]. In particular, observations of numerous galaxies have shown that the stellar rotational velocity remains relatively constant with increasing radial distance from the galactic centre [24, 25]. Indeed, even in the outermost regions with negligible luminosity, rotation speed does not appear to decrease with radial distance. This finding cannot be accommodated using visible matter alone, which is observed to be concentrated in the centre of the galactic halo. Instead, constant rotation curves imply an approximately spherical distribution of mass in the form of a dark matter 'halo', which extends much further than its visible counterpart and accounts for the majority of the galactic mass [26, 27].

Gravitational lensing, a prediction of General Relativity, provides further evidence of the existence of dark matter [28, 29]. Gravitational lensing refers to the distortion of spacetime by massive objects. This causes the path of photons from a distant source to an observer to deviate according to inhomogeneities in the mass distribution in the intervening space. Thus, images of distant bright sources contain an imprint of cosmic structure. Gravitational weak-lensing maps of large clusters of galaxies illustrate that the gravitational potential does not follow the distribution of the visible mass, providing evidence that these structures are dominated by dark matter [30, 31, 32]. In some extreme cases, the intra-cluster medium may even

disassociate entirely from the dark matter [33].

Yet another important source of evidence for the existence of dark matter comes from measurements of anisotropies in the cosmic microwave background [CMB] [34]. The CMB comprises the remnant radiation from the time in the early universe at which photons decoupled from baryonic matter and began to free-stream. Anisotropies in the CMB reflect overdense and underdense regions of the primordial plasma prior to decoupling. dark matter and baryonic matter would have behaved differently in this primordial plasma, as the former would have been unaffected by electromagnetic interactions with photons. This differing behaviour is expected to be imprinted upon the CMB, allowing the two matter components to be distinguished through the study of the CMB power spectrum. Indeed, such studies have convincingly demonstrated a density field dominated by dark matter [35, 36].

Taken together, galactic rotation curves, gravitational lensing surveys, and distortions in the CMB provide convincing evidence for the existence of a large dark component to the matter content of the universe. Problematically, however, the fact that this component does not interact electromagnetically does little to constrain its precise properties. Consequently, an array of widely varied dark matter models have been proposed in the past few decades, with predictions from each model then being tested against observations.

1.1.2 The Emergence of the CDM Paradigm

While the existence of dark matter is now widely accepted, the absence of dark matter signals from direct detection and collider experiments means that the precise nature of dark matter remains a mystery [37, 38, 39]. Nevertheless, both cosmological probes and particle physics experiments enable us to rule out some models, and tightly constrain others. I will now briefly review a range of possible dark matter candidates, and explain how the commonly accepted CDM paradigm has emerged as the dominant model of cosmology.

Models of dark matter may be categorised in a number of ways. For example, dark matter may be of either astrophysical or particulate origin. Examples of astrophysical dark matter include massive compact halo objects (MACHOs) [40, 41]

and primordial black holes [42, 43]. By contrast, examples of particulate dark matter include axions [44, 45], neutrinos [46], or supersymmetric partners to Standard Model particles [47, 48]. Such particle candidates for dark matter are often referred to as WIMPs (Weakly Interacting Massive Particles). This reflects the fact that while such particles do not interact electromagnetically, they do interact under gravity and may also undergo Weak interactions.

A further important categorisation of dark matter relates to energy scale. Candidates may be separated into 'hot', 'warm', or 'cold' categories, depending on their characteristic velocities. An example of a hot dark matter (HDM) candidate is the neutrino, travelling at velocities approaching the speed of light. By contrast, stable supersymmetric WIMP particles would travel much slower than the speed of light, and are thus considered cold dark matter (CDM). Warm dark matter (WDM) candidates such as light gravitinos exhibit intermediate behaviour.

As previously mentioned, any plausible dark matter model must yield theoretical predictions which are consistent with experimental bounds from a range of astrophysical measurements. CMB measurements are of great significance here. Anisotropies in the CMB have now been mapped to a high degree of precision, providing ever-tightening constraints on dark matter models [49, 50, 51].

Importantly, the latest CMB results disfavour HDM models in which neutrinos constitute the majority of the dark matter. The relative contribution of neutrinos to the energy density of the universe, $\Omega_\nu h^2$, is a function of the sum of the light neutrino masses [52]. The properties of the CMB power spectrum are sensitive to this value. For neutrinos to account for a substantial proportion of the dark matter, we would expect $\Omega_\nu h^2$ to be similar to the total matter contribution, $\Omega_m h^2$. However, CMB measurements from the PLANCK collaboration constrain the sum of the light neutrino masses to $\sum m_\nu < 0.54\text{eV}$ at the 95% confidence level, corresponding to $\Omega_\nu h^2 < 0.0057$. Meanwhile, PLANCK finds $\Omega_m h^2 = 0.1430 \pm 0.0011$ at the 68% confidence level [50]. Clearly, this discrepancy strongly disfavours neutrino based HDM models. Similar analyses of CMB data disfavour popular WDM models such as those based on light gravitinos.[1]

[1]It should be noted that these constraints are highly model-dependent. Here we assume a locally Lorentz invariant FRW cosmology [53]. In principle, more exotic cosmological models would change these constraints.

Consequently, with HDM and WDM models disfavoured, CDM has emerged as the dominant paradigm for dark matter. While there are a number of possible CDM candidates, supersymmetric partners to Standard Model particles are perhaps the most popular [54]. Specifically, models of supersymmetry in which the neutralino is the lightest stable supersymmetric particle (LSP) provide a natural WIMP dark matter candidate [55]. This model gained much attention due to the LSP WIMP candidate conveniently predicting the correct relic abundance to account for dark matter. This coincidence has historically been referred to as the 'WIMP Miracle'. Moreover, LSPs as WIMPs gained further popularity due to the plausibility of direct detection in experiments such as the Large Hadron Collider (LHC) [56].

Overall, therefore, CDM has emerged as the favoured model of dark matter, with plausible WIMP CDM candidates arising naturally from supersymmetric extensions to the Standard Model of particle physics. In the following sections, I will describe the successes of the CDM paradigm with respect to astrophysical predictions, and will also highlight the issues facing CDM which motivate the search for alternative dark matter models.

1.1.3 Successes of the CDM Paradigm in Astrophysics and Cosmology

In CDM models, structure formation proceeds hierarchically. That is to say, at the onset of the matter-dominated epoch, small overdensities in the primordial universe are able to break free from the expanding background and collapse first, and the resulting small halos then merge to form larger halos [57]. These larger halos then seed galaxy formation. This process endures until the epoch of dark energy domination [58], such that galaxy formation is an ongoing process rather than one limited to a short time period in the history of the universe. As the universe expands, collapse of CDM overdensities takes place on larger and larger scales. Therefore at late times, the characteristic halo mass is larger than at early times, such that the overall CDM distribution has no preferred mass scale [59]. That being said, baryonic physics prevents the formation of galaxies below a minimum mass scale or above a maximum scale [60]. The significance of the precise value of the minimum mass scales in particular will be discussed in Section 1.1.4.2.

A number of simulation tools exist with which to model CDM structure formation [61, 62, 63, 64]. When compared to astrophysical observations from collaborations such as the Sloane Digital Sky Survey (SDSS) [65], CDM simulations have performed remarkably well in reproducing the large scale filamentary structure and voids of the cosmic web [66, 67]. Moreover, the consistency of the CDM model with the results of CMB, galaxy clustering, and weak lensing surveys is well established [68, 69, 70]. Therefore, at cosmological scales, the CDM model has been shown to be remarkably consistent with data from a variety of observational probes. Such consistency at large scales has reinforced the popularity of the CDM paradigm. However, a number of issues arise for CDM on smaller, galactic scales. I shall address these issues in the following section.

1.1.4 Problems Facing the CDM Paradigm

1.1.4.1 Absence of Evidence from Direct Detection

While CDM models are able to consistently reproduce features of the large scale structure of the universe, the question remains as to the nature of the constituent WIMP particles. As previously mentioned, CDM gained in credibility due to the so-called 'WIMP miracle', whereby supersymmetry models apprently predicted the existence of an LSP with a relic abundance of the correct order of magnitude to account for the missing mass content of the universe [71, 72, 73, 74]. This was of great significance because the development of supersymmetry was not motivated by the need to identify a dark matter candidate. Instead, supersymmetry arose as an elegant solution to a number of unrelated problems within the Standard Model of particle physics. Namely, supersymmetry provides a framework in which the stark divide between bosons and fermions is naturally bridged and the light mass of the Higgs boson arises without fine-tuning [75, 76, 77]. Therefore, the fact that supersymmetry may also account for cosmological dark matter was seen by many as confirmation that it must indeed represent physical reality.

In previous decades, evidence of supersymmetry was expected to be readily accessible with the advent of advanced particle accelerators [78, 79]. However, after more than a decade of searching at the LHC, evidence of supersymmetry has yet to be found [80, 81, 82]. Moreover, a slew of non-accelerator based direct-

detection experiments have also failed to find evidence for an LSP CDM candidate [83, 84, 85, 86, 87].

The lack of evidence for any particle in the GeV-TeV energy range with a weak-scale cross-section with baryonic matter and the increasingly tight constraints on viable supersymmetry models [88, 89] motivate the consideration of alternative models of dark matter. The challenge, therefore, is identifying alternative models which reproduce the successful predictions of CDM on large scales while explaining the absence of direct detection evidence. This point will be revisited when I introduce ULDM in Section 1.1.5. However, before I discuss the ULDM alternative, I will briefly explicate the astrophysical problems also facing CDM.

1.1.4.2 The Small-Scale Crisis

While the CDM paradigm has been successful in reproducing the observed properties of large scale cosmological structure, there exist a number of apparent discrepancies at galactic scales and below. Collectively, these discrepancies are known as the 'small-scale crisis' [90, 91].

Perhaps the most studied of the small-scale controversies within CDM is known as the 'core-cusp' problem. This problem arises because CDM-only simulations tend to generate halos with central density profiles which sharply increase to a central 'cusp'. This feature is well-described by the semi-analytical Navarro-Frenk-White (NFW) profile [92]. Conversely, observations seem to favour a flatter central profile or 'core' [93, 94, 95]. Hence, this discrepancy is referred to as the core-cusp problem.

The core-cusp problem is a matter of significant debate, with a variety of solutions proposed which maintain the CDM framework. For example, it has been proposed that unsuitable mass estimators may have been used when analysing observational data, and that this leads to the erroneous detection of a core, when in reality there is indeed a cusp [96]. Others admit the existence of a core-cusp discrepancy when CDM-only simulations are compared to data, but contend that this situation is ameliorated when the effect of baryonic physics is taken into account [97, 98, 99]. While many possible remedies to the core-cusp problem have been proposed, it remains a topic of significant debate.

Another widely contested small-scale phenomenon is known as the 'missing

satellites problem' [100]. The hierarchical structure formation of CDM predicts that dark matter substructure should be prevalent on sub-galactic scales. Specifically, this model predicts that the Milky Way should contain $\sim$500 satellites of kpc scale within its virial radius [101]. However, observations show that the Milky Way contains far fewer satellites of this kind. The absence of significant substructure in observed galaxies has proven difficult to account for within the CDM framework. Nevertheless, a number of solutions to this apparent shortcoming of CDM have been proposed. For example, it has been proposed that low-mass CDM subhalos are prevented from producing significant stellar populations if they accrete most of their mass after the epoch of reionization. Under such conditions, the missing satellites problem appears to be ameliorated [102]. It has also been suggested that expectations of the number of observable satellites have been inflated by not correctly accounting for the detection efficiency of observational instruments and the luminosity of low-mass CDM subhalos [103]. Notwithstanding these various proposals for resolving the missing satellites problem, it remains a thorn in the side of existing CDM models and promotes the consideration of alternative models.

Yet another significant small-scale vulnerability of CDM is referred to as the 'too big to fail' problem [104, 105]. This refers to the fact that high resolution CDM galaxy simulations predict that galaxies with a stellar mass function similar to that of the Milky Way should host a number of intermediate mass systems large enough for significant star formation to occur. By contrast, however, such systems do not appear in observations. This indicates that if such intermediate systems really exist, they must have 'failed' to generate significant star formation, hence, 'too big to fail'. Note that this differs from the missing satellites problem, which concerns the lack of observed substructure at the smaller end of the mass function. As is the case with other aspects of the small-scale crisis, this issue is a matter of ongoing debate. Some contend, for example, that the assumed luminosity function which leads to the unobserved excesses of substructure is not valid due to gravitationally induced merging caused by classical dynamical friction [106]. Others contend that complex baryonic physics such as stellar feedback can resolve the apparent disparity between CDM simulations and observations [60]. However, recent research has lead to tighter constraints on satellite galaxy parameters, seemingly exacerbating the too big to fail problem and raising the bar for mechanisms proposed to alleviate

the problem [107].

Though the small-scale crisis of CDM is hotly contested, the lack of a single elegant framework in which all of its components are convincingly ameliorated is a strong motivator for exploring alternatives to CDM. In particular, models are sought which naturally alleviate the small-scale crisis without the need for complex baryonic physics but reproduce CDM predictions on large scales.

1.1.5 ULDM as an Alternative to CDM

In light of the unresolved problems within the CDM model, there is increasing motivation to search for alternatives which mitigate these problems, while also reproducing the successes of CDM. In particular, alternatives should reproduce the CDM predictions for the large scale structure of the universe, while simultaneously providing a natural solution to the small-scale crisis. Furthermore, they should explain the lack of direct-detection evidence and yet be well-motivated from a particle physics perspective. In this thesis, I will investigate ultra-light dark matter (ULDM) as an alternative to CDM. Here, I briefly outline the motivation behind the ULDM paradigm, with reference to the aforementioned successes and failures of CDM.

The fundamental ULDM hypothesis is that the constituent dark matter particle is a very light boson, with $m \sim 10^{-22}$eV [108]. The key advantage of such a dark matter candidate is that this extremely small mass corresponds to a kiloparsec scale de Broglie wavelength. As a result, structure formation on small scales is precluded by quantum uncertainty - as collapse proceeds past a certain point, increasing momentum opposes further particle confinement. Importantly, however, at scales much larger than the de Broglie wavelength, the dynamics of ULDM are indistinguishable from CDM [109]. Hence, ULDM presents a natural solution to the small-scale crisis, while retaining the successes of CDM at large scales.

Moreover, the concept of an extremely light boson appears in a number of scenarios in particle physics. Notably, the QCD axion, which resolves the Strong C-P problem, is one such example [44]. It has also been proposed that extremely light bosons could provide a resolution to the problem of lepton anomolous magnetic moments [110, 111]. As an ultra-light boson, ULDM provides a dark matter

candidate without recourse to supersymmetric extensions to the Standard Model. Furthermore, because of its extraordinarily small mass, the absence of direct detection is naturally explained. Indeed, particles of such small mass could only decay into photons with the decay rate scaling as the third power of the mass. Hence, signatures of such decay events would not be expected in instruments such as the LHC [112].

Overall, therefore, ULDM represents a well-motivated alternative to CDM, which may provide natural solutions to the small-scale issues of the latter. Meanwhile, the fact that ULDM and CDM predictions converge on large cosmological scales guarantee that this model provides a viable candidate to reproduce observations from probes of cosmological structure formation.

1.2 Outline

The following chapters in this thesis are dedicated to exploring the theory and computational modelling of ULDM, and analysing the plausibility of this model as an explanation of the mysterious dark matter component of the universe.

In Chapter 2, I review the fundamental theoretical background of the ULDM model of dark matter. I also introduce a number of astrophysical features of this model, which will be relevant to the content of later chapters. I then identify a number of open questions relating to the ULDM model, which will also be addressed in subsequent chapters.

In Chapter 3, I present the results of work already published in JCAP [9]. This work describes a simulation tool designed to solve the dynamical equations of the ULDM model using pseudo-spectral methods. This tool is called PyUltraLight. I discuss the features and limitations of PyUltraLight, and present a number of outputs serving as verification and efficiency tests. I also briefly review work which has since been completed by other research groups in which PyUltraLight has been adapted for a number of different numerical investigations.

In Chapter 4, I present the results of work already published in PASA [10]. This work addresses the aforementioned core-cusp problem of CDM, and makes use of astrophysical data from the SPARC database [113] to analyse whether ULDM or CDM models provide a better fit to the rotation curves of large dwarf galaxies.

Important in this analysis is the core-halo relationship of ULDM halos (introduced in Chapter 2). I also discuss the possibility of variability in this relationship.

In Chapter 5, I discuss material currently in preparation for publication. This work makes use of the AxioNyx simulation tool [114]. AxioNyx uses adaptive mesh refinement to allow for computationally efficient simulation of ULDM physics in an expanding background. I use this tool to study the collapse of aspherical overdensities to form ULDM halos. I discuss the process of relaxation and use these results to postulate mechanisms by which variability in the core-halo relationship of ULDM may arise. In particular, I address the phenomenon of soliton oscillation which is observed at late times in the collapse process and has important consequences for global properties of ULDM halos. I also use these simulation results to investigate the possibility of discerning ULDM signatures in the structure of the cosmic web through analysis of the anisotropic correlation functions of ULDM fields in which extended wavefronts are present.

In Chapter 6, I briefly highlight some ongoing work which is in the preliminary stages. This work concerns the study of angular momentum in ULDM halos formed by the collapse of rotating overdensities. I also consider statistical tools which may be applied to distinguish between ULDM and CDM density fields, based on the presence of extended anisotropic wavefronts in the former.

Finally, in Chapter 7 I summarise the results of this thesis and identify a number of avenues for future research in ULDM physics.

Chapter 2

Background and Literature Review

2.1 ULDM From First Principles

2.1.1 ULDM Candidates in Particle Physics

Within particle physics, the concept of symmetry plays an important role. The relationships and interactions of particles within the Standard Model are elegantly described using the mathematical framework of symmetry groups [115]. Because of this, physicists often look for fields which display obvious symmetries, as these fit naturally within the existing mathematical framework. Often, such symmetries are not exact, but are expected to be broken at some scale. A prototypical example of this is the phenomenon of neutrino oscillations. The existence of neutrino oscillations indicates the violation of lepton number conservation at a very low level [116]. Hence, a good place to start when considering possible new fields is with a model with an exact symmetry, and to then ask how this symmetry may be broken to a very small degree.

To see how ULDM fits into this framework, let us consider a massless, spinless field ϕ with no self-couplings. This field is described by the following action:

$$I = \frac{1}{2}\int d^4x\sqrt{-g}g^{\mu\nu}\partial_\mu\phi\partial_\nu\phi, \tag{2.1}$$

where g is the metric tensor. This field has an exact shift symmetry under $\phi \to \phi + C$, and is thus an attractive model from a particle physics perspective.

While the ULDM particle should be very light, it must not be precisely massless. Hence, rather than the action of Equation 2.1, we are interested in actions which reduce to Equation 2.1 in the limit that the mass approaches zero. In this way, ULDM may be considered a small deviation from a simple scalar field model with an exact shift symmetry.

An explicit example of such a ULDM model is represented by the following action:

$$I = \int d^4x\sqrt{-g}\left[\frac{1}{2}F^2 g^{\mu\nu}\partial_\mu\phi\partial_\nu\phi - m^2F^2\big(1-\cos(\phi)\big)\right]. \tag{2.2}$$

Here, ϕ is a dimensionless scalar field, which has a periodic shift symmetry of $\phi \to \phi + 2\pi$. Note that when the mass, m, is very small, Equation 2.2 approaches the form of Equation 2.1 and thus we realise a deeper, non-periodic, approximate shift symmetry. The constant F in Equation 2.2, where F has dimensions of mass, is required for dimensional consistency. This constant derives from the vacuum expectation value of the field, and is thus model-dependent. For most theoretical particle physics models, F is bounded below by the grand unified scale and above by the reduced Planck mass [117];

$$10^{16}\text{GeV} \lesssim F \lesssim 10^{18}\text{GeV}. \tag{2.3}$$

Spinless fields with a periodic shift symmetry arise naturally within a number of string theory models. Depending on the mass parameter, such fields may provide candidates for a number of cosmological phenomena including the inflaton field, dark energy, or the QCD axion [118]. In the present context of course, we are interested in a mass parameter m of the correct magnitude to describe dark matter. There have been various studies undertaken to constrain the ULDM particle mass via astrophysical observations, however, these constraints still remain a matter of ongoing debate. Most mass constraints favour $m \gtrsim 10^{-22}$eV [119, 120, 121]. Hence, I will use Equation 2.2 as the underlying particle physics model with a fiducial mass of 10^{-22}eV in the remainder of this thesis.

2.1.2 From Particle Physics to Cosmology

Let us now take a closer look at Equation 2.2, with $m = 10^{-22}$eV. It is necessary that this mass parameter yields a cosmological energy density of the correct magnitude to account for dark matter. Furthermore, the choice of $m = 10^{-22}$eV should yield a value of F consistent with the predictions of many theoretical models, as constrained by Equation 2.3.

To see how the field in Equation 2.2 evolves, let us apply the variational principle to obtain the equations of motion. The variation in the Lagrangian, $\mathcal{L}$, is given by:

$$\delta\mathcal{L} = \frac{\partial\mathcal{L}}{\partial\phi}\delta\phi + \frac{\partial\mathcal{L}}{\partial(\partial_\gamma\phi)}\delta(\partial_\gamma\phi), \tag{2.4}$$

such that the variation in the action is

$$\delta I = \int d^4x F^2\sqrt{-g}\Big[- m^2\sin(\phi)\delta\phi + g^{\mu\nu}\partial_\mu\phi\partial_\nu\big(\delta\phi\big)\Big] = 0, \tag{2.5}$$

where we have used $\partial_\nu(\delta\phi) = \delta(\partial_\nu\phi)$. Making use of the fact that

$$\sqrt{-g}g^{\mu\nu}\partial_\mu\phi\partial_\nu(\delta\phi) = \partial_\nu\Big[\sqrt{-g}g^{\mu\nu}\partial_\mu\phi\delta\phi\Big] - \partial_\nu\Big[\sqrt{-g}g^{\mu\nu}\partial_\mu\phi\Big]\delta\phi, \tag{2.6}$$

and noting that the volume integral of the total derivative is zero, we arrive at

$$\delta I = \int d^4x F^2\Big[- \sqrt{-g}m^2\sin(\phi) - \partial_\nu\big(\sqrt{-g}g^{\mu\nu}\partial_\mu\phi\big)\Big]\delta\phi = 0. \tag{2.7}$$

This yields the generalised equations of motion:

$$\frac{1}{\sqrt{-g}}\partial_\nu\big[\sqrt{-g}g^{\mu\nu}\partial_\mu\phi\big] + m^2\sin(\phi) = 0. \tag{2.8}$$

To relate these equations of motion to cosmology, let us now assume the metric tensor of an expanding Friedmann–Lemaître-Robertson–Walker (FLRW) universe in the post-inflationary epoch: [122]:

$$d\mathbf{s}^2 = -dt^2 + a(t)^2 d\mathbf{x}^2. \tag{2.9}$$

Further, let us assume that ϕ is constant across space, varying in time only. Making

use of the identity:

$$\partial_\nu \sqrt{-g} = \frac{1}{2}\sqrt{-g} g^{\alpha\beta} \partial_\nu g_{\alpha\beta}, \tag{2.10}$$

we arrive at the ULDM equations of motion for an FLRW universe [117]:

$$\ddot{\phi} + 3H(t)\dot{\phi} + m^2 \sin(\phi) = 0, \tag{2.11}$$

where $H(t) = \dot{a}/a$ is the Hubble constant and $\hbar = c = 1$.

Equation 2.11 indicates that for $H \gg m$, ϕ is approximately constant. When the ULDM field is established through symmetry breaking in the very early universe, H is indeed much larger than the ULDM mass and the field is therefore initially overdamped. Later, when $H \lesssim m$, the field begins to oscillate. The initial field value itself is governed by the details of the symmetry breaking mechanism, and is therefore model-dependent [123]. Typically, it is assumed that $\langle\phi\rangle \sim 1$, where ϕ is dimensionless, and m is as yet a free parameter.

For small field values $\phi \lesssim 1$, we can approximate the sine term in Equation 2.11 by the first Taylor series contribution [124]. While this approximation is not exact for the initial field, I will show that it becomes more accurate as the evolution proceeds. Hence, we may approximate Equation 2.11 by:

$$\ddot{\phi} + 3H(t)\dot{\phi} + m^2\phi = 0. \tag{2.12}$$

Let us assume an ansatz solution of $\phi(t) = A\cos(mt)$, where $A = A(t)$. Equation 2.12 may then be re-expressed as:

$$(\ddot{A} + 3H\dot{A})\cos(mt) - (3mHA + 2m\dot{A})\sin(mt) = 0. \tag{2.13}$$

This equation is automatically satisfied if both of the following conditions are met:

$$\text{Condition 1}: \quad 3HA = -2\dot{A} \tag{2.14}$$

$$\text{Condition 2}: \quad \ddot{A} = -3HA \tag{2.15}$$

Let us examine the first condition. Noting that $d(A^2)/dt = 2A\dot{A}$, this implies

$$\frac{d(A^2)}{dt} = -3HA^2. \tag{2.16}$$

We may integrate the above equation to obtain:

$$\int dt \frac{d(A^2)}{dt}\left(\frac{1}{A^2}\right) = \int dt \frac{da}{dt}\left(\frac{-3}{a}\right), \tag{2.17}$$

$$\therefore A^2 \propto a^{-3}. \tag{2.18}$$

This result is important for two reasons. First, we see that the energy density of the field, $\rho = m^2F^2A^2$, scales as a^{-3}. This is the same scaling property as conventional CDM [117], which is necessary if ULDM is to replicate CDM on large scales. Secondly, we see that the amplitude of the field oscillations are damped as $A \propto a^{-2/3}$. This means that approximating Equation 2.11 by Equation 2.12 becomes more accurate as expansion proceeds over time.

Let us now return to the second condition, $\ddot{A} = -3HA$. Substituting the first condition, $2\dot{A} = -3HA$, into the second, we find that the two are simultaneously satisfied if $\dot{H}A = \dot{A}H$, or, equivalently,

$$\dot{H} = \frac{-3H^2}{2}. \tag{2.19}$$

Proceeding as before, we can integrate this equation to obtain:

$$\int dt \frac{dH}{dt}\left(\frac{1}{H^2}\right) = \int dt \left(\frac{-3}{2}\right), \tag{2.20}$$

$$\therefore H \propto t^{-1}, \tag{2.21}$$

which is indeed what we expect, since $H \propto t^{-1}$ for any t^p where p is constant.[1]

[1]Note that while $H \propto \rho_{\text{crit}}^{1/2} \propto t^{-1}$ for both the radiation and matter dominated epochs, $\rho_{\text{crit}} \propto a^{-4}$ and $a \propto t^{1/2}$ for a radiation dominated universe, while $\rho_{\text{crit}} \propto a^{-3}$ and $a \propto t^{2/3}$ for a matter dominated universe.

Hence, we see that the ansatz solution $\phi = A\cos(mt)$ satisfies both conditions 2.14 and 2.15 (and thus Equation 2.12) when $A^2 \propto a^{-3}$. I now use this scaling behavior with $A_{t=0} \sim 1$ to compute an order of magnitude estimate of the parameter F and the current cosmological ULDM density.

To compute the value of F, we first note that in a radiation-dominated FLRW universe we have:

$$H^2 = \frac{8\pi}{3M_P^2}\rho, \quad \rho = \frac{\pi^2 g_e(T)}{30}T^4 \sim T^4, \tag{2.22}$$

where T is the photon temperature, M_P is the Planck mass, and $g_e(T)$ are the effective degrees of freedom for the energy density [125, 126]. Combining these expressions, we find that the ULDM field begins to oscillate when $H_{\text{osc}} \sim m$, or, roughly

$$T_{\text{osc}}^4 \sim m^2 M_P^2 \tag{2.23}$$

From Equations 2.22, we also have that the energy density of radiation at this time is of order T_{osc}^4. Meanwhile, the energy density of ULDM is of order m^2F^2. Letting ξ represent the ratio of ULDM energy density to radiation energy density, we have:

$$\xi_{\text{osc}} \sim \frac{m^2F^2}{T_{\text{osc}}^4}. \tag{2.24}$$

As expansion proceeds, this ratio grows as $1/T$ until radiation-matter equality at $T_{\text{eq}} \sim 1\text{eV}$. Hence, we find:

$$\frac{m^2F^2}{T_{\text{osc}}^4} \sim \frac{T_{\text{eq}}}{T_{\text{osc}}}. \tag{2.25}$$

Combining Equations 2.23 and 2.25 finally gives us an estimate of the parameter F:

$$F \sim \frac{T_{\text{eq}}^{1/2} M_P^{3/4}}{m^{1/4}} \sim 10^{17}\text{GeV}, \tag{2.26}$$

for $m = 10^{-22}\text{eV}$. Note that while we have obtained this value from astrophysical considerations, it conveniently lies within the theoretical acceptable range of Equation 2.3. This supports the notion of ULDM with the correct mass to account for dark matter arising naturally from a particle physics model.

I will now use this approximate value of F to compute an order of magnitude estimate of the current ULDM density (normalised by the critical density), $\Omega_{\text{ULDM},0}$. We note that $H_{\text{osc}}^2 \sim m^2$ and $H_{\text{eq}}^2 \sim T_{\text{eq}}^4/M_p^2$. Furthermore, we note that during the

matter dominated epoch we have $H \propto a^{-3}$, while during the radiation dominated era we have $H \propto a^{-4}$. Putting this together, we have:

$$\frac{H_0^2}{H_{\text{eq}}^2} = \frac{a_{\text{eq}}^3}{a_0^3}. \tag{2.27}$$

Assuming the present day scale factor $a_0 = 1$, this yields a value for the scale factor at matter-radiation equilibrium of

$$a_{\text{eq}}^3 \sim \frac{H_0 M_P^2}{T_{\text{eq}}^4}. \tag{2.28}$$

Analogously, we can compute the scale factor at the onset of the oscillation of the ULDM field through:

$$\frac{H_{\text{eq}}^2}{H_{\text{osc}}^2} = \frac{a_{\text{osc}}^3}{a_{\text{eq}}^3}. \tag{2.29}$$

Noting that $H_{\text{osc}} \sim m$ and substituting Equation 2.28 into the above, we find:

$$a_{\text{osc}}^3 \sim \left(\frac{T_{\text{eq}}^4}{M_p^2 m^2}\right)^{3/4} \frac{H_0^2 M_P^2}{T_{\text{eq}}^4}. \tag{2.30}$$

Finally, we use $\rho_{\text{ULDM},0} \sim m^2 F^2 A_0^2$ and $H_0^2 \sim \rho_{\text{crit},0}/M_P^2$ to obtain

$$\Omega_{\text{ULDM},0} \sim \frac{m^{1/2} F^2}{T_{\text{eq}} M_P^{3/2}}. \tag{2.31}$$

Substituting values $m \sim 10^{-22}$eV, $F \sim 10^{17}$GeV, $M_P \sim 10^{19}$Gev and $T_{\text{eq}} \sim 1$eV, this yields an order of magnitude estimate of

$$\Omega_{\text{ULDM},0} \sim \frac{(10^{-22})^{1/2}(10^{26})^2}{(10^{28})^{3/2}} = 0.1, \tag{2.32}$$

Which is indeed the correct order of magnitude to account for the observed dark matter density today [127]. While this is only a rough calculation, it serves to illustrate the viability of the ULDM model. Constraining the model parameters further is the subject of much ongoing research, and will be addressed in detail in the remainder of this thesis.

In summary, in this section I have demonstrated that the simple particle physics model of Equation 2.2 corresponds to a feasible ULDM candidate. This model is able to reproduce the expected cosmological dark matter density while simultaneously satisfying model-dependent particle physics constraints. In the next section, I will consider the dynamics of the ULDM field in a more general context, introducing perturbations around the FLRW metric necessary to seed structure formation.

2.2 ULDM Dynamics

In the previous section, I computed the average global evolution of the ULDM field in a homogeneous, isotropic FLRW universe. While we expect homogeneity and isotropy on large cosmological scales, this is not true in general on small scales. Indeed, local density variations in the early ULDM field are required to seed gravitational collapse and hence galactic structure formation.

In this section, we take into account local variations in the ULDM field. Because the ULDM field possesses mass, regions where the field value is large correspond to mass overdensities, while regions where the field value is small correspond to mass underdensities. We can take into account the presence of these density variations by introducing space and time dependent perturbations to the FLRW metric of an expanding universe. This will lead to modified equations of motion for ULDM, which will form the theoretical basis for simulation tools designed to model structure formation and dynamics.

We begin with the generalised equations of motion for the ULDM field, given in Equation 2.8. As discussed in the previous section, we may approximate the sinusoidal component by the leading order term of its Taylor expansion, with this approximation approaching the exact expression as the universe expands. Hence, we have:

$$\frac{1}{\sqrt{-g}}\partial_\nu\left[\sqrt{-g}g^{\mu\nu}\partial_\mu\phi\right] + m^2\phi = 0. \tag{2.33}$$

We now evaluate the above expression using the perturbed FLRW metric,

$$d\mathbf{s}^2 = -(1+2\Phi)dt^2 + a^2(1-2\Phi)d\mathbf{x}^2, \tag{2.34}$$

where $\Phi = \Phi(\mathbf{x}, t)$ is a small perturbation and $a = a(t)$. Because Φ is assumed to be small, we proceed only to linear order in Φ in our analysis. It is helpful to first employ the identity 2.10 re-express Equation 2.33 as:

$$\frac{1}{2}g^{\alpha\beta}(\partial_\mu g_{\alpha\beta})g^{\mu\nu}\partial_\nu\phi + \partial_\mu(g^{\mu\nu}\partial_\nu\phi) - m^2\phi = 0. \tag{2.35}$$

We will now examine each of the three terms in the summation separately. The first term may be written in the following expanded form:

$$\begin{aligned}\frac{1}{2}\Big[&g^{0\beta}(\partial_0 g_{0\beta})g^{0\nu}\partial_\nu\phi + g^{0\beta}(\partial_i g_{0\beta})g^{i\nu}\partial_\nu\phi \\ &+ g^{i\beta}(\partial_0 g_{i\beta})g^{0\nu}\partial_\nu\phi + g^{i\beta}(\partial_j g_{i\beta})g^{j\nu}\partial_\nu\phi\Big],\end{aligned} \tag{2.36}$$

where indices i and j run between 1 and 3 only while Greek indices run from 0 to 3. Because we are expanding to linear order in Φ, it is useful to obtain approximate expressions for the components of the inverse metric tensor as follows:

$$g^{00} = \frac{-1}{1+2\Phi} = -\sum_{n=0}^{\infty}(-2\Phi)^n \approx -(1-2\Phi), \tag{2.37}$$

$$g^{ii} = \frac{1}{a^2(1-2\Phi)} = \frac{1}{a^2}\sum_{n=0}^{\infty}(2\Phi)^n \approx \frac{1}{a^2}(1+2\Phi). \tag{2.38}$$

Using these expressions, we find:

$$g^{0\beta}(\partial_0 g_{0\beta})g^{0\nu}\partial_\nu\phi \approx -(1-2\Phi)\partial_0(-1-2\Phi)(-1+2\Phi)\partial_0\Phi, \tag{2.39}$$

$$g^{0\beta}(\partial_i g_{0\beta})g^{i\nu}\partial_\nu\phi \approx -(1-2\Phi)\partial_i(-1-2\Phi)\frac{1}{a^2}(1+2\Phi)\partial_i\phi, \tag{2.40}$$

$$g^{i\beta}(\partial_0 g_{i\beta})g^{0\nu}\partial_\nu\phi \approx \frac{3}{a^2}(1+2\Phi)\partial_0(a^2(1-2\Phi))(-1+2\Phi)\partial_0\phi, \tag{2.41}$$

$$g^{i\beta}(\partial_j g_{i\beta})g^{j\nu}\partial_\nu\phi \approx \frac{3}{a^2}(1+2\Phi)\partial_j(a^2(1-2\Phi))\frac{1}{a^2}(1+2\Phi)\partial_j\phi \tag{2.42}$$

where factors of 3 come from summing over indices i and j. Keeping terms to linear order in Φ only, we find that the first term of Equation 2.35 reduces to:

$$2\dot{\Phi}\dot{\phi} - \frac{2}{a^2}\partial_i\Phi\partial_i\phi - 3H(1-2\Phi)\dot{\phi}, \tag{2.43}$$

where $H = \dot{a}/a$. Working in a similar fashion to examine the second term in Equation 2.35, we have:

$$\partial_\mu(g^{\mu\nu}\partial_\nu\phi) = \partial_0(g^{0\nu}\partial_\nu\phi) + \partial_i(g^{i\nu}\partial_\nu\phi) \tag{2.44}$$

$$\approx \partial_0\big(-(1-2\Phi)\dot{\phi}\big) + \frac{1}{a^2}\partial_i\big((1+2\Phi)\partial_i\phi\big). \tag{2.45}$$

Again, keeping only terms to first order in Φ, we obtain

$$-\ddot{\phi}(1-2\Phi) + 2\dot{\Phi}\dot{\phi} + \frac{2}{a^2}\partial_i\Phi\partial_i\phi + \frac{1}{a^2}(1+2\Phi)\nabla^2\phi. \tag{2.46}$$

Putting together Equations 2.43 and 2.46 with the final $-m^2\phi$ term we find that, to linear order in Φ, Equation 2.35 reduces to:

$$-\ddot{\phi}(1-2\Phi) + 4\dot{\Phi}\dot{\phi} - 3H(1-2\Phi)\dot{\phi} + \frac{1}{a^2}(1+2\Phi)\nabla^2\phi - m^2\phi = 0. \tag{2.47}$$

We can simplify this expression by dividing through by $-(1-2\Phi)$ and again discarding higher orders in Φ:

$$\ddot{\phi} + 3H\dot{\phi} - 4\dot{\Phi}\dot{\phi} - \frac{1}{a^2}(1+4\Phi)\nabla^2\phi + m^2(1+2\Phi)\phi = 0. \tag{2.48}$$

From here, we must make some assumptions about the nature of the ULDM field ϕ and the gravitational potential Φ. Namely, we assume that both ϕ and Φ are slowly varying in space and time. Specifically:

$$|\dot{\phi}| << m|\phi|, \tag{2.49}$$

$$|\dot{\Phi}| << m|\Phi|, \tag{2.50}$$

$$|\nabla\phi| << m|\phi|, \tag{2.51}$$

where the final assumption also implies $|\nabla^2\phi| << m^2|\phi|$. Furthermore, at late times in an expanding universe, $H << m$ and $a \sim 1$. Combining these assumptions, we are able to neglect a number of terms in Equation 2.48 and obtain, for a slowly varying field at late times:

$$\ddot{\phi} - \nabla^2\phi + m^2(1+2\Phi)\phi = 0. \tag{2.52}$$

We may solve this using Wentzel–Kramers–Brillouin (WKB) methods, employing the following ansatz solution:

$$\phi = \frac{1}{\sqrt{2}m}\left(\psi e^{-imt} + \psi^* e^{imt}\right). \tag{2.53}$$

Like ϕ, ψ is assumed to be slowly varying. Therefore, ψ satisfies the same conditions as ϕ in Equations 2.49 and 2.51. Hence, we may directly substitute the ansatz solution into Equation 2.52 while neglecting highly suppressed terms. The outcome of this process is an equation in ψ:

$$i\dot{\psi} = \frac{-\nabla^2\psi}{2m} + m\Phi\psi. \tag{2.54}$$

Note that throughout this derivation we have suppressed factors of $\hbar$, assuming $\hbar = c = 1$. Restoring factors of $\hbar$, we recover the well-known Schrödinger Equation of non-relativistic quantum mechanics:

$$i\hbar\dot{\psi} = \frac{-\hbar^2}{2m}\nabla^2\psi + m\Phi\psi. \tag{2.55}$$

Hence, in the late universe, the ULDM field may be described by the macroscopic wavefunction ψ of a Bose-Einstein condensate. It follows that the particle number density is $|\psi|^2$, so that the mass density is $m|\psi|^2$. The gravitational potential, which is sourced by the field itself, then satisfies the Poisson equation:

$$\nabla^2\Phi = 4\pi G m|\psi|^2, \tag{2.56}$$

Where G is Newton's gravitational constant.

Overall, therefore, the dynamics of ULDM at late times may be conveniently described by the coupled Schrödinger-Poisson (Schrödinger-Poisson) differential equations. It is this system of equations which will form the foundation of the simulation tools discussed in the remainder of this thesis.

In deriving Equation 2.52, we neglected terms in H since $H << m$. We also assumed $a \sim 1$ since we are primarily concerned with the dynamics of ULDM at late times. These turn out to be suitable assumptions even at relatively high redshifts, and Equation 2.52 provides a good description of ULDM dynamics

throughout the process of structure formation. While neither Equation 2.52 nor the Schrödinger-Poisson system depend explicitly on H or a, this does not mean the dynamics are insensitive to expansion. To see how expansion influences the dynamics, we may re-cast the Schrödinger-Poisson equations in terms of comoving coordinates. To do this, we note that the Schrödinger-Poisson equations may be obtained directly from the following action:

$$S = \int dt \int d^3x \big[\mathcal{L}\big] = \int dt \int \frac{d^3x}{2} \Big[i(\psi^* \dot{\psi} - \psi \dot{\psi}^*) + m^{-1} (\nabla \psi)^2 - 2m\Phi |\psi|^2 \Big]. \quad (2.57)$$

We first note that:

$$(\nabla \psi)^2 = \nabla(\psi^* \nabla \psi) - \psi^* \nabla^2 \psi. \quad (2.58)$$

Within the action integral, the $\nabla(\psi^* \nabla \psi)$ term corresponds to the integral of a total derivative, and may therefore be ignored, hence, we have:

$$S = \int dt \int \frac{d^3x}{2} \Big[i(\psi^* \dot{\psi} - \psi \dot{\psi}^*) - m^{-1} \psi^* \nabla^2 \psi - 2m\Phi |\psi|^2 \Big]. \quad (2.59)$$

In comoving coordinates, this becomes

$$S = \int dt \int \frac{a^3 d^3x}{2} \Big[i(\psi^* \dot{\psi} - \psi \dot{\psi}^*) - m^{-1} a^{-2} \psi^* \nabla^2 \psi - 2m\Phi |\psi|^2 \Big], \quad (2.60)$$

where now $x = x_{\rm com}$ and $\nabla = \nabla_{\rm com}$. Applying the variational principle,

$$\frac{\partial \mathcal{L}}{\partial \psi^*} - \frac{d}{dt} \frac{\partial \mathcal{L}}{\partial \dot{\psi}^*} = 0, \quad (2.61)$$

we find:

$$\frac{1}{2} \Big(2i\dot{\psi} a^3 - a m^{-1} \nabla^2 \psi - 2a^3 m \Phi \psi + 3i a^2 \dot{a} \psi \Big) = 0, \quad (2.62)$$

while the Poisson equation in comoving coordinates is:

$$\nabla^2 \Phi = 4\pi G m a^2 |\psi|^2. \quad (2.63)$$

Let us now introduce $\tilde{\psi} = a^{3/2}\psi$ such that Equation 2.62 becomes:

$$i\dot{\tilde{\psi}} = \frac{\nabla^2\tilde{\psi}}{2ma^2} + m\Phi\psi \tag{2.64}$$

and the Poisson equation becomes:

$$\nabla^2\Phi = \frac{4\pi Gm}{a}|\tilde{\psi}|^2. \tag{2.65}$$

Note that the physical density is then $\rho = m|\psi|^2 = ma^{-3}|\tilde{\psi}|^2$. Equations 2.64 and 2.65 therefore form the comoving Schrödinger-Poisson system, which will be useful in later sections when simulating ULDM dynamics in an expanding background.

2.3 Astrophysics of ULDM and Open Questions

In this section, I briefly discuss some astrophysical constraints relevant to ULDM, and outline the key astrophysical problems that ULDM has been proposed to solve. I will then investigate whether the ULDM model does indeed provide a convincing solution to these problems using numerical methods in later sections.

2.3.1 The ULDM Halo Profile

In recent years, structure formation simulations have revealed a characteristic profile for ULDM halos. Typical halos consist of a smooth, coherent core embedded in an incoherent outer halo possessing granular density fluctuations [128, 129, 130]. The density profile of the inner core closely matches that of the ground state solution to the Schrödinger-Poisson differential equations [131]. This ground-state solution is often referred to as a soliton, and has a smooth, flat density profile at zero radius. Meanwhile, the average shape of the outer density profile is consistent with the NFW profile of CDM for which $\rho \propto 1/r^3$ at large radii.

The NFW profile is characterised by the following expression [92]:

$$\rho_{\rm NFW}(r) = \frac{\rho_0}{\frac{r}{R_s}\left(1+\frac{r}{R_s}\right)^2}, \tag{2.66}$$

where ρ_0 and R_s are free parameters, which vary from halo to halo. Meanwhile, the solitonic profile is well-approximated by [132]:

$$\rho_{\rm sol}(r) = \frac{\rho_c}{\left(1 + 0.091\left(\frac{r}{r_c}\right)^2\right)^8}. \tag{2.67}$$

Here, ρ_c is the density at $r = 0$, given by

$$\rho_c = 1.9 \times 10^7 a^{-1} m_{22}^{-2} \left(\frac{r_c}{\rm kpc}\right)^{-4} M_\odot {\rm kpc}^{-3}, \tag{2.68}$$

where a is the cosmological scale factor, r_c is the radius at half-maximum density, and $m_{22} = m/10^{-22}$eV.

Hence, the ULDM profile is often described piecewise, using $\rho_{\rm sol}$ in the centre and $\rho_{\rm NFW}$ at large radii. The transition between these two regions appears to be governed by a universal core-halo mass relation [133]:

$$\frac{M_c}{M_h} = 5.04 \times 10^{-2} \left(\frac{M_h}{10^9 M_\odot}\right)^{-2/3} m_{22}^{-1}, \tag{2.69}$$

where $M_h = (4\pi r_{\rm vir}^3/3)\zeta(z)\rho_{\rm crit}$ is the virial mass of the halo with $\zeta(z) = (18\pi^2 + 82(\Omega_m(z) - 1) - 39(\Omega_m(z) - 1)^2)/\Omega_m(z) \sim 200$ [134], and M_c is the mass within radius r_c. This core-halo mass relation may be alternatively expressed as [132]:

$$r_c = 1.6 a^{1/2} \left(\frac{\zeta(z)}{\zeta(0)}\right)^{-1/6} \left(\frac{M_h}{10^9 M_\odot}\right)^{-1/3} m_{22}^{-1} \text{ kpc}. \tag{2.70}$$

The existence of a smooth core in ULDM halos has been proposed as a natural solution to the core-cusp problem introduced in Section 1.1.4.2. However, it is important to note that the mass of the soliton within r_c scales inversely with the radius. That is to say, heavier solitons tend to be much more 'peaked' than their lighter counterparts. Given this scaling property and the apparent core-halo mass relation, it has been suggested that in certain regimes, the ULDM profile may actually exacerbate the core-cusp problem relative to CDM [133]. This claim will be investigated in Chapter 4, while the universality of the core-halo mass relation

will also be addressed in Chapter 5.

2.3.2 Upper and Lower bounds on ULDM halos

There are a number of constraints governing the formation of realistic astrophysical ULDM halos. These constraints arise due to the scale invariance of the Schrödinger-Poisson equations, discussed in detail in Appendix A. Succinctly, if a spherically symmetric eigenstate of the Schrödinger-Poisson equations is found for an object of a particular mass, an entire family of solutions may be automatically constructed, parametrised by mass alone. In the following sections, we will use numerical solutions of the Schrödinger-Poisson system to derive constraints on ULDM halo parameters.

2.3.2.1 Minimum ULDM halo radius

To see how the scaling properties of the Schrödinger-Poisson system give rise to constraints on ULDM halos, one first numerically computes the density profiles of the spherically symmetric solutions to the Schrödinger-Poisson equations for a given mass M [135, 136, 137, 138]. Each solution corresponds to a spherically symmetric eigenstate, which we will index n. For each eigenstate, one may then obtain values for the half-mass radius, $r_{1/2}$, and the central density, ρ_c, for any value of M. The values of $r_{1/2}$ and ρ_c corresponding to the ground state solution then represent bounds on the radius and central density of excited states for the same mass M. Namely, we find [117]:

$$r_{1/2} = \frac{\hbar^2}{GMm^2} f_n \geq 0.335 \text{ kpc} \left(\frac{10^9 M_\odot}{M}\right) m_{22}^{-2}, \tag{2.71}$$

$$\rho_c = \left(\frac{Gm^2}{\hbar^2}\right)^3 M^4 \rho_n \leq 7.05 \ M_\odot \text{pc}^{-3} \left(\frac{M}{10^9 M_\odot}\right)^4 m_{22}^6, \tag{2.72}$$

where M is the total mass of the object, and f_n and ρ_n are eigenstate-dependent constants. For the lowest energy solution (f_0, ρ_0), the inequalities become equalities, and thus constitute bounds on the halo parameters.

Equations 2.71 and 2.72 may be used to test ULDM predictions against astrophysical observations, however, there are a number of caveats to this approach.

While simulations suggest that typical ULDM halos possess a spherically symmetric 'core', the above inequalities assume the the spherically-symmetric solution represents the entire mass of the object. For large ULDM halos, one expects a generic halo profile with a small core residing within a larger, incoherent outer halo. This outer halo is not, in general, spherically symmetric and therefore does not represent one of the eigenstates discussed above. Hence, these inequalities are most useful for small astrophysical objects, where the spherically symmetric core dominates according to Equation 2.69. Furthermore, baryonic physics is not considered in deriving the above equalities. Hence, they should only be applied in situations where the mass to light ratio is high. An example of a suitable test regime is the dwarf spheroidal galaxies of the Local Group with mass-to-light ratios $\geq 100 M_{\odot}/L_{\odot}$. One such study of 36 of these dwarf spheroidals ([139]) yields results consistent with Equations 2.71 and 2.72 for $m \approx 10^{-22} eV$ and $M \gtrsim 3 \times 10^{8} M_{\odot}$, however further studies are required to provide a convincing agreement.

2.3.2.2 Minimum ULDM halo mass

The inverse mass-radius scaling behaviour of the Schrödinger-Poisson system, as shown in Equation 2.71, has further physical consequences. In addition to constraining the half-mass radius for a ULDM halo of total mass M, Equation 2.71 may also be used to derive a lower bound on the value of M. To see this, we make use of yet another relation arising from the numerical solutions to the Schrödinger-Poisson system, in this case constraining the virial velocity, v_{vir}:

$$v_{\mathrm{vir}}^2 = \frac{G^2 M^2 m^2}{\hbar^2} \omega_n, \tag{2.73}$$

where similarly to Equations 2.71 and 2.72, ω_n is a constant whose value depends on the eigenstate n. Specifically, we find that ω_n decreases for increasing n, with $\omega_n < \omega_0 \approx 0.1$.

We also note that gravitational collapse only occurs in the presence of an overdensity, meaning that the region within a virialised ULDM halo must have higher density than the average density of the universe. It is typical to assume that the average internal density within the virial radius is a multiple of the critical

density [140]:

$$\bar{\rho}_{\rm vir} = 200\rho_{\rm crit} = 200\left(\frac{3H^2}{8\pi G}\right). \tag{2.74}$$

While Equations 2.73 and 2.74 constrain the virial velocity and the virial overdensity, we may also constrain the virial radius of a ULDM halo by noting that, as a consequence of the repulsive nature of the quantum pressure at small scales, the virial radius must be larger than the de Broglie wavelength of the ULDM constituent particle. Specifically [117]:

$$r_{\rm vir} \gtrsim \frac{\lambda_{\rm dB}}{2\pi} = \frac{\hbar}{m v_{\rm vir}}. \tag{2.75}$$

Combining Equations 2.73 and 2.75 we find:

$$r_{\rm vir} \gtrsim \frac{\hbar^2}{GMm^2}\omega_n^{-1} \geq 3.2\frac{\hbar^2}{GMm^2}, \tag{2.76}$$

where we have used the ground state value $\omega_0 = 0.1$ in the second inequality. Comparing this result to 2.71, where $f_0 = 3.9$, we see that this implies that for the smallest halos, $r_{\rm vir} \approx r_{1/2}$. Consequently, $\bar{\rho}_{\rm vir} \approx \bar{\rho}_{1/2}$ and $M_{\rm vir} \approx M_{1/2} = 1/2M$. Hence, equating $\bar{\rho}_{1/2}$ with Equation 2.74, we have:

$$200H^2 r_{1/2}^2 = MG, \tag{2.77}$$

and substituting Equation 2.71 for $r_{1/2}$ we find:

$$M \gtrsim 10\frac{H^{1/2}\hbar^{3/2}}{Gm^{3/2}} = 5\times10^7 M_\odot \left(\frac{H}{70{\rm kms}^{-1}{\rm Mpc}^{-1}}\right)^{1/2} m_{22}^{-3/2}, \tag{2.78}$$

corresponding to a minimum virial mass of $M_{\rm vir} \approx M_{1/2} = 1/2M = 2.5\times10^7 M_\odot$. In contrast to CDM models, where a large number of subhalos with masses below $10^8 M_\odot$ are expected, the above limit indicates that dark matter subhalos around globular clusters or ultra-compact dwarf galaxies are not expected [141]. Hence, ULDM seems to naturally provide a resolution to the missing satellite problem introduced in Chapter 1.

2.3.2.3 Maximum ULDM halo mass

Just as the scaling properties of the Schrödinger-Poisson equations naturally give rise to a minimum halo mass, they also give rise to a maximum halo mass. Consider Equation 2.71 for the half-mass radius $r_{1/2}$. We now ask what value of $M_{1/2}$ contained within this radius would correspond to $r_{1/2}$ approaching the Schwarzschild radius, r_S. That is:

$$r_S = \frac{2GM_{1/2}}{c^2} = \frac{\hbar^2}{GMm^2} f_n. \tag{2.79}$$

Since $2M_{1/2} = M$, this equation can easily be rearranged to show that the Schwarzschild radius is equal to the half-mass radius when

$$M = \frac{\hbar c}{Gm}\sqrt{f_n}. \tag{2.80}$$

Taking the ground state soliton solution $f_n = f_0 \approx 3.9$ this gives:

$$M_{\max} \approx 2.67 \times 10^{12} M_\odot m_{22}^{-1}. \tag{2.81}$$

Above this mass, a black hole would be expected to form. Note that this calculation corresponds only to a constraint on the mass of a soliton. As previously mentioned, large astrophysical ULDM halos are not well-described by the soliton solution alone, but rather a central solitonic core surrounded by a much larger incoherent outer halo. Hence, the maximum ULDM halo mass will be much larger than the upper limit on the central core. This maximum halo mass depends on the core-halo relation discussed previously. Therefore, let us now combine the core-halo relation with the upper bound on the soliton mass and compare our results to observations.

The largest observed astrophysical dark matter halos are associated with rich galaxy clusters and have masses approaching $2 \times 10^{15} M_\odot$ [32, 142]. Taking into account the apparent core-halo mass relation of Equations 2.69 and 2.70 and the fact that $r_{1/2} \sim 1.45 r_c$ [132], at $z \sim 1$ this corresponds to $r_{1/2} \sim 0.0184$kpc and consequently:

$$M_{\max}(\text{observed}) \sim 1.8 \times 10^{10} M_\odot m_{22}^{-2}, \tag{2.82}$$

which is well below the limit set by Equation 2.81. Hence, we see that the astrophysical constraints imposed by the scaling relations of the Schrödinger-Poisson

system are consistent with the observations of the largest observed cosmological structures.

Note, however, that the core-halo relation employed above has not been shown to be universal. That is to say, it is not yet clear whether the core-halo mass relation (which was determined from simulations of small to medium halos) can be extrapolated to the largest ULDM halos. Indeed, the possibility of variability in the core-halo relation will be investigated later in this thesis.

2.3.3 Open Questions

While the preceding section outlines the foundations of the astrophysics of ULDM, there are a number of outstanding questions yet to be resolved. It is the purpose of the remainder of this thesis to develop tools with which to address some of these questions, which I will now briefly summarise.

2.3.3.1 Tools for the simulation of ULDM

In order to understand the complicated dynamics of ULDM in an astrophysical context, it is necessary to develop computational tools capable of modelling this behaviour. Importantly, such tools need to be able to capture quantum effects unique to ULDM. For this reason, n-body simulators traditionally employed in the case of CDM are unsuitable. In Chapters 3, and 5 of this thesis I will introduce a number of tools designed to model ULDM dynamics governed by the Schrödinger-Poisson system. These include PyUltraLight, chplUltra, and AxioNyx.

2.3.3.2 Can ULDM solve the core-cusp problem?

It has been predicted that the core-cusp problem introduced in Section 1.1.4.2 may be ameliorated in ULDM due to the quantum pressure preventing collapse at the centre of a ULDM halo. However, because of the scaling properties of ULDM, the radius of a ULDM core scales inversely with mass. It is important to understand the effect this has at astrophysically observable scales, as it is feasible that in some regimes the ULDM density may indeed exceed CDM density at the same radius. This question will be addressed in Chapter 4.

2.3.3.3 Dynamics of interacting ULDM halos

In the context of cosmological structure formation, it is expected that as the universe evolves, DM halos will merge to form larger objects. The details of this merger process in the ULDM model are not yet well-understood, and are expected to differ from CDM mergers through the presence of macroscopic quantum interference effects. Mergers will be addressed in Chapter 3 of this thesis.

2.3.3.4 Variability in the core-halo mass relation

As described in Section 2.3.1, simulations of ULDM halos tend to favour a composite halo structure consisting of a central solitonic core surrounded by an incoherent outer halo. There appears to be a relationship (Equations 2.69, 2.70) between the relative masses of these contributions to the overall halo, but whether this relationship may be extrapolated across a wide range of mass scales is not yet known. Furthermore, as this relationship is drawn from a statistical average over a number of simulated halos, it is expected that there will be a certain variance around the theoretical value for any given halo. Factors which may lead to deviations from the theoretical value are not yet well-understood, and in Chapter 5 of this thesis I will address evidence indicating that the core-halo relationship may be violated to some extent in certain regimes.

2.3.3.5 Characterisation of the solitonic core of ULDM halos

While it has been observed through simulations that ULDM halos tend to possess an inner core resembling the ground-state (soliton) solution to the Schrödinger-Poisson system, it is of interest to explore parameters other than the spherically-averaged density profile of this region in order to establish the extent to which a solitonic description is applicable. For example, one may expect that asphericities in an initial overdensity, which collapses to form a ULDM halo, may be imprinted in the final structure. One may also expect that angular momentum may lead to non-trivial velocity distributions in the core, differing from the characteristic internal velocity field of a true soliton. It is also necessary to understand the broader dynamics of the core region as relaxation occurs following collapse, particularly any oscillatory effects. These questions will be addressed in Chapter 5.

2.3.3.6 Other observable signatures of ULDM

In addition to characteristic density profiles of ULDM halos, it is useful to look for other potentially observable effects which may serve as signatures of the ULDM model. In particular, the wave-like behaviour of ULDM on scales similar to the de Broglie wavelength may lead to observable interference effects in some regimes. The presence of such interference effects and statistical methods to analyse them are discussed in Chapters 3 and 5.

Chapter 3

PyUltraLight: A Pseudo-Spectral Solver for ULDM Dynamics

This chapter is an adaptation of

Faber Edwards, Emily Kendall, Shaun Hotchkiss, Richard Easther
PyUltraLight: A Pseudo-Spectral Solver for Ultralight Dark Matter Dynamics
JCAP No. 10 (2018) [9]

3.1 Introduction

As discussed in Chapters 1 and 2, CDM has been the prevailing model of dark matter for at least the past two decades. This describes a cosmology with simple, pressureless, noninteracting dark matter comprised of WIMPs. This model, however appears to be at odds with observations at small astrophysical scales [143]. The potential shortcomings of simple CDM scenarios motivate investigations of more novel dark matter scenarios. In particular, ultra-light dark matter (ULDM), is an increasingly well-studied possibility.[1]

As also discussed Chapters 1 and 2, ULDM models are motivated by fundamental

[1]ULDM is also variously known as fuzzy dark matter (FDM), BEC dark matter, scalar field dark matter (SFDM), axion dark matter, and Ψ dark matter.

theories possessing approximate shift symmetries [144, 123]. Moreover, ULDM may naturally resolve the small-scale problems of ΛCDM as the Heisenberg uncertainty principle suppresses gravitational collapse on length scales shorter than the de Broglie wavelength of the ULDM particle. In this regime the mass of the ULDM particle becomes correlated with astrophysical observables; if it is of order 10^{-22} eV, structure is suppressed at kiloparsec scales and below [108].

Given the presence of a fundamental lengthscale, the behaviour of ULDM is more complex than that of simple dark matter scenarios whose cosmologically relevant interactions are purely gravitational. Physically, the effective short-scale pressure and condensate-like properties of ULDM create new dynamical possibilities for ULDM scenarios, such as purely pressure supported soliton-like solutions [145], and superposition or interference during interactions between condensate-like halos [146]. Consequently, modelling dark matter dynamics in ULDM scenarios is more challenging than in simple cold dark matter models, but it is critical to understanding complex ULDM physics.

In the non-relativistic regime, the dynamics of ULDM can be reduced to the Schrödinger-Poisson system, where the complex variable ψ describes the local density of ULDM quanta, while the Poisson equation describes the local gravitational potential. Many approaches have been taken to this problem, including both modifications of existing cosmological simulation codes and the development of new codes specifically designed for ULDM systems. One widely used approach is the Madelung fluid formulation of the Schrödinger-Poisson system [147] which has a quantum pressure term that can be treated numerically in a variety of ways. In Ref. [148], the cosmological code GADGET [149] is modified to treat the quantum pressure as an effective particle-particle interaction and the resulting code, AXION-GADGET is publicly available [150]. Ref. [151] modifies a non-public extension of GADGET, P-GADGET3 to treat the quantum pressure term via smoothed-particle hydrodynamics (SPH) routines. The SPH approach is also used in Ref. [152], while a particle-mesh approach was implemented in [153]. NYX [154] was modified in [146] to study merging ULDM solitonic cores, GALACTICUS [155] was modified in [156] to study the effects of tidal stripping and dynamical friction on ULDM halos, AREPO [157] was modified in [158] to study the core-mass relationship and turbulence characteristics of ULDM halos, and GAMER [159, 160] was modified

[129] to perform a detailed study of structure formation in ULDM cosmologies.

In this chapter I introduce PyUltraLight,[2] a stand-alone Python-based pseudospectral Schrödinger-Poisson solver. The key advantage of this code is that it reproduces many of the key findings of more complicated cosmological simulation codes within a desktop computing environment. Hence, it may provide a valuable cross-check on more complex implementations, as well as serve as a basis for further development of such codes within the computational cosmology community.

PyUltraLight is based on a symmetrised-split-step (leapfrog) solver for time evolution, and uses a pseudospectral Fourier algorithm to solve the Poisson equation for the gravitational potential at each step.[3] This algorithm has second order accurate time integration steps and sub-percent level energy conservation, while the wavefunction normalisation is conserved to machine precision. As a pseudospectral code, linear differential operators are computed by direct multiplication in the Fourier domain, while nonlinear terms are evaluated in position space. Consequently, PyUltraLight is free from noise associated with spatial derivatives computed via finite-differencing. There is a necessary computational cost associated with the Fourier and inverse Fourier transforms but these transforms are optimised in PyUltraLight through the use of the pyFFTW pythonic wrapper around the C-based FFTW subroutine library [167, 168]. As the FFTW libraries offer full parallelisation, PyUltraLight is currently designed to take advantage of multiple cores on a user PC or shared-memory environment. Full MPI compatibility has not yet been implemented as we have not found a need to run simulations in a distributed-memory cluster environment, however future releases may address this possibility. We note that some modifications to PyUltraLight developed by other research groups have successfully implemented MPI compatibility [169]. This will be discussed later in more detail.

[2]The initial code development for PyUltraLight was completed as part of an MSc thesis by Faber Edwards, with contributions by Shaun Hotchkiss and Richard Easther [161]. Further code development was then undertaken by myself, as well as the entirety of the analysis, verification and written work presented here.

[3]A similar methodology was described in Ref. [162]; at the time of writing this code has not been released. Spectral methods are often used to solve the Poisson equation in large scale structure simulations, while the PSpectre code [163] provides a pseudospectral solver for the evolution of the inflaton and fields coupled to it during parametric resonance and preheating after inflation [164, 165, 166].

In the following sections, I first describe the implementation of the Schrödinger-Poisson system in PyUltraLight, referring the reader to Section 3.3 for a review of the derivation of the Schrödinger-Poisson equations in this context. I then describe testing and verification procedures applied to the code. I reproduce a selection of results from a variety of other ULDM simulations and discuss the energy conservation and accuracy as a function of spatial resolution.

3.2 The rescaled Schrödinger-Poisson Equations

The Schrödinger-Poisson system which describes the non-relativistic dynamics of ULDM is as given by:

$$i\hbar\dot{\psi} = -\frac{\hbar^2}{2m}\nabla^2\psi + m\Phi\psi, \tag{3.1}$$

where ψ is interpreted as the macroscopic wavefunction of a Bose-Einstein condensate. It follows that the particle number density of the condensate is given by $|\psi|^2$, so its mass density is simply $m|\psi|^2$. The local gravitational potential thus satisfies the Poisson equation,

$$\nabla^2\Phi = 4\pi G m|\psi|^2, \tag{3.2}$$

where G is Newton's gravitational constant. The coupled equations 3.1 and 3.2 together form the nonlinear Schrödinger-Poisson system. While Equations 3.1 and 3.2 are valid for open boundary conditions, PyUltraLight is designed to solve the Schrödinger-Poisson system under periodic boundary conditions. In this case the correct form of equation 3.2 is

$$\nabla^2\Phi = 4\pi G m\big(|\psi|^2 - \langle|\psi|^2\rangle\big), \tag{3.3}$$

where we subtract the average density from the right hand side of the Poisson equation. The form of Equation 3.3 is a consequence of Gauss' law and the fact that the surface integral of the gradient of the field around the perimeter of the simulation grid is identically zero when periodic boundary conditions are imposed [170].

It is helpful to recast the Schrödinger-Poisson system (equations 3.1 and 3.3) in terms of adimensional quantities. In keeping with Refs [132, 162] we introduce

length, time, and mass scales as follows:

$$L = \left(\frac{8\pi\hbar^2}{3m^2H_0^2\Omega_{m_0}}\right)^{\frac{1}{4}} \approx 121\left(\frac{10^{-23}\,\mathrm{eV}}{m}\right)^{\frac{1}{2}}\,\mathrm{kpc}, \tag{3.4}$$

$$T = \left(\frac{8\pi}{3H_0^2\Omega_{m_0}}\right)^{\frac{1}{2}} \approx 75.5\,\mathrm{Gyr}, \tag{3.5}$$

$$M = \frac{1}{G}\left(\frac{8\pi}{3H_0^2\Omega_{m_0}}\right)^{-\frac{1}{4}}\left(\frac{\hbar}{m}\right)^{\frac{3}{2}} \approx 7\times10^7\left(\frac{10^{-23}\,\mathrm{eV}}{m}\right)^{\frac{3}{2}}\mathrm{M}_\odot, \tag{3.6}$$

where m is the mass of the ultra-light scalar field, H_0 is the present-day Hubble parameter, G is Newton's gravitational constant and Ω_{m_0} is the present-day matter fraction of the energy density of the universe. We recast equations 3.1 and 3.2 in terms of the dimensionless quantities

$$t' = \frac{t}{T}, \quad \vec{x}^{\,\prime} = \frac{\vec{x}}{L}, \quad \Phi' = \frac{mT}{\hbar}\Phi, \quad \psi' = T\sqrt{mG}\psi. \tag{3.7}$$

Dropping the primes for notational convenience, we see that the coupled differential equations of the Schrödinger-Poisson system under periodic boundary conditions reduce to

$$i\dot{\psi}(\vec{x},t) = -\frac{1}{2}\nabla^2\psi(\vec{x},t) + \Phi(\vec{x},t)\psi(\vec{x},t), \tag{3.8}$$

$$\nabla^2\Phi(\vec{x},t) = 4\pi\big(|\psi(\vec{x},t)|^2 - \langle|\psi(\vec{x},t)|^2\rangle\big), \tag{3.9}$$

where it is understood that all quantities involved are dimensionless. We can recover dimensionful quantities via the "dictionary" provided by equations 4.7 to 4.8. For example, the integrated mass of the system, M_{tot}, is given by

$$M_{tot} = M\int d^3x|\psi|^2. \tag{3.10}$$

Likewise, the mass density at any point is given by

$$\rho = ML^{-3}|\psi|^2. \tag{3.11}$$

By dimensional analysis, we can easily restore dimensionful units to any of the

quantities calculated by the code. In particular, in the following sections it is to be understood that

$$E = ML^2T^{-2}\ E_{code}, \quad v = LT^{-1}\ v_{code}, \tag{3.12}$$

where E and v represent energy and velocity, respectively. PyUltraLight works internally with these dimensionless quantities, but can receive initial conditions and generates output in physical units. Henceforth, we will often refer to $|\psi|^2$ as the density, where it is understood that this is in fact a dimensionless quantity related to the physical mass density via the constant of proportionality given by equation 3.11.

3.3 Dynamical Evolution in PyUltraLight

Dynamical evolution within PyUltraLight progresses via a symmetrised split-step Fourier process on an $N \times N \times N$ grid with periodic spatial boundary conditions.[4] To understand this method, first consider the exact expression for the unitary time evolution of the wavefunction according to equation 3.8, namely

$$\psi(\vec{x}, t+h) = \mathcal{T} \exp\left[-i \int_t^{t+h} dt' \left\{-\frac{1}{2}\nabla^2 + \Phi(\vec{x}, t')\right\}\right] \psi(\vec{x}, t), \tag{3.13}$$

where $\mathcal{T}$ is the time-ordering symbol. For a sufficiently small timestep h, the trapezoidal rule gives the approximation

$$\int_t^{t+h} dt' \Phi(\vec{x}, t') \approx \frac{h}{2}\Big(\Phi(\vec{x}, t+h) + \Phi(\vec{x}, t)\Big). \tag{3.14}$$

We can therefore write the approximate form of equation 3.13 as

$$\psi(\vec{x}, t+h) \approx \exp\left[i\frac{h}{2}\Big(\nabla^2 - \Phi(\vec{x}, t+h) - \Phi(\vec{x}, t)\Big)\right] \psi(\vec{x}, t). \tag{3.15}$$

[4] PyUltraLight is publicly available under a BSD licence. The full repository, including supplementary files such as the code used to generate soliton profiles, is available on GitHub at `https://github.com/auckland-cosmo/PyUltraLight`. PyUltraLight makes use of the pyFFTW pythonic wrapper around the FFTW C-based fast Fourier transform libraries. Both pyFFTW and FFTW are freely-available and PyUltraLight has been used successfully on both Mac OS and Linux systems, as well as a shared-memory cluster environment. We welcome advice and feedback from users.

Note that the exponential in equation 3.15 omits the time-ordering symbol, and is only equivalent to its time-ordered counterpart to order h^2.

The linear differential operator in equation 3.15 acts naturally in Fourier space, while the nonlinear potential term is simplest to evaluate in position space. By splitting the exponential we can evaluate each term in its natural domain. Such a splitting is valid when the timestep is small, and is represented as

$$\psi(\vec{x}, t+h) \approx \exp\left[-\frac{ih}{2}\Phi(\vec{x}, t+h)\right] \exp\left[\frac{ih}{2}\nabla^2\right] \exp\left[-\frac{ih}{2}\Phi(\vec{x}, t)\right] \psi(\vec{x}, t). \quad (3.16)$$

This splitting can be understood thusly: first, a half timestep is taken in which only the nonlinear potential operator acts, followed by a full timestep in the linear term. The potential field is then updated, and a final half timestep in the nonlinear term is performed. Using the Baker-Campbell-Hausdorff formula to express the product of exponentials in equation 3.16 as a single exponential and keeping only terms to order h^2 we find:

$$\exp\left[i\frac{h}{2}\Big(\nabla^2 - \Phi(\vec{x}, t+h) - \Phi(\vec{x}, t)\Big) + \frac{h^2}{8}\Big[\nabla^2, \Phi(\vec{x}, t)\Big] - \frac{h^2}{8}\Big[\nabla^2, \Phi(\vec{x}, t+h)\Big]\right]. \quad (3.17)$$

Making use of the fact that $\Phi(\vec{x}, t+h) \approx \Phi(\vec{x}, t) + h\dot{\Phi}(\vec{x}, t)$ we see that the commutators in equation 3.17 cancel at $\mathcal{O}(h^2)$ and the expression matches 3.15, with the dominant error term appearing at $\mathcal{O}(h^3)$.

Evaluation of equation 3.16 within PyUltraLight thus proceeds as follows: Initially, the nonlinear term acts in position space for one half-timestep. The result is Fourier transformed, and a full timestep is taken with the differential operator applied in the Fourier domain. The potential field is then updated in accordance with equation 3.9. After an inverse Fourier transform a final half timestep is taken with the updated nonlinear term acting in position space to give the new ψ field configuration. This procedure is known as the symmetrised split-step Fourier method, and used widely in fields such as nonlinear fiber optics [171, 172, 173].

The algorithm can be represented schematically as

$$\psi(\vec{x}, t+h) = \exp\left[-\frac{ih}{2}\Phi(\vec{x}, t+h)\right] F^{-1} \exp\left[\frac{-ih}{2}k^2\right] F \exp\left[-\frac{ih}{2}\Phi(\vec{x}, t)\right] \psi(\vec{x}, t), \quad (3.18)$$

where the order of operations runs from right to left, F and F^{-1} denote the discrete Fourier transform and its inverse, and k is the wavenumber in the Fourier domain. The potential field is updated following the inverse Fourier transform in equation 3.18, via

$$\Phi(\vec{x}, t+h) = F^{-1}\left(-\frac{1}{k^2}\right) F\ 4\pi|\psi(\vec{x}, t_i)|^2, \tag{3.19}$$

where $\psi(\vec{x}, t_i)$ is the field configuration at this halfway point in the full timestep. We explicitly set the $k = 0$ Fourier mode to zero prior to the final inverse Fourier transform; as a consequence there is no need to subtract the global average density from the local value in Equation 3.19, in contrast to Equation 3.3. The final operation in equation 3.18 only changes the phase of ψ, so we could replace $\psi(\vec{x}, t_i)$ with $\psi(\vec{x}, t+h)$ in equation 3.19 with no change in meaning. PyUltraLight makes an additional simplification to the symmetrised split-step Fourier method by combining the consecutive half-steps in the nonlinear term into a single full step. Consequently, only the first and last operations involve actual half steps. Schematically this becomes:

$$\psi(t+nh) = \exp\left[+\frac{ih}{2}\Phi\right]\left(\prod^{n}\exp\left[-ih\Phi\right]\exp\left[\frac{ih}{2}\nabla^2\right]\right)\exp\left[-\frac{ih}{2}\Phi\right]\psi(t), \tag{3.20}$$

where Φ is updated at each step via equation 3.19. Attention is drawn to the sign difference between the first and last operators. The positive sign in the last operator is a consequence of the grouping of the preceding consecutive half steps.

From a computational perspective, the numerical Fourier transforms are likely to be the rate-limiting step in any pseudospectral code. In PyUltraLight the discrete Fourier transform (DFT) and its inverse are implemented via pyFFTW, a pythonic wrapper for the C-based FFTW subroutine library which efficiently implements both real and complex DFTs [167, 168, 174]. This allows PyUltraLight to combine the flexibility of a notebook based modelling tool with the efficiency of a carefully tuned, compiled numerical library. FFTW is fully parallelised and its support for multithreading is inherited by pyFFTW and accessed within PyUltraLight; the number of threads used by the pyfftw.FFTW class is determined by the Python multiprocessing routines which are used to ascertain the number of available CPU cores. In addition, PyUltraLight uses the NumExpr package to

parallelise operations on array objects within the simulation [175].

3.4 Initial Conditions: Soliton Profiles

PyUltraLight specifies the initial dark matter configuration as a superposition of an arbitrary number of solitonic halos, with arbitrary (user-defined) velocities and phases. This is necessarily an idealisation, given that realistic dark matter halos will not map directly to the solitonic solutions, but it provides an excellent "playground" in which to explore ULDM dynamics, and the initialisation routines within PyUltraLight can be easily augmented to accommodate a wider range of scenarios. The initial field configuration is built by loading a NumPy array file encoding a solitonic solution to the Schrödinger-Poisson system and the corresponding position mass, velocity, and phase parameters each specified by the user within the accompanying Jupyter notebook.

In practice, only a finite range of halo masses can be supported within a given simulation – the radius of a solitonic halo is inversely proportional to its mass, so resolving a light halo interacting with a very massive halo would require an extremely fine spatial mesh. However, PyUltraLight also allows the user to specify a fixed, external potential which does not take part in the dynamics. At this point only a central $1/r$ potential is supported but this would be easily generalised. It should be noted that because PyUltraLight enforces periodic boundary conditions, care must be taken in cases where solitons approach the boundaries of the simulation grid. If a soliton were to cross the boundary during a simulation in which a Newtonian central potential is implemented, the forces exerted during the crossing would be unphysical. For studies of orbital stability this is unlikely to cause any problems, as in these circumstances material collapses toward the centre of the simulation grid rather than crossing the boundaries. However, the user should ensure that solitons are initialised sufficiently far from the boundary for the purposes of each simulation on a case-by-case basis. In situations where a significant portion of the total mass is expected to be ejected, such as the merger of multiple solitons to form a larger halo, care should be taken to ensure that mass ejected above the escape velocity is not recaptured as it re-enters the grid from the other side. For studies of this kind, an absorbing sponge at the grid boundaries is

perhaps more suitable than periodic boundary conditions, though this has not yet been implemented in PyUltraLight.

The soliton profile used to generate the initial conditions in PyUltraLight is found by first imposing spherical symmetry in the Schrödinger-Poisson equations and assuming time independence in the radial density profile [162]:

$$\psi(\vec{x},t) \to e^{i\beta t} f(r), \quad \Phi(\vec{x},t) \to \varphi(r), \tag{3.21}$$

where $r = |\vec{x}|$. Introducing $\tilde{\varphi}(r) := \varphi(r) + \beta$, equations 3.8 and 3.9 reduce to

$$0 = -\frac{1}{2} f''(r) - \frac{1}{r} f'(r) + \tilde{\varphi}(r) f(r) \tag{3.22}$$

$$0 = \tilde{\varphi}''(r) + \frac{2}{r}\tilde{\varphi}'(r) - 4\pi f(r)^2 \tag{3.23}$$

where primes denote derivatives with respect to r. Note that this system contains no arbitrary constants, so the underlying profile is effectively universal and is loaded as a pre-computed array by PyUltraLight, rather than computed from scratch with each code execution. The soliton profile numpy array file is included with PyUltraLight, however, an auxiliary program soliton_solution.py is also supplied, from which this array can be generated; it uses a fourth-order Runge-Kutta algorithm to solve the coupled profile equations. We set $f(r)|_{r=0}$=1, while smoothness requires that first derivatives of $f(r)$ and $\tilde{\varphi}(r)$ vanish at the origin. We then use the shooting method to search for solutions of $f(r)$ and $\varphi(r)$ satisfying the boundary conditions $\lim_{r\to\infty} \varphi(r) = 0$ and $\lim_{r\to\infty} f(r) = 0$, varying $\tilde{\varphi}(r)|_{r=0}$ until we obtain a solution of $f(r)$ which approaches zero at the maximal specified radius, r_m. The value of β is then calculated by assuming that $\varphi(r)$ goes as $-c/r$ at large radii, where c is a constant. Under this assumption, we can write

$$\tilde{\varphi}(r_m) = -\frac{c}{r_m} + \beta, \quad c = r_m^2 \tilde{\varphi}\,'(r_m). \tag{3.24}$$

We thus obtain the full solution $\psi(\vec{x},t) = e^{i\beta t} f(r)$. Having initially chosen $f(r)|_{r=0} = 1$, we may then generalise to $f(r)|_{r=0} = \alpha$, where α is an arbitrary positive real number. It is easily verified that if $e^{i\beta t} f(r)$ is a solution to the spherically

symmetric Schrödinger-Poisson system, then $g(r)$ is also a solution, where

$$g(r) = e^{i\alpha\beta t}\alpha f(\sqrt{\alpha}\ r). \tag{3.25}$$

A more detailed discussion of the scaling properties of the Schrödinger-Poisson system is given in Appendix A. We thus have a family of spherically symmetric soliton solutions to the dimensionless Schrödinger-Poisson system; the dimensionless soliton mass is proportional to $\sqrt{\alpha}$ and the full width at half maximum is proportional to $1/\sqrt{\alpha}$. Since the size of the soliton scales inversely with the mass, the most massive soliton in the solution puts a lower bound on the required spatial resolution.

The Schrödinger equation is not trivially form invariant under Galilean boosts but we can enforce Galilean covariance through the addition of a velocity-dependent phase factor,

$$\psi(\vec{x}, t) = \alpha f\big(\sqrt{\alpha}|\vec{x} - \vec{v}t|\big)e^{i\left(\alpha\beta t + \vec{v}\cdot\vec{x} - \frac{1}{2}|\vec{v}|^2 t\right)}. \tag{3.26}$$

To construct the initial field configuration, PyUltraLight, loads the NumPy array encoding the radial profile $f(r)$ for the $f(r)|_{r=0} = 1$ case. Equation 3.26 is then used to transform the this solution into soliton(s) with user-specified values position, mass, and velocity specified, via the accompanying Jupyter notebook. The user may also add an additional constant phase factor if desired.

3.4.1 Choosing the Timestep

The Courant-Friedrichs-Lewy (CFL) condition is an upper bound on the timestep (as a function of grid-spacing) that must be satisfied by many partial differential equation solvers based on finite-differencing [176] and is often cited in numerical analyses of ULDM via the Schrödinger-Poisson system, see e.g. Ref. [146]. However, the CFL condition expresses a causality constraint, and is generally only strictly applicable to hyperbolic PDEs, whereas the Schrödinger-Poisson has only a first order time derivative, even though it is effectively the nonrelativistic limit of the Klein-Gordon equation. Moreover, because PyUltraLight computes spatial derivatives via a pseudospectral method, technically it is unconditionally stable [177]. Our split-step algorithm is second order in the timestep, and its value will

always be an empirical tradeoff between computational cost and convergence to the apparent limit in which step is arbitrarily small. Consequently, the user is encouraged to validate their choice of timestep via case-by-case convergence testing.

The default timestep in PyUltraLight is fixed with reference to the fluid interpretation of the Schrödinger-Poisson system [117]. The fluid interpretation is often used to recast the Schrödinger-Poisson system in the form of the Madelung equations [178] - a hydrodynamical representation of the system. The first step is to define:

$$\psi \equiv \sqrt{\rho} e^{i\theta}, \quad \vec{v} \equiv \boldsymbol{\nabla}\theta. \tag{3.27}$$

and to treat $\vec{v}$ as a fluid velocity. From this perspective, if the phase difference between two adjacent grid points exceeds π, the fluid will appear to move "backwards" across the grid. We thus set the default timestep, Δt, so that fluid travelling at this maximum velocity traverses one grid space, Δx, per timestep, or

$$\Delta t = \frac{(\Delta x)^2}{\pi}. \tag{3.28}$$

This is a choice, rather than a strict constraint on Δt. However, if the "fluid" approaches velocities where the phase appears to switch direction, the configuration is approaching the point where the simulation grid is too coarse to fully resolve the dynamics. Hence, a timestep much smaller than this value may offer little practical advantage. However, in some cases the breakdown may occur in regions of the simulation volume that are of little physical interest, and the user is free to choose a larger timestep via the 'step_factor' parameter in the Jupyter notebook.

Alternatively, Ref. [158] fixes the timestep by ensuring that neither of the unitary operators in Equation 3.18 lead to a phase change of more than π for a single grid point over one timestep. However, because the pseudo-spectral algorithm does not compare the phase of a single gridpoint at different points in time, this choice of timestep is not a requirement for stability. This method gives the following constraints:

$$\Delta t < \left[\frac{2\pi}{\Phi_{max}}, \frac{2(\Delta x)^2}{\pi} \right], \tag{3.29}$$

where the second of these constraints is generally the stricter of the two, and is equivalent to our default choice of timestep up to a multiplicative factor of $\mathcal{O}(1)$.

Our experience is that specifying the timestep via Equation 3.28 is suitable for the majority of simulation scenarios, and we explore convergence in more detail in Section 3.7.

3.5 ULDM Dynamics with PyUltraLight

In this section, we validate PyUltraLight by reproducing results from previous studies of ULDM dynamics, demonstrating interference effects and effective repulsive forces arising from the wavelike nature of ULDM. In addition we study the evolution of the velocity field of a solitonic core orbiting within a Newtonian central potential, showing that the stable orbital configuration is an irrotational Riemann-S ellipsoid. Finally, we demonstrate that PyUltraLight delivers sub-percent level energy conservation for a selection of dynamical scenarios.

3.5.1 Interference Patterns During Soliton Collisions

The outcomes of ULDM soliton collisions depend critically on whether the total energy of the isolated binary system is positive or negative. With a positive total energy the solitons pass through each other, emerging largely undisturbed from their initial configurations and the wavefunctions describing the solitons are superposed during the collision, yielding distinctive interference patterns.

Following [146], we consider the head-on collision of two solitons with mass ratio $\mu = 2$ and high relative velocity. While we work in dimensionless code units, it should be noted that a dimensionful velocity can be restored from the code velocity by multiplying through by LT^{-1}, the scale parameters defined in Equations 4.7 and 3.5. This simple case of a head-on soliton collision can be treated approximately. Starting from equation 3.26 we write the total wavefunction of the binary system in terms of dimensionless quantities along the collision axis as

$$\begin{aligned}\psi(x,t) = \alpha_1 f\big(\sqrt{\alpha_1}|x - x_1 - v_1 t|\big) e^{i\left(\alpha_1\beta t + v_1(x-x_1) - \frac{1}{2}v_1^2 t + \delta\right)} \\ + \alpha_2 f\big(\sqrt{\alpha_2}|x - x_2 - v_2 t|\big) e^{i\left(\alpha_2\beta t + v_2(x-x_2) - \frac{1}{2}v_2^2 t\right)},\end{aligned} \tag{3.30}$$

where x_1 and x_2 are the initial central positions of the solitons, v_1 and v_2 are the

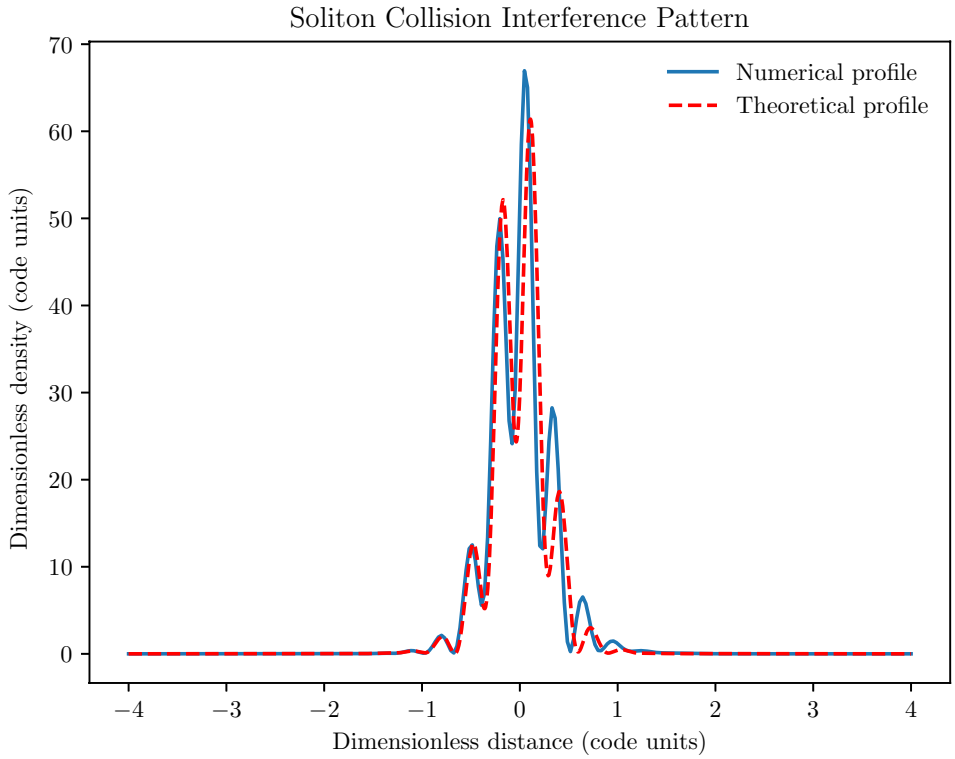

Figure 3.1: Comparison of theoretical and numerical density profiles at time of maximal interference for head-on collision of two solitons with mass ratio $\mu = 2$ and no relative phase difference. The solitons have dimensionless masses 5 and 10, with an initial separation of 4 code units and relative velocity of 20 code units. The simulation resolution is 256^3 in a box of side-length 8.

soliton velocities, δ is a constant relative phase term and $\alpha_2 = 4\,\alpha_1$, parameterising the density profiles as discussed in Section 3.4. For convenience we set $v_1 = -v_2$ and $x_1 = -x_2$. We expect that the interference effects will be maximised when two components of the wavefunction are centred at the same location, such that $x_1 + v_1 t = -x_2 - v_2 t = 0$. This corresponds to a time $t_o = |x_1/v_1| = |x_2/v_2|$, where in this simplified model we do not account for distortions caused by the accelerating or compactifying effects that the gravitational interaction has on the soliton profiles as they approach one another. The dimensionless density is then given by

$$|\psi(x, t_o)|^2 = \alpha_1^2 \Big[f(\sqrt{\alpha_1} x)^2 + 16 f(2\sqrt{\alpha_1} x)^2 +$$

$$8f(\sqrt{\alpha_1}x)f(2\sqrt{\alpha_1}x)\cos\left(-3\alpha_1\beta\left|\frac{x_1}{v_1}\right|+2v_1x+\delta\right)\Bigg]. \quad (3.31)$$

Figure 3.1 shows the dimensionless density profile at the time of maximal interference for two solitons with mass ratio 2 and phase difference $\delta = 0$. The numerical result obtained using PyUltraLight closely matches the theoretical prediction of equation 3.31. Small disparities between the numerical and theoretical profiles may be attributed to the effect of gravitational contraction not included in the theoretical prediction of equation 3.31 and to a small offset in the true time of maximal interference due to the solitons accelerating as they fall together. We do not expect an exact match, but we have verified that PyUltraLight qualitatively reproduces the wave interference effects of the ULDM model. With the exception of [146], few studies of ULDM dynamics have investigated the interference patterns generated by colliding solitons in this way. In some cases, this is because the algorithm employed to simulate the dynamics is not capable of reproducing such effects. An example of this is given in [153], where it is demonstrated that the coarse-grained nature of the particle-mesh method renders the algorithm incapable of reproducing detailed interference patterns such as those shown here.

3.5.2 Effective Forces From Destructive Interference

As demonstrated in [162], the wavelike properties of ULDM give rise to effective forces which can dramatically affect the dynamics of core collisions. These effective forces arise as a result of interference phenomena, rather than because of any local interactions the ULDM model might incorporate. Figure 3.2 shows the results of a head-on collision between two solitons, where in one instance the solitons have no initial phase difference, and in the other instance a phase difference of π is applied in the initial conditions. In this simulation, solitons of mass 20 are initialised with relative velocity 20 and initial separation 1.2 (code units). The solitons are allowed to collide, and contours of the density profile along the plane of symmetry are displayed. In one case (top) there is no phase offset between the initial solitons, while in the second the phases differ by π. In the latter case, the phase shift creates an effective repulsive force between the two solitons. It can be seen in the second frame that as the solitons approach one another, the π phase shift results in a

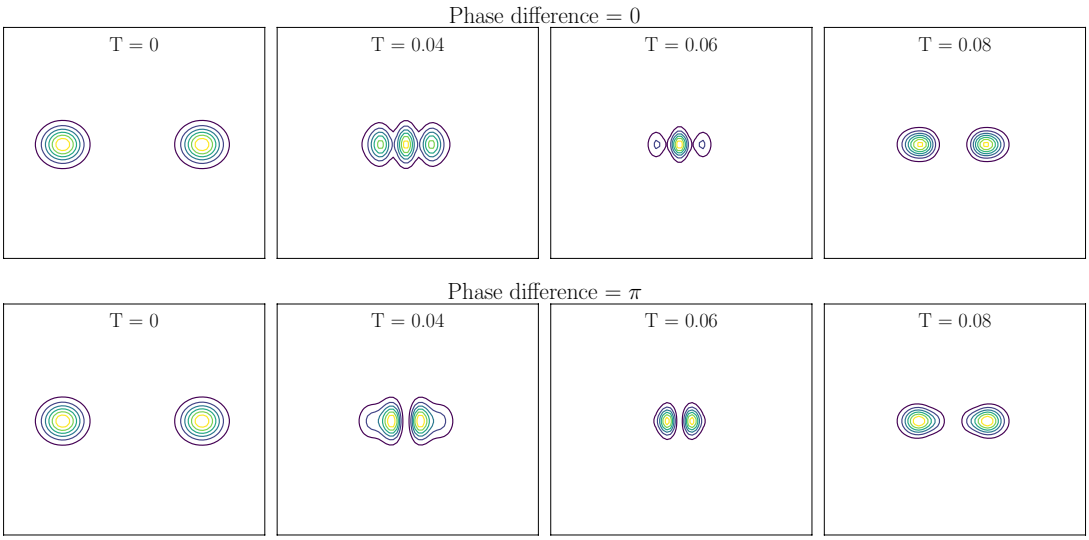

Figure 3.2: Head-on collisions between solitons of mass 20, initial relative velocity 20, and initial separation 1.2 in code units. Plots show contours of constant density; time progresses from left to right across each row and is indicated in code units for each frame. The upper panel shows solutons initially in phase; the effective repulsive force generated by a π phase shift can be seen in the lower panel.

slowing of the approach accompanied by a deformation of the density profile, acting so as to avoid contact between the solitons. Dissimilarly, in the case where there is no phase shift, the solitons readily collide and merge to form a single contiguous density profile prior to re-separating. Further discussion of this phenomenon and its possible observational consequences can be found in [162].

3.5.3 Tidal Disruption of Solitons Orbiting a Central Potential

PyUltraLight allows the inclusion of a static potential equivalent to a point-mass at the centre of the simulation region. There is no backreaction on this mass as a result of the ULDM dynamics, and its "mirror images" within the periodic coordinate systems are not accounted for within the overall gravitational potential. While a potential of this form does not necessarily accurately emulate that which we might expect from a realistic galaxy or dark matter halo, it provides a starting

point for a study of the stability of satellite dark matter halos orbiting a much larger object. In particular, this includes the investigation of lifespans of dwarf satellite galaxies orbiting much larger objects (including the Milky Way) which are a key to understanding whether ULDM models can resolve the so-called missing satellites problem [90].

An extensive study of the tidal disruption of ULDM solitonic cores orbiting a central potential has recently been undertaken in [179] and we reproduce just one of their results here. To do this, we again adopt Equation 3.27, namely:

$$\psi \equiv \sqrt{\rho} e^{i\theta}, \quad \vec{v} \equiv \boldsymbol{\nabla}\theta, \tag{3.32}$$

where we are working in dimensionless code units. Using these definitions, the Schrödinger-Poisson system can be recast in terms of hydrodynamical quantities in the so-called Madelung representation. The Madelung equations resemble the continuity and Euler equations of classical fluid dynamics, with the addition of a 'quantum pressure' term accounting for resistance against gravitational collapse. The Madelung formalism is discussed in detail in [178, 180, 181, 182]. Because this hydrodynamical formulation defines the fluid velocity as the gradient of the phase of the field ψ, problems arise when $\psi = 0$, where the phase is not well defined. Because of this issue, the Madelung and Schrödinger representations are not strictly equivalent unless a quantisation condition is imposed, as discussed in [183]. We do not consider the subtleties of the Madelung representation here, as it is sufficient for our purposes to consider the fluid velocity in the region of a solitonic core, where no field nodes are present.[5] For a discussion of the possible remedies to the 'nodes problem', the reader is referred to Chapter 15.3 of [184]. Where the Madelung representation is well defined, i.e. where the phase is a smoothly varying function, the velocity field of the Schrödinger-Poisson system is strictly irrotational, $\nabla \times \vec{v} = 0$. If a radially symmetric soliton is initialised in a circular orbit around a Newtonian potential, there will be initial transient behaviour as the spherical profile becomes elongated along the radial direction of the central potential. Meanwhile, the velocity field corresponding to the overall orbital motion of the soliton will be

[5]It should be noted that, restoring dimensionful units, the fluid velocity $\vec{v}$ is related to the ususal quantum mechanical probability current $\vec{j}$ through $|\psi|^2\vec{v} = \vec{j} = \hbar/2mi\,[\psi^*\nabla\psi - \psi\nabla\psi^*]$

superposed with the internal velocity field, combining so as to produce a net flow with vanishing curl.

The family of Riemann-S ellipsoids describe non-axisymmetric uniformly rotating bodies whose internal velocity fields have vanishing curl [185]. Therefore, it is the characteristic internal velocity field of a Riemann-S ellipsoid which we expect to arise during our simulation of a soliton orbiting a central mass. It is found in [179] that an initially spherical solitonic core without self-rotation will gradually spin up to form a tidally-locked ellipsoid with an irrotational internal velocity field when orbiting a host mass. We reproduce this result using PyUltraLight. Figure 3.3 shows the internal velocity field of a solitonic satellite after one complete revolution around a host mass. The soliton has become elongated along the radial line connecting it to the host, indicating that it is tidally locked, while the velocity field within the tidal radius is visibly irrotational and bears the qualitative trademarks of the Riemann-S ellipsoid as presented in Figure 2 of [186].

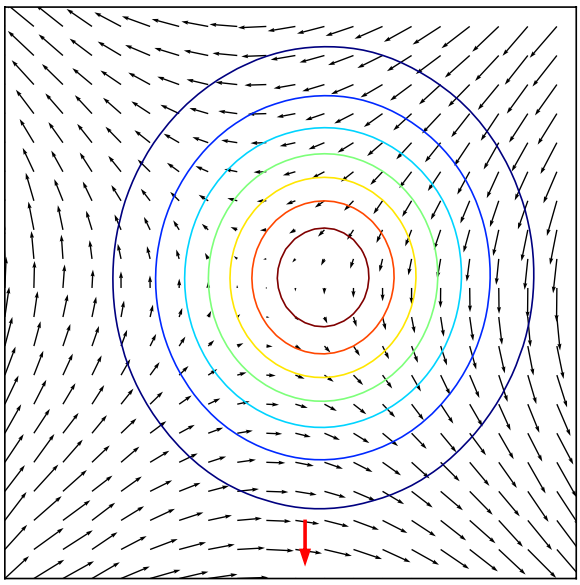

Figure 3.3: Contours of constant density for a solitonic core after one revolution around a central potential. Contours are superimposed upon the internal velocity field (with the bulk motion subtracted). This velocity field is qualitatively that of an irrotational Riemann-S ellipsoid, and the deformation of the density profile of the soliton along the radial direction (red arrow) is visible. The host:satellite mass ratio is approximately 55; simulation resolution is 256^3.

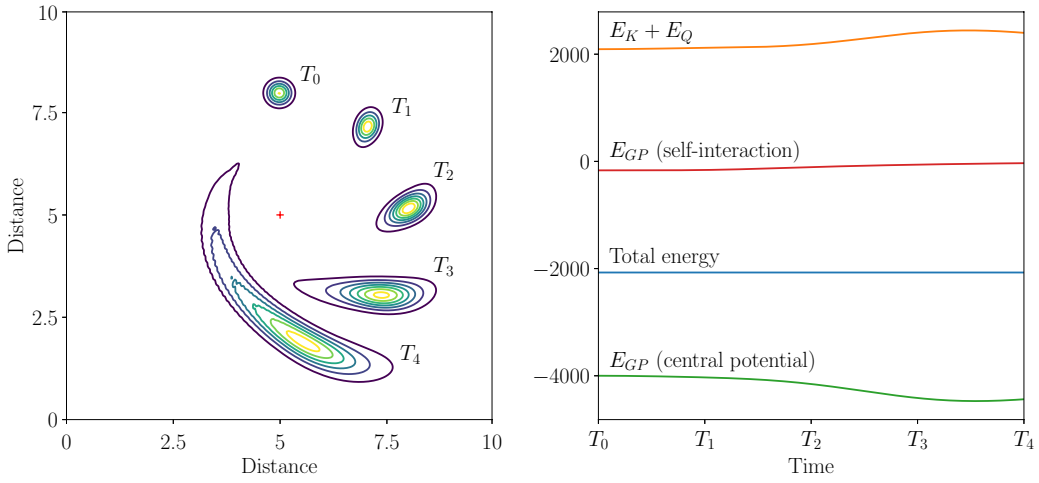

Figure 3.4: Left: Evolution of the density profile of a solitonic core at equally spaced times as it undergoes tidal disruption in a potential centred at the red cross. Right: Evolution of the components of the total energy of the system; times correspond to the labeled density profile snapshots. All quantities are in dimensionless code units.

It should be noted that the wider velocity field is not expected to be accurately predicted in a simulation of this kind, though the field within the tidal radius is well-modelled. This is because the initial soliton density profile is defined only out to a given cutoff radius, beyond which the ψ field value is set identically to zero. As mentioned previously, the Madelung hydrodynamical formulation of the Schrödinger-Poisson system is not valid where $\psi = 0$. Because of this, we focus primarily on the internal velocity field within the high density region of the solitonic core. As we have seen, in this region PyUltraLight is able to accurately reproduce the expected velocity field characteristics.

3.6 Energy Conservation

Physically, we require that the overall energy in the system will be conserved. This provides a test on the numerical performance of PyUltraLight, and we find that even at relatively low spatial resolution we see sub-percent level energy conservation for all the dynamical scenarios considered here. In this section, we express the energy of the Schrödinger-Poisson system in terms of the variables ψ and Φ and

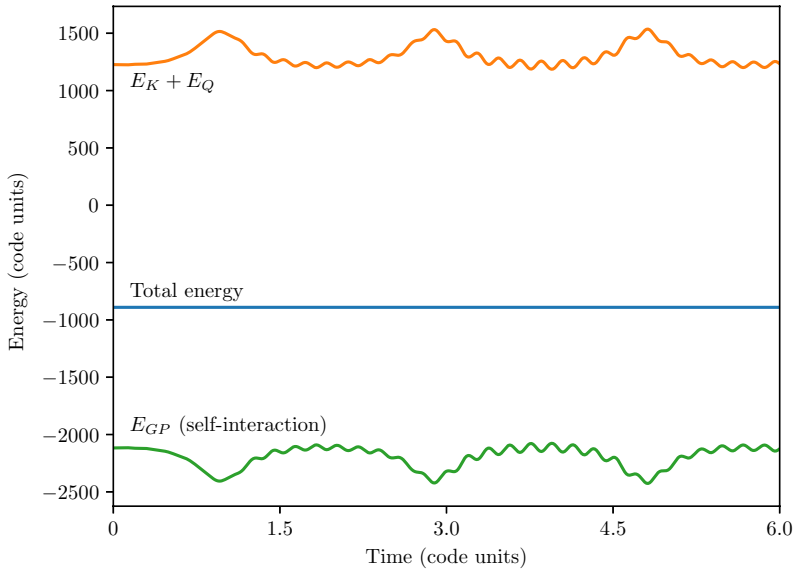

Figure 3.5: Evolution of the components of the total energy of a binary soliton system with each soliton in an elliptical orbit around the common centre of mass.

discuss its decomposition into individual constituents calculated separately within the code. We then present results for a variety of configurations.

We begin by defining a suitable action which yields the full Schrödinger-Poisson system through its corresponding Euler-Lagrange equations. We find that variation of

$$S = \int dt \int_{\mathbb{R}^3} d^3x \; - \left\{ \frac{1}{2}|\nabla\Phi|^2 + \Phi|\psi|^2 + \frac{1}{2}|\nabla\psi|^2 + \frac{i}{2}(\psi\dot{\psi}^* - \dot{\psi}\psi^*) \right\} \tag{3.33}$$

with respect to Φ, ψ^* and ψ yields equations 3.9, 3.8, and the conjugate of equation 3.8, respectively. The integrand of equation 3.33 is the Lagrangian density, $\mathcal{L}$, from which we can derive the conserved energy in the usual way:

$$E_{tot} = \int_{\mathbb{R}^3} d^3x \left\{ \frac{\partial\mathcal{L}}{\partial\dot{\psi}}\dot{\psi} + \frac{\partial\mathcal{L}}{\partial\dot{\psi}^*}\dot{\psi}^* + \frac{\partial\mathcal{L}}{\partial\dot{\Phi}}\dot{\Phi} - \mathcal{L} \right\}. \tag{3.34}$$

Evaluating this expression, we obtain:

$$E_{tot} = \int_{\mathbb{R}^3} d^3x \left\{ \frac{1}{2}|\nabla\Phi|^2 + \Phi|\psi|^2 + \frac{1}{2}|\nabla\psi|^2 \right\} \tag{3.35}$$

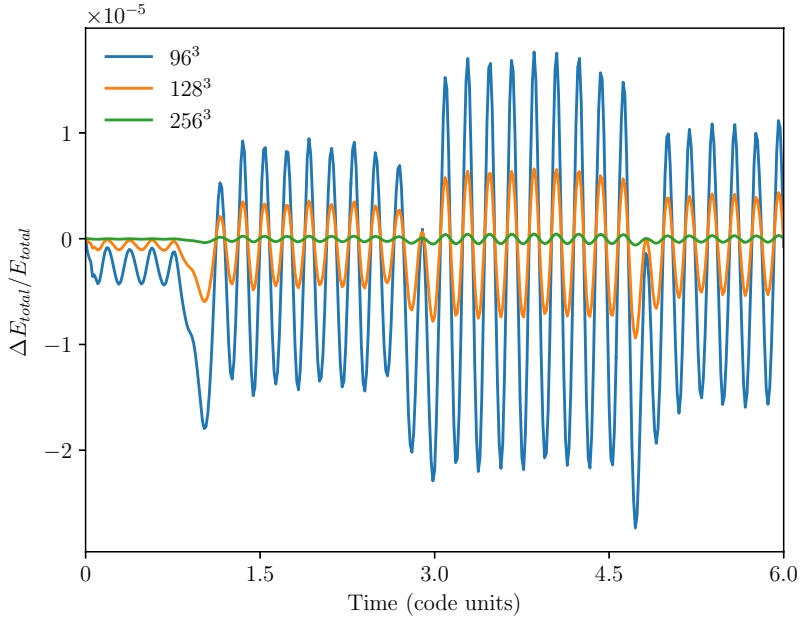

Figure 3.6: Energy conservation as a function of simulation resolution for a binary solitons orbiting their common centre of mass. ΔE_{total} is the difference between the current total energy and the initial total energy for the configuration. The ratio of this difference to the initial integrated energy is plotted on the y axis for each resolution.

$$= \int_{\mathbb{R}^3} d^3x \left\{ \frac{1}{2}\nabla(\Phi\nabla\Phi) - \frac{1}{2}\Phi\nabla^2\Phi + \Phi|\psi|^2 + \frac{1}{2}\nabla(\psi^*\nabla\psi) - \frac{1}{2}\psi^*\nabla^2\psi \right\} \tag{3.36}$$

$$= \int_{\mathbb{R}^3} d^3x \left\{ \frac{1}{2}\Phi|\psi|^2 - \frac{1}{2}\psi^*\nabla^2\psi \right\}, \tag{3.37}$$

where in the last step we have used Stokes' Theorem as well as the Poisson equation (3.9) to perform simplifications. Because we are working with the dimensionless quantities defined in equation 3.7, it is easy to see that this quantity is related to the physical energy through multiplication by a constant factor of $L^5T^{-4}G^{-1}$. It should be noted that equation 3.37 is not equivalent to the expectation value of the Schrödinger Hamiltonian, which is itself not a conserved quantity of the Schrödinger-Poisson system and is given by

$$\langle \hat{H} \rangle = \int_{\mathbb{R}^3} d^3x \left\{ \Phi|\psi|^2 - \frac{1}{2}\psi^*\nabla^2\psi \right\}. \tag{3.38}$$

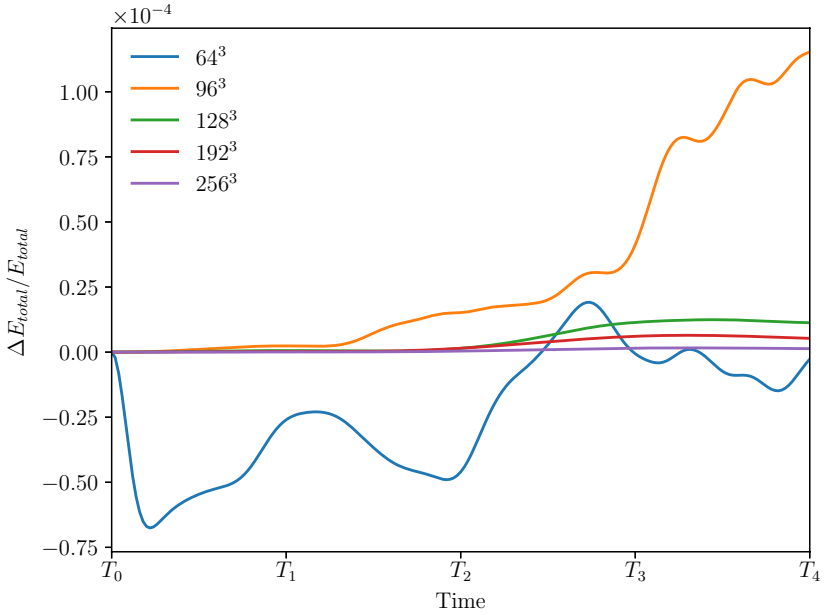

Figure 3.7: Energy conservation as a function of simulation resolution for a soliton undergoing significant tidal disruption in a Newtonian central potential. ΔE_{total} is the difference between the current total energy and the initial total energy for the configuration. The ratio of this difference to the initial integrated energy is plotted on the y axis for each resolution.

The two terms in the integral 3.37 are calculated separately within the code. The first term is the gravitational potential energy of the Schrödinger-Poisson system, E_{GP}. As discussed in [117], the second term may be decomposed into contributions which may be considered separately as kinetic and 'quantum' energies, E_K and E_Q. However, for our purposes it is sufficient to consider only their combined contribution. When PyUltraLight includes the central potential of a central point mass we have additional energy contributions. The gravitational potential energy from self-interactions is calculated separately from the gravitational potential energy due to the central potential.

Figures 3.4 and 3.5 demonstrate energy conservation for two scenarios. The first case shows the evolution of the energy of a single soliton undergoing significant tidal disruption within a Newtonian central potential. For this simulation a soliton of mass 12 in code units was initialised at a radial distance of 3 code units from the centre of a Newtonian central potential generated by a central mass of 1000

code units. As the soliton is disrupted, the kinetic energy increases, while the gravitational energy due to the central potential decreases, as expected. Meanwhile, the gravitational potential energy from self-interactions gradually increases toward zero as the disruption continues. In this case the sum of the individual energy components is conserved to 1 part in 10^6 at a resolution of 256^3.

Figure 3.5 demonstrates the evolution of the energy of a binary system of solitons in elliptical orbits around their common centre of mass over three orbital periods. In dimensionless code units, the soliton masses are 22, the initial separation 2, and the initial relative velocity was 3.6. At points of closest approach the kinetic energy increases as the solitons speed up, while the potential energy due to self-interaction decreases commensurately such that the total energy is conserved. In this scenario no central potential has been included. As the solitons reach the first point of closest approach, they become slightly deformed, exciting oscillatory modes which are manifested in Figure 3.5 as small scale oscillations superposed on the global behaviour. Figure 3.6 demonstrates the relationship between the total integrated energy and the grid resolution for the same binary system of solitons used to generate Figure 3.5. The vertical axis shows the ratio of the deviation in the total energy to the initial value of the energy, where the deviation is measured as the difference between the current and initial values. Energy is conserved at sub-percent level even at low resolutions (96^3), and increasing grid resolution greatly improves accuracy.

Figure 3.7 demonstrates the improvement in energy conservation with increasing grid resolution for a single soliton tidally disrupted in a Newtonian central potential, with the same set up as used in Figure 3.4. Namely, a single soliton of mass 12 code units is initialised at a distance of 3 code units from a central mass, $M = 1000$. The initial velocity of the soliton is $\sqrt{M/r}$ where r is the radial distance of the soliton from the central mass. The duration of the simulation is 0.5 code units so that the soliton undergoes significant tidal disruption as demonstrated in Figure 3.4. While we see that energy is conserved at sub-percent level even for 64^3 grid resolution, the qualitative behaviour of the mass density distribution in this case is not correct, so we conclude that this resolution is insufficient for convergence despite good energy conservation. This highlights the importance of a multifaceted approach to convergence testing. At 256^3, energy is conserved to parts in 10^{-6}.

3.7 Spatial and Temporal Resolution

We now examine the convergence of the ψ field configuration as a function of spatial resolution and timestep in a typical simulation. We initialise PyUltraLight with two diametrically opposed solitons orbiting a large Newtonian central potential, running until the solitons are tidally disrupted, as shown in Figure 3.8.

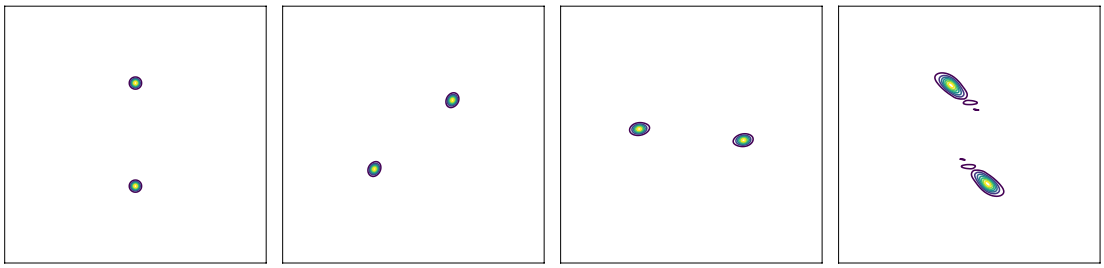

Figure 3.8: The configuration used to test the sensitivity of solutions to the spatial and temporal resolution. Two solitons of mass $m = 20$ are initialised at radial distances $r = 2$ from a central mass with $M = 1000$ moving in opposite directions with initial speeds $|v| = \sqrt{M/r}$, corresponding to clockwise orbits around the central mass. The box size is 10, while the total duration is 0.25 (all quantities in code units). Time runs from left to right.

To examine the sensitivity of the ψ field configuration to the spatial resolution, we first run at 256^3 with the default timestep. We then re-run at resolutions from 64^3 to 320^3 with the timestep fixed to the 256^3 value and downsample the final outputs to 64^3. We sort the resulting values by the density at the corresponding spatial location, and plot differences in the phase and the magnitude of ψ relative to the values of the 320^3 run as shown in Figure 3.9 (bottom). The convergence is poor at 64^3, but improves with resolution, to the point that there is little difference between the 256^3 and 320^3 cases.

To examine the sensitivity of the the ψ field configuration to the timestep, we take the same default simulation at 256^3, and then compare this to runs with timesteps 0.1, 10, and 50 times the default and down-sample the final output arrays to 64^3. We sort sort the array values in order of the ψ field magnitude in the run with the smallest timestep and in Figure 3.10 we show the difference in the phase and magnitude of ψ as a function of the timestep. The difference between the

results with the default timestep and a value 10 times smaller are negligible; and there is reasonable agreement between the default case and those with the timestep boosted by a factor of 10. However, when the timestep is increased by a factor of 50 the accuracy of both the phase and magnitude data are significantly reduced.

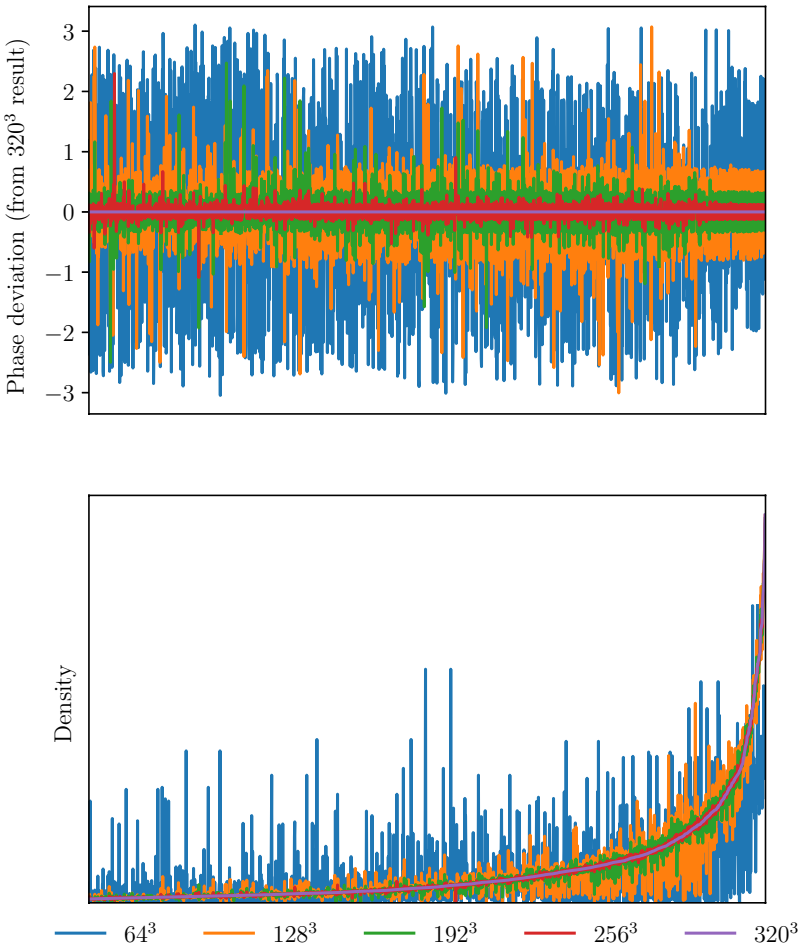

Figure 3.9: Top: Deviation of the phase of ψ compared to the highest resolution result (320^3). Field values are arranged in order of increasing magnitude from left to right. A slight improvement in phase convergence can be seen for higher density regions to the right. Bottom: Improving convergence of $|\psi|$ with increased spatial resolution for the simulation shown in Figure 3.8

Figure 3.11 shows profiles of the density through the simulation volume, as a function of spatial resolution and timestep. Each plot represents the density profile down the axis of symmetry of the initial configuration (vertical axis in Figure 3.8)

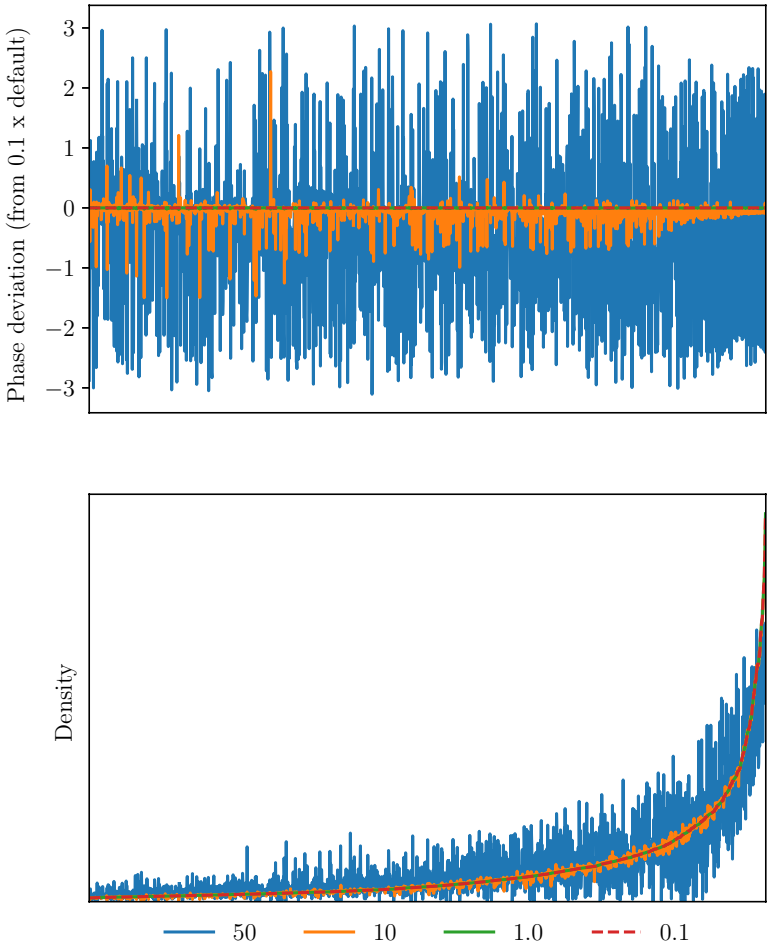

Figure 3.10: Top: Phase deviation of ψ, relative to solution with timestep 0.1 times default, sorted by the density. There is excellent agreement with the default timestep, and reasonable convergence at steps up to 10 times the default, with better accuracy in high density regions. Bottom: Difference in magnitude of ψ, relative to the solution with timestep 0.1 times default. Again we see good convergence with the default timestep, and tolerable agreement in high density regions when the step is a factor of 10 or less than default.

after approximately half a revolution around the central potential, or t=0.28 code units – slightly after the final frame in Figure 3.8 - when the solitons have become distorted due to tidal forces, but are not yet completely disrupted. We see that as the timestep is varied from 0.1 to 50 times the default value, the results with the default and the shorter timestep are virtually indistinguishable, and results are still

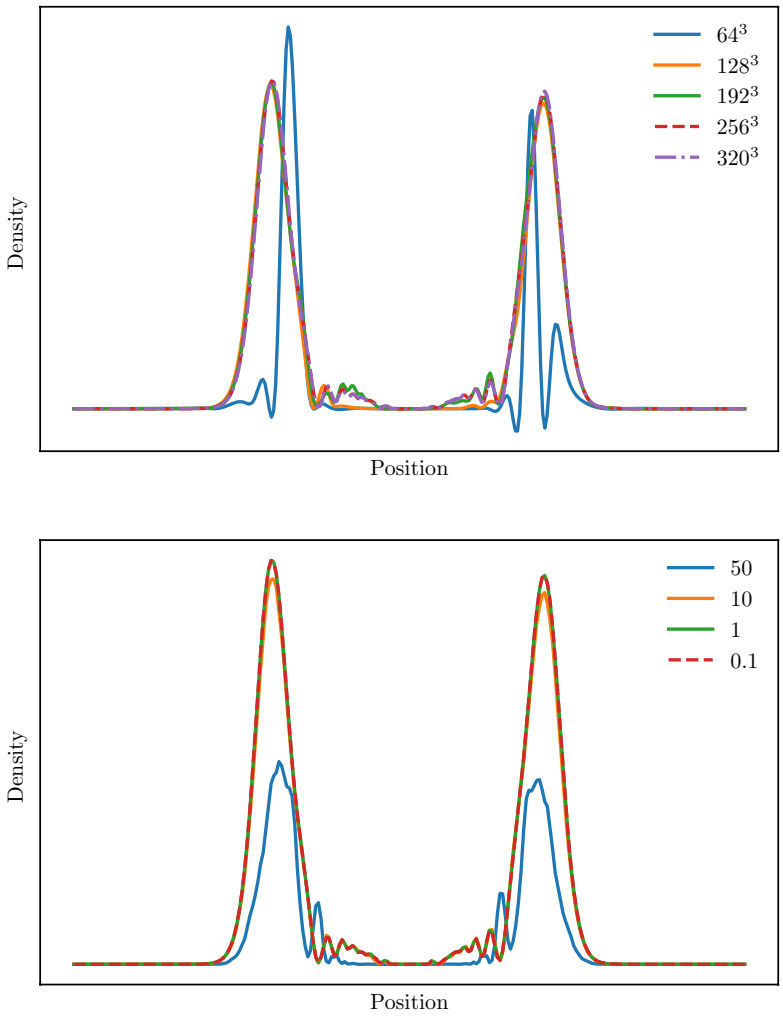

Figure 3.11: Top: Effect of decreasing the spatial resolution on the density profile at half a revolution. Bottom: Effect of increasing the timestep on the density profile at half a revolution.

reasonably accurate at 10 times the default timestep, with small deviations at high densities. We also see that as the spatial resolution is decreased from 320^3 to 64^3, the lowest resolution performs poorly, but there is good convergence at resolutions of 192^3 and above.

3.8 Discussion and Outlook

PyUltraLight is an accurate, flexible and easy to use tool for studying the dynamics of ultra-light dark matter governed by the Schrödinger-Poisson system of equations. The code makes use of a pseudospectral symmetrised split-step Fourier methodology, in which all spatial derivatives are treated via explicit multiplication in the Fourier domain, thereby avoiding difficulties associated with finite-differencing methods.

Energy conservation within PyUltraLight is excellent, at sub-percent level for simulations run at 128^3, with even better performance as resolution is increased. The code captures complex phenomena resulting from the wave-like properties of ultra-light dark matter, including the interference patterns arising during high-velocity collisions of solitonic cores, and effective forces observed in cases where the colliding cores are out of phase. These phenomena can be clearly observed at relatively low spatial resolution, avoiding the need for high-performance computing infrastructure to study the fundamental behaviour of ULDM systems in simple configurations. This makes PyUltraLight a useful tool for investigating the dynamics of ULDM systems.

PyUltraLight is Python-based, and as such is particularly simple to understand and use. The accompanying Jupyter notebook allows for the efficient adjustment of simulation parameters, and offers a useful browser interface for quick visualisation of simulation results. While Python-based, the code makes use of low-level language resources, namely the FFTW libraries through the use of the Pythonic pyFFTW wrapper and will operate at $\sim 80\%$ efficiency on a 16 core desktop workstation, suggesting that it is computationally efficient.

The current implementation of PyUltraLight is already a useful tool for simulating dynamical ULDM systems and exploring their dynamics. However, there is much scope for improvement. In particular, future releases may incorporate a variable timestep and more sophisticated physics, including explicit self-interactions in the axion sector or additional matter components. Augmented versions of the code may also include higher-order generalisations of the pseudo-spectral method, such as those used in [187].

Since its release, the utility of PyUltraLight has been confirmed as the code

has been used and adapted by a number of research groups. Of particular interest is a variation of PyUltraLight implemented in the Chapel programming language [188]. Named chplUltra, development of this code is described in Ref. [169]. This implementation is easily scalable, with successful testing completed in both simple laptop-only simulations as well as large simulations on high-performance Chapel infrastructure utilising hundreds of processors. chplUltra is currently being used to study mergers within binary ULDM systems [189] (in preparation).

A further interesting adaptation of PyUltralight is presented in Ref. [190]. In this case, the code is modified in order to simulate the interaction of ULDM solitons with a black hole. This is of particular interest given that many observed galaxies tend to possess a supermassive black hole at their centre, at which point a ULDM halo is typically thought to be solitonic in nature. Interestingly, this adaptation of PyUltraLight was used to demonstrate that black holes in the centres of solitons exhibit stochastic motion driven by excitations to the ULDM field sourced by the ULDM-black hole interactions. Evidence of novel phenomena such as this motivate further studies of this kind, perhaps utilising more sophisticated modifications of PyUltraLight. Indeed, interest in this topic has already begun to build; see, for example, [191].

Recently, yet another adaptation of PyUltraLight has been developed, named PySiUltraLight [192]. In this case a quartic self-interaction term is included in order to explore a wider class of ULDM models.

We also note that PyUltraLight has proven useful for modeling physics outside of ULDM. In particular, a generalisation of PyUltraLight has been used to model the gravitational fragmentation of the inflaton condensate [193]. This study of nonlinear dynamics in the very early universe illustrates the broad applicability of the PyUltraLight tool.

It is anticipated that additional variations of PyUltraLight will continue to be developed, with the features of each variation tailored to a particular problem in ULDM physics. While PyUltraLight is particularly useful for simulations of galactic scale physics, it is not well-adapted to large scale cosmological simulations in an expanding background. This is due to the fixed resolution of the computational grid, which corresponds to decreasing spatial resolution as the physical size of the simulation region increases with time. In Chapter 5, I will introduce

a recently developed ULDM simulator which employs adaptive mesh refinement (AMR) to overcome this obstacle. Tools which make use of AMR are bulky and necessarily more computationally expensive, so while they have the advantage of variable resolution, there remains a demand for simple, standalone tools such as PyUltraLight for addressing a variety of problems in ULDM physics. Indeed, we are currently aware of a variety of ongoing projects in which PyUltrLight is being employed.

Chapter 4

The Core-Cusp Problem Revisited: ULDM vs. CDM

This chapter is an adaptation of

Emily Kendall and Richard Easther
The core-cusp problem revisited: ULDM vs. CDM
Publ. Astron. Soc. Austral. 37 (2020) [10]

4.1 Introduction

As discussed in Chapter 1, the CDM dark matter model successfully accounts for the large scale structure of the universe [194] and the spectrum of anisotropies in the microwave background [195, 196, 197, 198, 199, 18, 200]. Nevertheless, the so-called "small-scale crisis" remains a challenge [90]. A key issue is the apparent tension between the central density profiles of dark matter halos in simulations containing only gravitationally interacting CDM, and those inferred from observational data. Simulations tend to produce 'cuspy' central density profiles [92], which grow as $1/r$ at small radii, but observational data appears to favour flattened central cores [201]. The tension between the two is widely known as the "core-cusp problem" [202, 203, 96].

The seriousness of the core-cusp problem is the subject of ongoing debate, see, for example, Ref. [204]. Nevertheless, the wider category of "small-scale" problems in standard CDM, along with tighter constraints from direct-detection experiments [205], motivate the study of alternative dark matter models such as ULDM, which may naturally ameliorate tensions on small scales due to macroscopic quantum phenomena.

As reviewed in Ref. [117], current constraints prefer a ULDM particle mass of $\mathcal{O}(\sim 10^{-22}\text{eV})$, corresponding to a kiloparsec-scale de Broglie wavelength. ULDM thus exhibits novel wave-like behaviour on astrophysically interesting scales. ULDM simulations suggest that realistic astrophysical halos have an inner core consisting of a kiloparsec-scale Bose-Einstein condensate, surrounded by a virialised outer halo [146, 128]. The outer region resembles a standard CDM halo, which is well approximated by the Navarro–Frenk–White (NFW) profile characteristic of collisionless CDM, and most commonly associated with WIMP dark matter [92]. Because the (solitonic) profiles of the inner condensates are smooth, it has been suggested that ULDM can resolve the core-cusp problem without the need to invoke baryonic astrophysics. However, solitonic density profiles obey an inverse mass-radius scaling law. Therefore, it has been suggested that the density of the ULDM halo might, in fact, exceed that of an analogous NFW halo over a finite range of small radii in larger galaxies. In particular, Ref [133] concludes that CDM-only NFW profiles may outperform ULDM profiles for galaxies with halo masses $\mathrm{M_h} \gtrsim 10^{11}\mathrm{M_\odot}$.[1]

To further explore the possible worsening of the core-cusp problem in ULDM, we examine the effect of scatter in the core-halo mass scaling relation. Starting from the semi-analytic density profile of Ref. [133], we look at the scatter in the parameters implied by Ref. [132]. We show that the resulting statistical variability may ease concerns that the core-cusp problem is exacerbated for ULDM relative to CDM for "large dwarf" galaxies.

Our analysis also highlights a number of caveats that apply to all such discussions. First, the incoherent outer regions of ULDM halos are subject to strong fluctuations, both temporally and spatially. These are not captured by semi-analytic halo density

[1]Ref [133] refers to these galaxies as "large dwarfs", though we note that the upper limit on this category is around $10^{12}\mathrm{M_\odot}$, approaching estimates of the Milky Way mass [206].

profiles and we argue that these fluctuations may accentuate the intrinsic scatter in halo parameters. Moreover, baryonic feedback is known to be significant for dwarf galaxies [97, 204] and neither the NFW or ULDM profiles incorporate this effect. Consequently, we caution against attempting to discriminate between ULDM and CDM models based on DM-only simplified theoretical profiles.

Observationally, we find that neither semi-analytic ULDM halos (for ULDM particle mass $0.8 - 2.5 \times 10^{-22}\,\mathrm{eV}$) nor NFW halos provide a particularly convincing fit to rotation curves of large dwarf galaxies in the SPARC database [113]. Moreover, many rotation curves are extracted from a few data points with significant uncertainties and which only span a small range of radial distances, further complicating attempts to draw robust conclusions. These issues are exacerbated by the relatively large number of free parameters in the theoretical models. For instance, a ULDM mass parameter of $10^{-23}\,\mathrm{eV}$ seemingly ameliorates the core-cusp problem in galaxies exhibiting a steep decrease in rotation velocity at small radii, but such a small mass is in tension with other constraints. Consequently, the primary conclusion to be drawn from this type of parameter-fitting exercise seems to be that analyses of the core-cusp problem (and potentially other "small scale" anomalies) based on simplified semi-analytic DM-only models cannot meaningfully test these scenarios, especially when observational data is limited and detailed numerical simulations with baryonic feedback are lacking.

The structure of this chapter is as follows. In Section 4.2, we review the construction of semi-analytic density profiles for both the ULDM and CDM models and briefly discuss aspects of realistic ULDM halos which are not captured by the semi-analytic model. In Section 4.3 we compare the semi-analytic density profiles for ULDM and CDM halos in the dwarf galaxy mass range $10^{11} - 10^{12}\,\mathrm{M}_{\odot}$, taking into account statistical variation in both the NFW concentration parameter and the ULDM core-halo mass relation. We then compare the radial velocity profiles inferred from these density profiles with astrophysical data from the SPARC database [113]. We conclude in Section 4.5.

4.2 Semi-Analytic Halos

We begin by looking at the semi-analytic parametrisations of ULDM and CDM halos. The well known NFW profile of CDM [92, 207] is given by

$$\rho_{\rm NFW}(r) = \frac{\rho_0}{\frac{r}{R_s}\left(1+\frac{r}{R_s}\right)^2}\,. \tag{4.1}$$

At small radii the profile is proportional to $1/r$, while at large radii it goes as $1/r^3$. The parameters ρ_0 and R_s vary from halo to halo; ρ_0 can be interpreted as a characteristic density, while R_s is the scale radius and determines the distance from the centre at which the transition between the 'small r' and 'large r' limits occurs.

The NFW halo is assumed to be radially symmetric, and requires truncation at a finite radius in order to prevent the integrated mass diverging as $r \to \infty$. The truncation is typically set by the virial radius, which is itself determined approximately via the spherical top-hat collapse model describing the evolution of a uniform spherical overdensity in a smooth expanding background [140, 208, 209]. Gravitational collapse of the overdensity halts when virial equilibrium is reached. In this scenario the corresponding virial radius is the radius at which the mean internal density is $\Delta_c \rho_{\rm crit}(t)$. Here $\rho_{\rm crit}(t)$ is the critical density of the universe at time t. The factor Δ_c is of order 10^2 and while different conventions exist, we make the common choice $\Delta_c = 200$ [210] in what follows.

Once the virial radius is specified as the outer limit of the halo, Equation 4.1 completely determines the density profile for given ρ_0 and R_s. For any given virial mass, there is a range of corresponding NFW density profiles, with the distributions of ρ_0 and R_s emerging from the mass-concentration-redshift relation seen in N-body simulations and observations [211, 212].

Whereas CDM halos can be described by NFW distributions, a different approach must be taken in the case of ULDM. ULDM dynamics is governed by the Schrödinger-Poisson system of coupled differential equations. In a static background, they take the dimensionless form

$$i\dot{\psi} = -\frac{1}{2}\nabla^2\psi + \Phi\psi, \tag{4.2}$$

$$\nabla^2\Phi = 4\pi|\psi|^2, \tag{4.3}$$

where ψ is the ULDM wavefunction, Φ is the Newtonian potential, and the density $\rho \propto |\psi|^2$. The solitonic ground state profile cannot be written down analytically, but given a numerically computed spherically symmetric profile ψ for $\psi(0) = 1$, the full family of solutions is then given by

$$\psi'(x) = \gamma\psi(\sqrt{\gamma}x), \tag{4.4}$$

where γ is a scaling parameter and the dimensionless mass of the soliton is proportional to $\sqrt{\gamma}$, while the dimensionless radius is proportional to $1/\sqrt{\gamma}$. The dimensionless density $|\psi|^2$ and dimensionless radius x can be transformed into dimensionful quantities by

$$\rho = \mathcal{M}\mathcal{L}^{-3}|\psi|^2, \tag{4.5}$$

$$r = \mathcal{L}x, \tag{4.6}$$

where

$$\mathcal{L} = \left(\frac{8\pi\hbar^2}{3m^2H_0^2\Omega_{m0}}\right)^{\frac{1}{4}} \approx 121\left(\frac{10^{-23}\,\mathrm{eV}}{m}\right)^{\frac{1}{2}}\mathrm{kpc}, \tag{4.7}$$

and

$$\begin{aligned}\mathcal{M} &= \frac{1}{G}\left(\frac{8\pi}{3H_0^2\Omega_{m0}}\right)^{-\frac{1}{4}}\left(\frac{\hbar}{m}\right)^{\frac{3}{2}} \\ &\approx 7\times10^7\left(\frac{10^{-23}\,\mathrm{eV}}{m}\right)^{\frac{3}{2}}\mathrm{M}_\odot\,.\end{aligned} \tag{4.8}$$

Ref. [133] gives a piecewise parameterization of the generic ULDM profile

$$\rho(r) = \begin{cases}\rho_{\mathrm{sol}}(r), & 0 \le r \le r_\alpha \\ \rho_{\mathrm{NFW}}(r), & r_\alpha \le r \le r_{\mathrm{vir}},\end{cases} \tag{4.9}$$

where $\rho_{\mathrm{sol}}(r)$ is the appropriately scaled density profile of the ground state soliton solution. The contribution from the solitonic core and the overall virial mass is predicted to obey a scaling relationship [132, 135] which sets the central density,

ρ_c, of a ULDM halo with virial mass, M_{vir}. This yields an expression relating the core size to the velocity dispersion, and finally to the halo virial mass.[2]

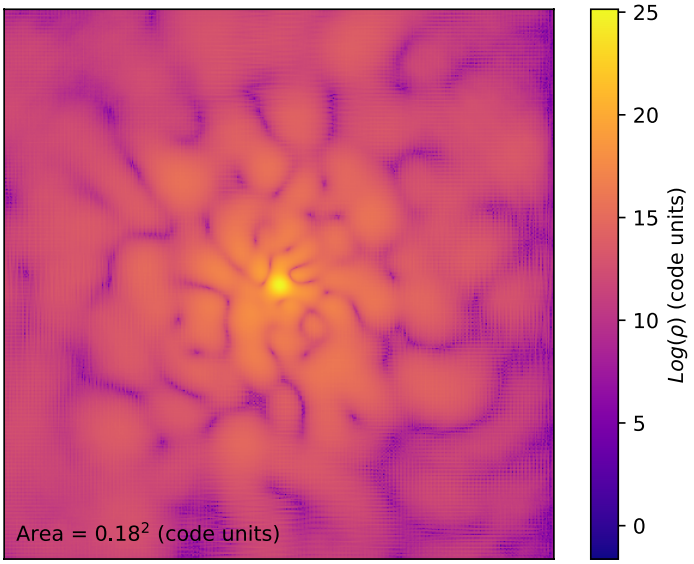

Figure 4.1: Illustration of the scale of the fluctuations present in the incoherent outer halo for a merger of 8 randomly located solitons. The contour plot represents the ($\log_{10}$ scaled) local density across a slice through the centre of the final halo. In this plot, distance is not log-scaled, and we see that the spatial size of the fluctuations is of the same order of magnitude as the solitonic core itself.

This core-halo mass relation was introduced in Chapter 2 and can be understood simply by matching the virial velocities of the core and the wider halo (see Appendix B for details). At $z = 0$, we may recast Equations 2.68 and 2.70 from Chapter 2 to

[2]The authors of [132] suggest the following general expression:

$$M_c = \alpha \left(|E|/M\right)^{1/2}, \tag{4.10}$$

where the core mass M_c is determined by the total energy, E, and the total mass of the halo, M where α is a constant of order unity. They then explain that the right hand side of the equation represents the halo velocity dispersion, while the left hand side represents the inverse core size due to soliton scaling laws. By invoking the virial condition of the spherical collapse model, the authors then construct the redshift dependent relationship between the solitonic core mass and the halo virial mass for a ULDM halo.

obtain:

$$\rho_c = 2.9 \times 10^6 \, \mathrm{M}_\odot \, \mathrm{kpc}^{-3} \left(\frac{\mathrm{M_{vir}}}{10^9 \mathrm{M}_\odot} \right)^{4/3} \mathrm{m_{22}}^2, \tag{4.11}$$

and

$$r_c = 1.6 \, \mathrm{kpc} \left(\frac{\mathrm{M_{vir}}}{10^9 \mathrm{M}_\odot} \right)^{-1/3} \mathrm{m_{22}}^{-1}, \tag{4.12}$$

where r_c is the radius at which the density is half of the central value, and $\mathrm{m_{22}}$ is given by $\mathrm{m_{22}} \equiv m/10^{-22}\,\mathrm{eV}$ where m is the ULDM particle mass.

While the piecewise semi-analytic ULDM profile is a useful tool, one should be mindful of its limitations. For example, while a number of studies have attempted to establish 'universal' properties of ULDM halos, many of these analyses generated ULDM halos through the mergers of smaller compact objects [146, 158]. This method of halo assembly is not representative of a realistic structure formation process, however it has the advantage of avoiding the computational difficulty of undertaking large-scale ULDM cosmological simulations. For this reason there is currently limited information from which to draw robust conclusions about the properties of astrophysical ULDM halos. In particular, universal application of the core-halo mass relation cannot be fully justified until more work is done to understand the characteristic timescales associated with the formation of quantum pressure-supported cores in scenarios including condensation from a fluctuating background, gravitational collapse in an expanding background, and mergers of objects with and without stable central cores. Moreover, it is difficult to accurately predict the effect that baryonic feedback will have on the formation of solitonic cores in halos of different masses, which could be significant at small radii in the present context.

Halo substructure is likewise missing from the semi-analytic model presented above. In simulations of soliton mergers the resulting halos have turbulent outer regions, with fluctuations on scales comparable to the core size, as illustrated in Figure 4.1. In addition to the fluctuations inherent in a large ULDM halo, smaller halos are likely to orbit or interact with larger halos. This substructure is not captured by the semi-analytic model described above, and predictions for tracer velocity profiles may thus not match those of realistic astrophysical objects. Furthermore, temporal fluctuations in the core density are also missing from the

semi-analytic model. Realistic halo cores are not exact soliton solutions of the Schrödinger-Poisson equation, they interact non-trivially with the fluctuating NFW-like outer halo, and their central densities can vary with time by as much as a factor of two [128].

Taken together, these limitations suggest that the core-halo mass relation of the semi-analytic model should not be interpreted as an inviolable rule, but as a statement about the averaged characteristics of a statistical distribution. To estimate the variance corresponding to this distribution, we can consider a range of possible central densities for a given virial mass (somewhat analogous to the scatter in NFW concentration parameters [207]). The results of Ref. [132] indicate that a scatter in the core mass M_c of up to $\pm 50\%$ is possible for a given virial mass. Unfortunately, the small sample size and limited halo mass range ($M_{vir} \approx 10^8 - 10^{11}\, M_\odot$) found in [132] preclude a detailed analysis of the statistical properties of realistic astrophysical halos, but future simulations (especially those including baryonic feedback) should lead to improved predictions for this distribution.

To partially account for statistical variance in halo properties, one can allow for variation in the radius at which the solitonic profile of the ULDM halo transitions into an NFW profile. This is acknowledged in Ref [133] and is captured by the parameter α: the transition radius, r_α, is given by $r_\alpha = \alpha r_c$, with $3 \leq \alpha \leq 4$. For a given theoretical halo, an adjustment to the transition radius should be accompanied by changes in the parameters of the outer NFW halo, so as to maintain the core-halo mass ratio.

Thus, by taking the central soliton density and transition radius as variable parameters, we can create a range of plausible ULDM halo profiles for a given halo by using the virial mass to predict ρ_c, and assuming variation of $\pm 50\%$ around this central value. Given specific values for the central density and transition parameter α, the solitonic piece of the ULDM profile is then completely specified, and its mass can be calculated. The remainder of the virial mass must be accounted for by the NFW tail of the profile. By matching the densities of the NFW tail to the inner soliton at the transition radius, the values of R_s and ρ_0 for the NFW tail are obtained.

4.3 ULDM and CDM Halos and Astrophysical Data

We now compare the radial profiles of ULDM halos to NFW halos using the semi-analytic profiles described above, focusing on masses in the range 10^{11} and $10^{12}\,\mathrm{M}_{\odot}$, which may show an apparent worsening of the core-cusp problem [133]. Figure 4.2 compares such halos; the shaded blue region represents the ULDM halos for which the core-halo mass relation has a scatter $\mathrm{M}_c = \mathrm{M}_{\mathrm{cp}} \pm 50\%$ range, where M_{cp} is the theoretical prediction for the core mass. Note that because higher central densities correspond to narrower soliton profiles, the shaded region possesses 'crossover points' near the transition from the solitonic to NFW profile, appearing somewhat skewed from the median line. Were we to vary more parameters in the model (such as transition radius and axion mass), we would see a broadening of the shaded region, such that the median line would be fully encompassed by the shaded region. Because we are here focusing primarily on the core mass (and therefore central density), we illustrate only the changes in density profile attributable to this, hence the restricted range of profiles shown as the shaded blue region.

The Schrödinger-Poisson soliton scaling relations show that the $\mathrm{M}_c = \mathrm{M}_{\mathrm{cp}} \pm 50\%$ mass range corresponds to a range of $\gamma_p/4 \leq \gamma \leq 9\gamma_p/4$, where γ_p is the theoretical prediction of the square root of the dimensionless central density. Consequently, there is a large variation in the central density and thus widely varying predictions for the ULDM profiles. We fix $\alpha = 3.5$ (in the middle of the predicted range) which does not affect the central density as the core lies well within the solitonic region. Changing the value of α will, however, affect the predicted velocity profiles for each halo. We do not attempt to fit this parameter to data in this Section; the previously discussed limitations of the semi-analytic models employed here suggest that this would be unlikely to be a meaningful exercise. The blue ULDM profiles are compared to the red shaded regions of Figure 4.2, showing the 2σ variation about the theoretical prediction for the concentration parameter of the NFW halo with the same virial mass [207].

Following Ref [133], we plot to a minimum radius of $r/r_{\mathrm{vir}} = 10^{-4}$ and for the same choices of m_{22}. For any $\mathrm{M}_{\mathrm{vir}}$, the NFW halo density will inevitably exceed that of the ULDM halo at very small radii, though the threshold for this transition

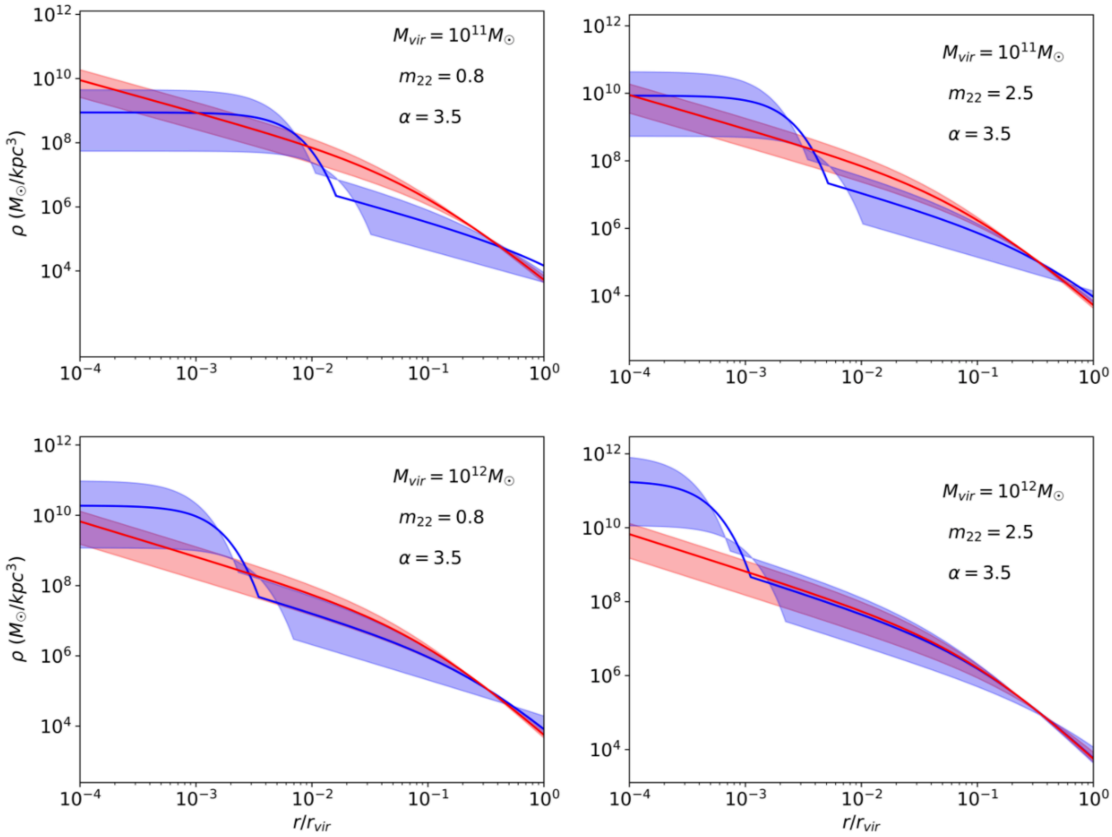

Figure 4.2: Density profiles as a function of radius (normalised to the virial radius) for ULDM and NFW halos of masses $10^{11}\,M_\odot$ (top) and $10^{12}\,M_\odot$ (bottom). The left panel represents the results for $m_{22} = 0.8$, while the right panel corresponds to $m_{22} = 2.5$. The transition radius is fixed at $r_\alpha = 3.5 * r_c$. The blue shaded region represents the ULDM profile with $M_c = M_{cp} \pm 50\%\, M_{cp}$, while the solid blue line represents the ULDM profile when the theoretical core-halo mass relation is taken to be exact. The red shaded region represents the range of NFW profiles for a halo of the same virial mass with a 2σ variation around the median (solid red line).

may be arbitrarily small, and not observationally relevant. However, we note that the apparent worsening of the core-cusp discrepancy does depend on the choice of inner radial cutoff.

From Figure 4.2 we see that for halo masses of $10^{11}\,M_\odot$ there is a wide range of M_c for which the ULDM profile is 'less cuspy' than its NFW counterpart. For a halo mass of $10^{12}\,M_\odot$ and a ULDM particle mass $m_{22} = 0.8$ the range of plausible ULDM profiles likewise includes those which are 'less cuspy' than the corresponding NFW profile. At higher particle mass ($m_{22} = 2.5$) for $10^{12}\,M_\odot$ halos, the NFW profiles

tend to be less peaked than corresponding ULDM profiles at radial distances in the range $10^{-4} \leq r/r_{\rm vir} \leq 1$.

To assess the suitability of these semi-analytic profiles, we compare to observations drawn from the SPARC database. Because observations yield the (line of sight) velocity distributions of tracer stars as a function of galactocentric radius rather than the halo density itself, we must first transform our theoretical density profiles into velocity profiles. In so doing, we acknowledge that the effects of non-circular motion and kinematic irregularities constitute a non-trivial source of random error in observed velocities, which should be kept in mind especially when working with limited data sets.

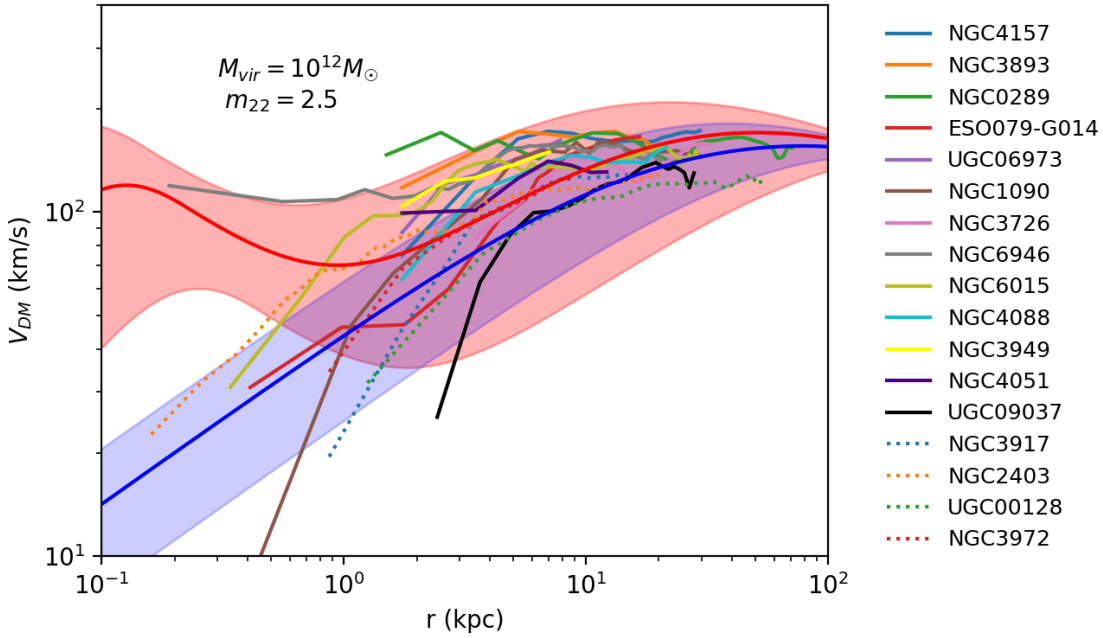

Figure 4.3: Velocity distributions for galaxies with maximum velocities in the range $125 \leq v < 175\,\mathrm{km s^{-1}}$ in the SPARC database. Data at innermost radii is limited for these galaxies, making it difficult to determine the overall characteristics of the profiles. The SPARC data is plotted alongside theoretical NFW (shaded blue) and ULDM (shaded red) profiles, assuming a virial mass of $10^{12}\mathrm{M}_\odot$, $\mathrm{m}_{22} = 2.5$, and $\pm 50\%$ scatter in the ULDM core-halo mass relation and $\pm 2\sigma$ scatter in NFW concentration. Galaxies in the legend are ordered from highest maximum velocity (top) to lowest (bottom).

We convert density profiles to velocity distributions [213] via

$$V(r)^2 = \frac{4\pi G}{r} \int_0^r \rho(r') r'^2 dr', \tag{4.13}$$

where

$$V^2 = V_{\rm disk}^2 + V_{\rm bulge}^2 + V_{\rm gas}^2 + V_{\rm halo}^2. \tag{4.14}$$

The SPARC database contains photometric data for 175 galaxies and rotation curves from $\mathrm{H_I}/\mathrm{H}_\alpha$ studies. The disk and bulge velocities in the SPARC database are given for $\Upsilon = 1\,\mathrm{M}_\odot\,/\,\mathrm{L}_\odot$ at $3.6\,\mu$m. However, the greatest source of uncertainty in mass modelling is the assumed stellar mass-to-light ratio, $\Upsilon_\star$ [113]. As in [133], we assume a constant value of $\Upsilon_\star = 0.2\,\mathrm{M}_\odot\,/\,\mathrm{L}_\odot$ at $3.6\,\mu$m, likewise noting that this constitutes a non-trivial source of uncertainty. Moreover, there is significant uncertainty in the SPARC data itself. Error bars are omitted in the following graphs for ease of viewing, however, they are discussed in Section 4.6.

The characteristics of the velocity profiles in the SPARC database vary widely from galaxy to galaxy; however we qualitatively identify two subsets of galaxies; those with maximum tracer velocities $75 \leq v < 125\,\mathrm{kms}^{-1}$, and those for which $125 \leq v < 175\,\mathrm{kms}^{-1}$. The former group tends to exhibit a strong steepening in the radial velocity profile toward the inner halo, while the profiles for the latter group are comparatively flat[3]. We assume that higher asymptotic velocities correspond to a larger halo mass, and consider halo masses in the range $10^{11} - 10^{12}\,\mathrm{M}_\odot$, expecting that masses at the top end of the range will give a better match to galaxies with higher asymptotic velocities.

In Figure 4.3, we see that galaxies with asymptotic velocities at the higher end of the range do not always exhibit a pronounced steepening of the velocity profile at small radii. Indeed in some cases there is simply no data at small radii. From this figure we see that while a halo mass of $10^{12}\mathrm{M}_\odot$ with $\mathrm{m}_{22} = 2.5$ provides a reasonable fit to the data at radii > 10kpc, it is difficult to judge the fit at small radii, where the ULDM and NFW profiles differ most strongly, due to a lack of data. Furthermore, while the data at higher radii seems to be relatively clustered, there are significant deviations within the limited data that exists at small radii. For

[3]We exclude data for which the velocities calculated according to Equation 4.14 are inconsistent - this can occur due to the uncertainty in the assumption for $\Upsilon_\star$.

example, the curves for NGC1090 and NGC6946 are widely disparate at small radii, but seem to converge at larger radii. Attempting to fit such data to a single set of model parameters would be of limited utility without a much more comprehensive data set from which statistical outliers could be properly identified. Furthermore, we note that there are substantial changes in theoretical ULDM velocity profiles under variation in the ULDM particle mass. The scale of these changes is exhibited in 4.4. As such, we remark that analyses of the sort presented here would benefit greatly from tighter constraints on the ULDM particle mass.

By contrast, for galaxies with smaller maximum velocities ($75 \leq v < 125\,\mathrm{kms}^{-1}$), there is more data at smaller radii. For such galaxies we see the steepening rotation curves characteristic of cored density profiles, as shown in Figure 4.4. In this case, choosing parameters such that the theoretical profiles overlap with the data at small radii is easy (in this case $\mathrm{m}_{22} = 0.1$, $\mathrm{M}_{\mathrm{vir}} 5 \times 10^{11} \mathrm{M}_{\odot}$), however it is not clear whether the behaviour of this profile would fit data at larger radii were it available. Furthermore, while the choice $\mathrm{m}_{22} = 0.1$ provides a reasonable fit to the data in this case, a ULDM particle mass $\mathrm{m}_{22} = 0.1$ is in tension with constraints from the Lyman-α forest, as well as high-redshift UV luminosity function comparisons[4] [214, 215, 216, 217, 218]. It must be acknowledged, however, that baryonic feedback is expected to have the greatest impact in the innermost regions of realistic halos. As such, agreement between our semi-analytic DM-only model and observational data at small radii should be interpreted cautiously, especially since this is also the region where assumptions regarding the stellar mass to light ratio have the greatest significance.

4.4 Impact of ULDM Particle Mass on Halo Velocity Profiles

Figure 4.5 demonstrates the scale of the changes to the velocity profiles of theoretical ULDM halos under changes in the ULDM particle mass. In order to perform a meaningful parameter fitting exercise, observational data would be required to span the wide range of radii illustrated here. In this way, the regions of the rotation

[4] $0.8 < \mathrm{m}_{22} < 2.5$ is preferred by current constraints, as mentioned in [133]

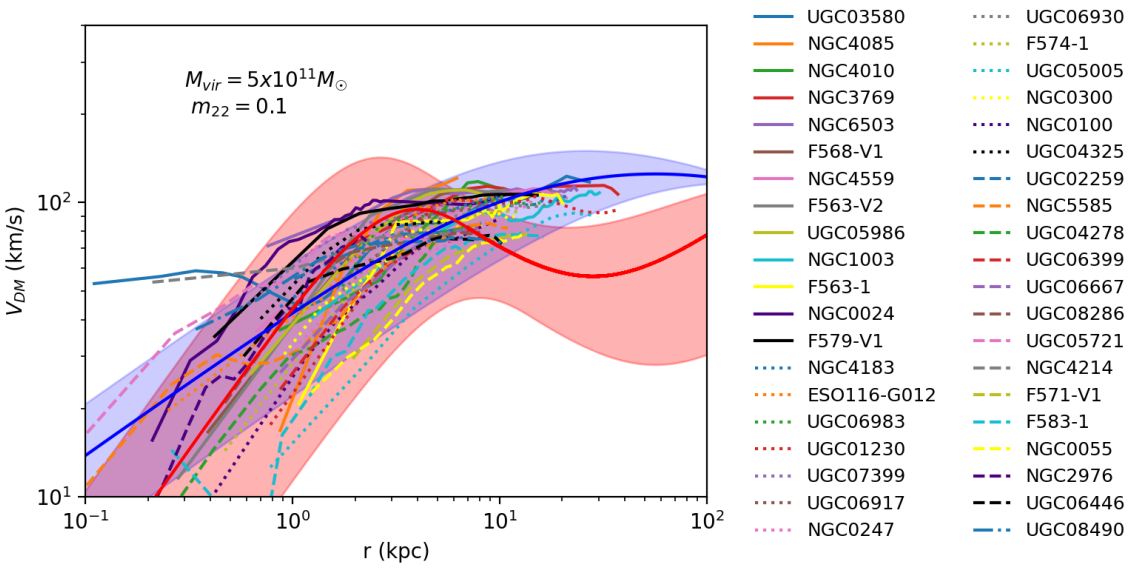

Figure 4.4: Velocity distributions for galaxies with maximum velocities in the range $75 \leq v < 125\,\mathrm{kms}^{-1}$ in the SPARC database. Data at outer radii is limited for these galaxies, making it difficult to determine the overall characteristics of the profiles. The SPARC data is plotted along with theoretical NFW (shaded blue) and ULDM (shaded red) profiles, assuming a virial mass of $5 \times 10^{11}\mathrm{M}_\odot$, $\mathrm{m}_{22} = 0.1$, and $\pm 50\%$ scatter in the ULDM core-halo mass relation and $\pm 2\sigma$ scatter in NFW concentration. Galaxies in the legend are ordered from highest maximum velocity (top left) to lowest (bottom right).

curves most sensitive to the assumption for the ULDM particle mass could be tested simultaneously. Presently available data, when binned according to e.g. maximum velocity, is likely to yield disparate preferences for the ULDM particle mass, as illustrated in Figures 4.3 and 4.4. Further work to constrain the plausible range of the particle mass will make comparisons of the ULDM and CDM models with astrophysical data more effective.

4.5 Conclusions

The ULDM model has gained attention in part because it may offer a solution to the CDM core-cusp problem. However, in some cases ULDM profiles can actually have higher densities than their NFW counterparts at observationally relevant

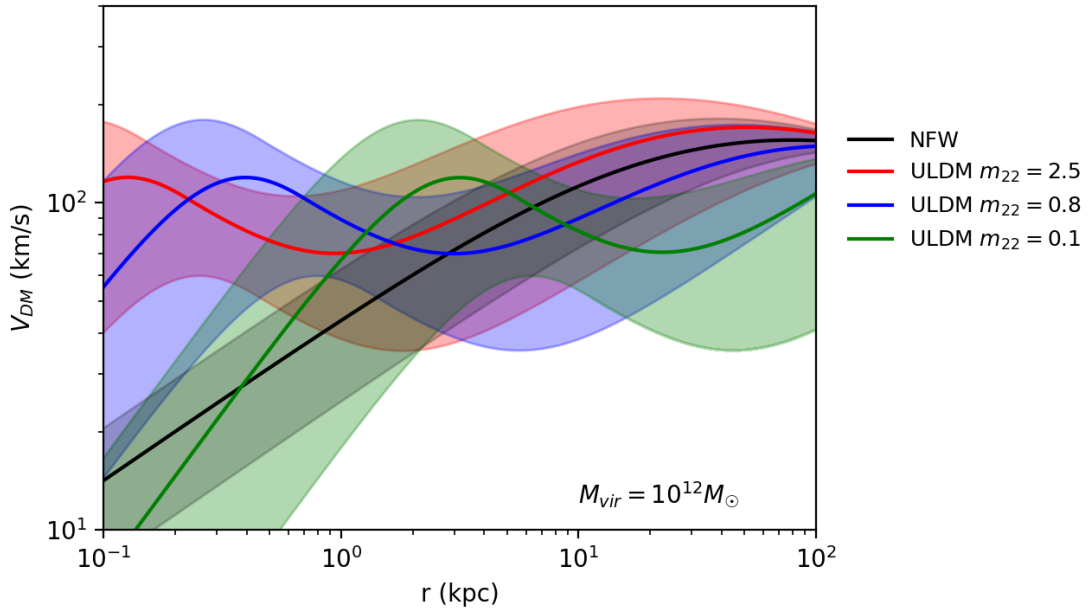

Figure 4.5: Plot demonstrating the effect of changing the ULDM particle mass assumption on the velocity profiles for halos of mass $10^{12}\mathrm{M}_\odot$.

radii in the interior of halos with mass $\mathrm{M} \gtrsim 10^{12}\mathrm{M}_\odot$, where the central density is determined by the theoretical core-halo mass relation. However, apparent statistical spread in the ULDM core-halo mass relation [132] leads to a sizeable range of plausible central densities for a halo of any given mass. Furthermore, analyses of oscillations of the cores of ULDM halos on timescales much smaller than the relaxation time have demonstrated significant fluctuations in central density [128]. This suggests that theoretical core-halo mass relations should not be interpreted too literally for any individual ULDM halo, and this should be taken into account when performing model-selection analyses. The limited available simulation data means that the exact features of the distribution of halo properties in ULDM are poorly characterised. Nevertheless, it remains apparent that core masses at the lower end of the plausible range could mitigate the apparent worsening of the core-cusp discrepancy for ULDM halos.

When the spread in the theoretical core-halo relation is accounted for, comparisons of theoretical ULDM and NFW profiles to the SPARC database yield inconclusive results as far as interior regions of the halos are concerned. Parameters

can be easily chosen to provide a superficial fit to given subsets of data. However, the available data often do not span a large enough range of radial values to assess the relative merits of the UDLM and NFW profiles over the whole profile. In particular, rotation curves in the SPARC database that exhibit a strong steepening at small radii often lack data at large radii. Conversely, rotation curves that include data at large radii often lack measurements at small radii. However, from our restricted analysis, it appears that neither the theoretical ULDM nor CDM model can reliably reproduce the data across a broad range. Wide deviations at small galactocentric radii cannot be accounted for by random measurement errors, and suggest that sophisticated modelling of baryonic physics will be necessary before any conclusions can be reasonably drawn. The lack of baryonic physics in both the semi-analytic CDM and ULDM models is significant, as are other limitations due to poorly characterised statistics and simplistic assumptions about halo modelling.

In principle, one could perform a Bayesian Information Criterion (BIC) analysis to determine which of the ULDM or NFW models is more strongly favoured by the data [219]. The model with the lowest BIC, defined as

$$\mathrm{BIC} = k \ln \mathrm{N} - 2 \ln \mathcal{L}, \tag{4.15}$$

is preferred. Here $\mathcal{L}$, N, and k are the maximised likelihood function, the sample size, and the number of model parameters, respectively. The utility of BIC or other model selection tools, however, is hampered by the lack of comprehensive data, the high number of free parameters (the stellar mass to light ratio in the SPARC data, virial mass assumptions of the galactic halos, ULDM particle mass, NFW concentration parameter, UDLM soliton to NFW transition radius and variation in the ULDM core-halo mass relation), and the omission of baryonic feedback in ULDM simulations. Indeed, BIC analyses are known to be compromised when the sample size of the data is not sufficiently large in comparison to the number of free parameters in the model. Because of this limitation, and large and unquantified systematic biases in both the observational data and theoretical predictions, such analyses are premature at this point. Previous studies such as Ref. [220] of the core-halo mass relation and the fitting of semi-analytical profiles to galaxy data also emphasise the necessarily preliminary and tentative nature of all analyses of

ULDM-derived rotation curves.

To summarise, the parameter space describing "typical" ULDM halos is larger than simple semi-analytical models suggest. It is necessary to constrain this parameter space in order to make robust model selection possible. Tightening the constraints on the plausible ULDM particle mass [221, 222, 223] and obtaining additional spectroscopic data with improved uncertainties covering a greater halo mass range and radius would be of tremendous benefit in this regard. Such improved data can be expected from future surveys [224]. In addition, better ULDM cosmological structure formation simulations are needed to improve the understanding of ULDM halo evolution [225, 226, 152] and these should also incorporate baryonic feedback. Thus, the key conclusion to be drawn from this work is that more information from simulations and astrophysical observations is needed, as is more sophisticated incorporation of baryonic effects within semi-analytic models of both ULDM and CDM, before the relative successes of each model can be fairly compared. Indeed, recent work identifies a sizeable dispersion in the core-halo mass relation for simulated ULDM halos, and finds that this dispersion increases with halo mass [227]. The authors emphasise that observational constraints on the ULDM particle mass must take into account an additional uncertainty of the order of 50% on the core-halo mass relation for halos exceeding $10^9 M_\odot$. Furthermore, recent observational studies again conclude that 'cored' central density profiles are preferred, but emphasise the need to further study dissipative processes in the gas-rich, early phases of galaxy evolution in order to fully understand the inner density profiles of galactic halos [228].

4.6 Errors in SPARC Data

As discussed in Section 4.3, the uncertainties associated with the SPARC rotation curves for the galaxies studied here make it difficult to draw robust conclusions as to the suitability of one or the other dark matter model. Indeed, sources of error quoted in the SPARC database relate not only to the random error in measured line-of-site velocities, but also to errors on the galaxy distance measurement, inclination, and total luminosity. Furthermore, inaccuracy in the assumed stellar mass-to-light ratio may lead to skewed velocity decompositions, a systematic effect that could

exceed the stochastic measurement errors.

Figures 4.6 and 4.7 show the error bars associated with the low asymptotic velocity ($75 \leq v < 125\,\mathrm{kms}^{-1}$) and high asymptotic velocity ($125 \leq v < 175\,\mathrm{kms}^{-1}$) measurements, respectively.

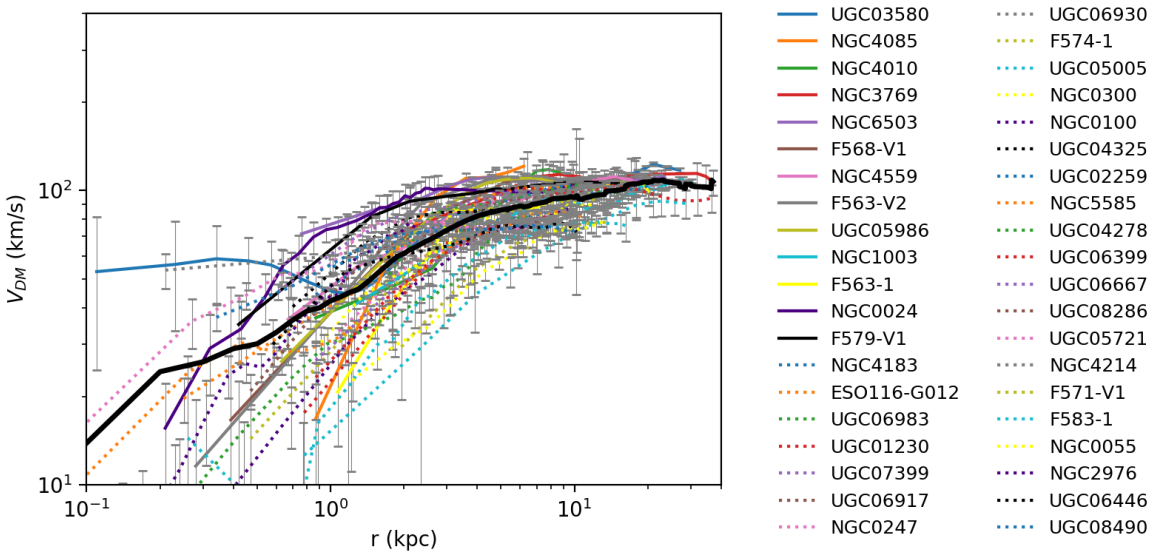

Figure 4.6: Radial distributions for galaxies with maximum velocities in the range $75 \leq v < 125\,\mathrm{kms}^{-1}$ in the SPARC database. The average velocity curve is shown by the bold black line. Large uncertainties coupled with a wide spread of data at small radii limit the utility of this data set for determining the precise details of small scale structure in dark matter halos.

In Figure 4.6, we see large error bars at small radii. It is precisely this regime in which accurate velocity profiles are needed to assess the significance of the core-cusp discrepancy - a key differentiating factor between ULDM and CDM models as illustrated in Figure 4.4. Hence, more comprehensive, accurate data in this regime would be of tremendous benefit. Furthermore, in Figure 4.4 we also observe that at higher radii, the ULDM model exhibits a characteristic dip in the radial velocity profile. The observational data does not extend far enough into the high radius regime to reveal whether such features exist in astrophysical structures. Indeed, the data in this case tapers off at galactocentric radii exceeding around 10kpc. From the limited number of galaxies for which data approaches this regime (in

particular UGC03580, UGC01230, NGC3769, NGC1003), there does not seem to be a tendency toward a dip. The error bars are relatively constrained in this high radius region, as shown in Figure 4.6, so the absence of a dip arguably weakens support for the ULDM model. More data at higher radii is required to make a strong determination on this point.

Meanwhile, in Figure 4.7, the spread of data at high radius is within the scale of the error bars, but at smaller radii the data is not encompassed by random measurement error alone. This spread of data may suggest that grouping galaxies based on asymptotic velocities alone is an insufficient method of characterisation. However, there is very limited data in this sample at small radii, so both larger data sets and comprehensive modelling of baryonic effects in high density inner regions are required to resolve this issue.

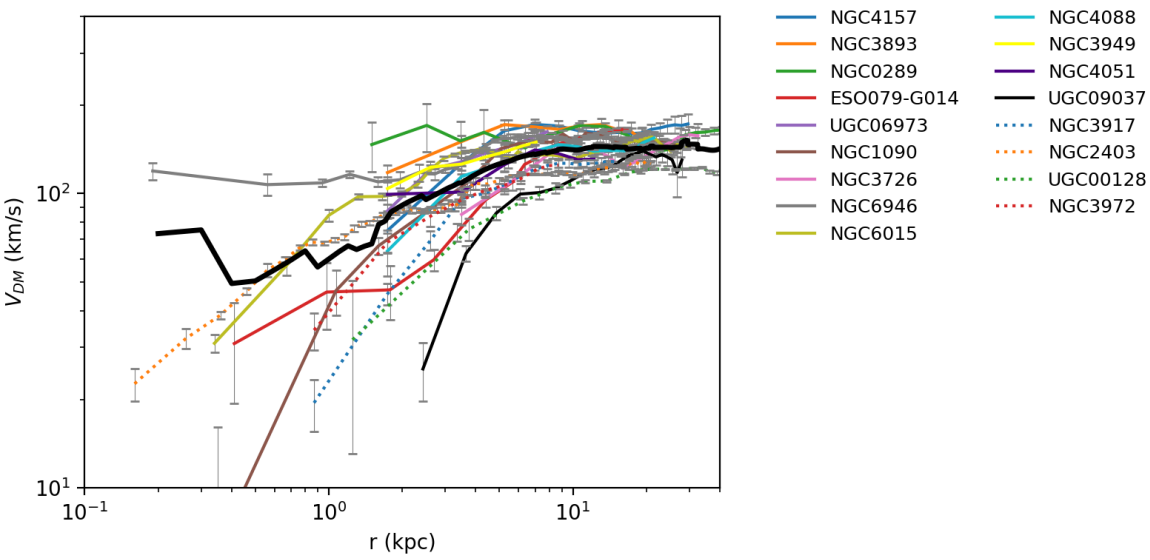

Figure 4.7: Radial distributions for galaxies with maximum velocities in the range $125 \leq v < 175\,\mathrm{kms}^{-1}$ in the SPARC database. The average profile is shown in the bold black line. The limited number of galaxies with high asymptotic velocities makes it difficult to judge typical galaxy characteristics in this regime. Furthermore, we see that data at small radii is lacking, and for that which is available, the variation in velocity profiles cannot be accounted for by random error in the measured velocities alone.

Chapter 5

Collapse of Aspherical Overdensities in the ULDM Model: Evidence for Variability in the Core-Halo Mass Relation

This chapter is an adaptation of

Emily Kendall, Richard Easther
Collapse of Aspherical Overdensities in the ULDM Model: Evidence for Variability in the Core-Halo Mass Relation
(Manuscript in preparation)

5.1 Introduction

In this chapter I investigate the collapse of aspherical ULDM overdensities in an expanding background. I study the properties of the ULDM halos formed by this collapse process, investigating whether traces of asphericity present in the initial overdensity are imprinted in the collapsed objects. I also investigate the process of 'soliton oscillation', which has been previously observed in Refs. [229, 230, 231] and shown to persist well after collapse has taken place.

Of particular interest is the effect these phenomena may have on variability in the core-halo mass relation [232, 233, 132]. Indeed, should asphericity be present within the central region of collapsed ULDM objects, this region cannot accurately be modelled by the soliton solution to the Schrödinger-Poisson equations. Accordingly, variability around the theoretical core-halo mass relation (in which the core is modelled as a soliton) is expected. Moreover, given the oscillations of this (approximately) solitonic core, the core-halo mass relation must indeed vary over time. It is the purpose of this work to estimate the extent of this variability.

In order to perform this analysis, I first initialise a spherically-symmetric, isolated Gaussian overdensity within the AxioNyx AMR simulation tool [114]. This overdensity is allowed to collapse from redshift $z = 99$ to $z < 1$, assuming a matter-dominated universe in which the evolution of the scale factor, a, obeys $a \propto t^{2/3}$. I then gradually augment the initial conditions in order to 'flatten' the initial overdensity along one axis, and gauge the effect this flattening has on the collapse process and final ULDM halo parameters.

The remainder of this chapter is organised as follows. I first give a brief introduction to the AxioNyx simulation suite in Section 5.2, and discuss simulation setup parameters in Section 5.3. I then present the results in 5.4 and analyse the effect of asphericity and soliton oscillations on the core-halo mass relation. I conclude in 5.5.

5.2 AxioNyx: AMR Solver for ULDM Dynamics

While fixed-grid pseudospectral solvers such as PyUltraLight are useful for simulating ULDM physics on a static background, they suffer from decreasing spatial resolution in an expanding background. In the context of ULDM, it is important that resolution is maintained at the scale of the de Broglie wavelength in order to properly model macroscopic quantum phenomena. This becomes increasingly difficult with a fixed-grid solver when processes such as overdensity collapse over a large range of redshifts are simulated, and is generally computationally prohibitive.

To overcome this, Adaptive Mesh Refinement (AMR) may be used. This technique allows for selected regions of the simulation grid to be computed at higher resolution than others. For example, regions of high density or velocity

may trigger refinement, while regions of low density are computed on a base-level coarse grid. This ensures computational efficiency while maintaining the necessary resolution in regions in which important physics is modelled. AxioNyx is an AMR solver designed for ULDM simulations. It is built on top of the Nyx cosmology AMR simulator [154], which is itself built upon the AMReX framework [234]. While AxioNyx inherits support for simulating CDM and baryonic matter from Nyx, it is the only the new ULDM functionality which I employ here. Specifically, AxioNyx utilises both pseudospectral and finite-differencing methods to solve the Schrödinger-Poisson system on the root grid, while using finite-differencing alone to solve the Schrödinger-Poisson system in refined regions where periodic boundary conditions no longer apply.

AxioNyx provides a simple C++ header file for specifying the spatial parameters of an initial a ULDM overdensity field. The comoving cosmological critical density and Hubble constant are also specified here, and by default the critical density sets the uniform background density field. In this work I also make use of a separately computed Gaussian random field, which is then called by the header file to initialise a background with random small perturbations around the critical density. A separate input file is used to specify parameters such as root grid resolution, comoving grid size, initial and final redshifts, FDM to CDM ratios, and refinement criteria. In this work I begin all simulations at $z = 99$ ($a = 0.01$) on a 512^3 base grid. The critical density is $\rho_{\rm crit}(a) = a^{-3} \times 1.36 \times 10^{11}$ $\mathrm{M}_\odot\mathrm{Mpc}^{-3}$ with $H_0 = 70\mathrm{kms}^{-1}\mathrm{Mpc}^{-1}$ and $m_{22} = 1$.

5.3 Flattened Ellipsoidal Overdensities

To begin, we take a spherical Gaussian overdensity, and gradually augment this through flattening along one axis. For a grid of coordinates (x, y, z), we define:

$$r = \sqrt{x^2 + y^2 + z^2}, \quad \text{and} \quad r_{\rm ell} = \sqrt{\left(\frac{x}{a}\right)^2 + \left(\frac{y}{b}\right)^2 + \left(\frac{z}{c}\right)^2}. \tag{5.1}$$

In this work, we take $a = b$ and define the flattening parameter f as:

$$f = \frac{a - c}{a}. \tag{5.2}$$

We explore different flattening scenarios by setting $0.0 \leq f \leq 0.5$, while keeping the product abc constant such that:

$$a = b = \left(\frac{1}{1-f}\right)^{1/3}, \quad \text{and} \quad c = a(1-f). \tag{5.3}$$

Finally, we introduce a characteristic radius $r_{\rm ch}$ to control the width of the flattened Gaussian. This is kept constant throughout the simulations at

$$r_{\rm ch} = \frac{a_{\rm init} \times 0.165L}{\sqrt{2}}, \tag{5.4}$$

where L is the comoving side length of the simulation box and the value of $r_{\rm ch}$ is chosen such that the overdensity is large enough to collapse but does not take up enough of the root simulation grid to be disrupted by the periodic boundary conditions. All simulations are initialised at $z = 99$, corresponding to $a_{\rm init} = 0.01$. The initial density field is then defined as:

$$\rho(x, y, z) = \rho_{\rm crit}\left(1 + \delta_1 \exp\left(-\frac{r_{\rm ell}^2}{r_{\rm ch}^2}\right)\right), \tag{5.5}$$

where $(1 + \delta_1)\rho_{\rm crit}$ is the initial maximum overdensity at the centre of the Gaussian. While this field initialisation is used for the first round of simulations, we also perform another series of simulations using an alternative initial field, namely

$$\rho_{\rm alt}(x, y, z) = \rho_{\rm crit}\left(1 + \delta_1 \exp\left(-\frac{r_{\rm ell}^2}{r_{\rm ch}^2}\right) + \delta_2 \mathcal{G}(x, y, z)\right), \tag{5.6}$$

where the final term in the sum, $\delta_2\mathcal{G}(x, y, z)$, represents a Gaussian random field which is introduced in order to break the symmetry in the simulation to a low degree. We choose $\delta_2 < \delta_1$, ensuring that the principal overdensity remains dominant. The same Gaussian random field is used for each simulation, and is read in at runtime from a separately generated array. The Gaussian random field used here is not intended to replicate the density field of the early universe, but to provide an explicit symmetry-breaking mechanism without the need to introduce particles.

We will refer to the simulations which utilise Equations 5.5 and 5.6 as the 'unperturbed case' and 'perturbed case', respectively. We will consider their results

separately in the next section.

5.4 Results

5.4.1 Unperturbed Case

We first consider the case where the background field is constant, as in Equation 5.5. We find that AxioNyx preserves symmetry to a high degree, such that the collapsed halos do not produce the typical incoherent outer regions seen in other simulations (see, for example, Figure 4.1). Indeed, the random fluctuations, which are characteristic of the incoherent outer regions of ULDM halos must be seeded by some explicit symmetry-breaking mechanism. This may be the introduction of CDM or baryonic matter particles, or, as we shall explore in the next section, the introduction of additional small random perturbations to the background. Notwithstanding the unphysically high preservation of symmetry of these simulations, they provide a useful test regime in which to explore the role that the initial overdensity shape plays in halo formation.

We simulate collapse for initial overdensities characterised by flattening parameters $f = 0.0$, 0.1, 0.2, 0.3, 0.4, and 0.5. We choose $\delta_1 = 0.1$ and $L = 1.0$Mpc. Density plots of the initial configurations are shown in Figure 5.1. Running these simulations from $a = 0.01$ to $a = 0.6$ ($99 \leq z \leq 0.67$), we first find that increasing the flattening parameter leads to a delayed collapse. This phenomenon is illustrated in Figure 5.2. We consider 'collapse' to have occured at the first peak in the overdensity curve. After this point, the central soliton-like core has formed, and begins to oscillate.

Figure 5.2 clearly illustrates that as flattening increases, the first peak in overdensity shifts to a higher scale factor (lower redshift). Figure 5.3 is also presented to more clearly illustrate the late-time oscillation phase for the two extreme cases, $f = 0.0$ and $f = 0.5$. Indeed, it is known that in triaxial collapse scenarios, collapse occurs most slowly along the longest axis, leading to phenomena such as the colloquial 'Zel'dovich pancake' [235, 236]. As we increase the flattening parameter in these simulations, the length of the longest axis increases, and it is therefore expected that the collapse process takes longer to complete.

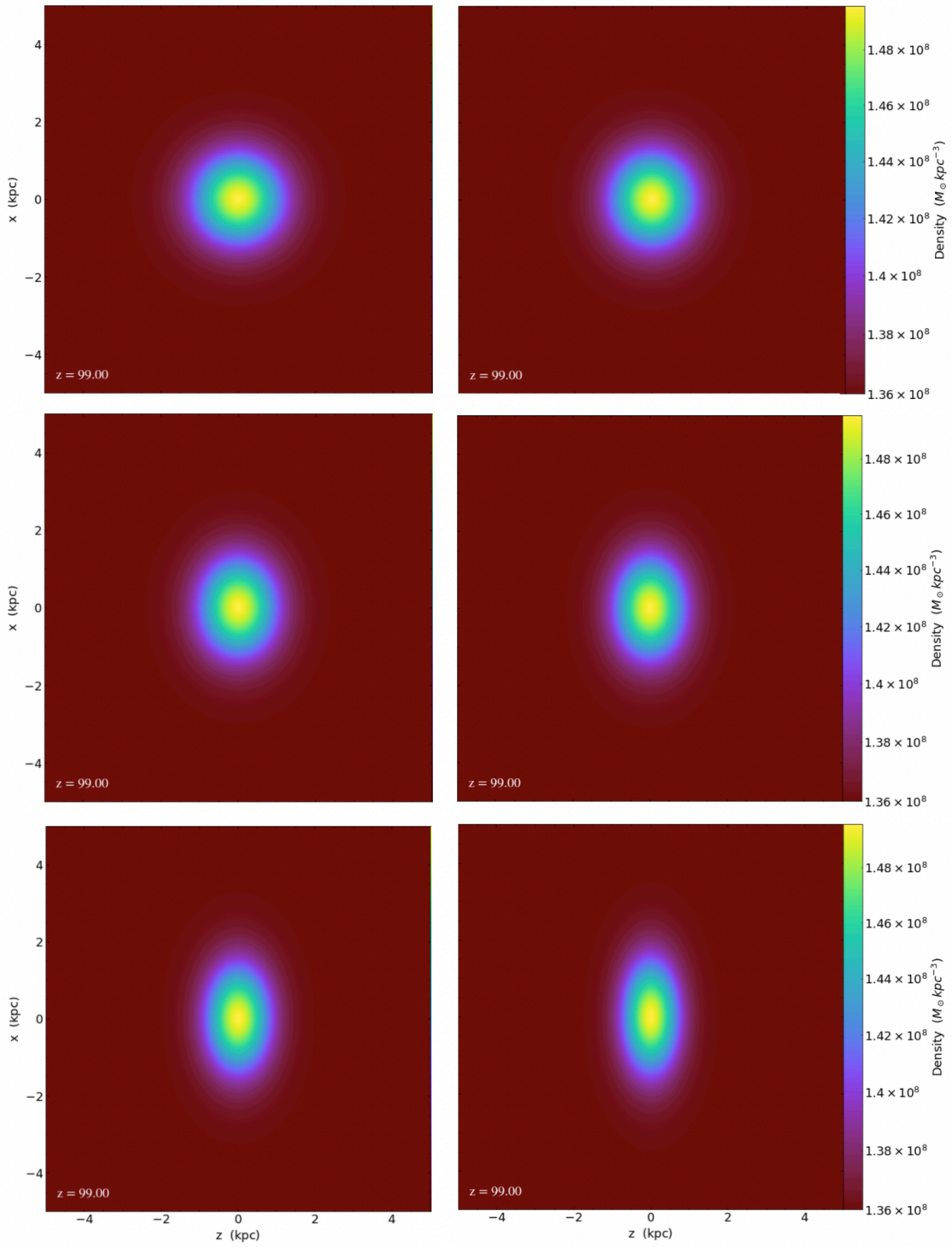

Figure 5.1: Illustrations of the initial field configurations in the unperturbed case. The $x - z$ plane is chosen such that the effect of increasing the flattening parameter is visible.

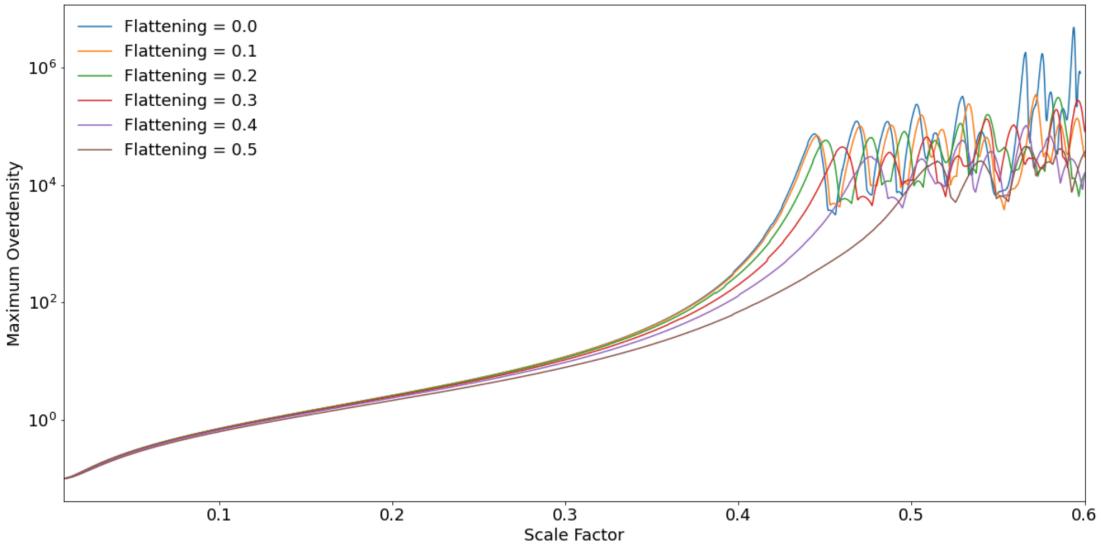

Figure 5.2: Plot of maximum overdensity as a function of the scale factor for initial overdensities with varying flattening parameter. Increasing the flattening parameter leads to a delayed collapse.

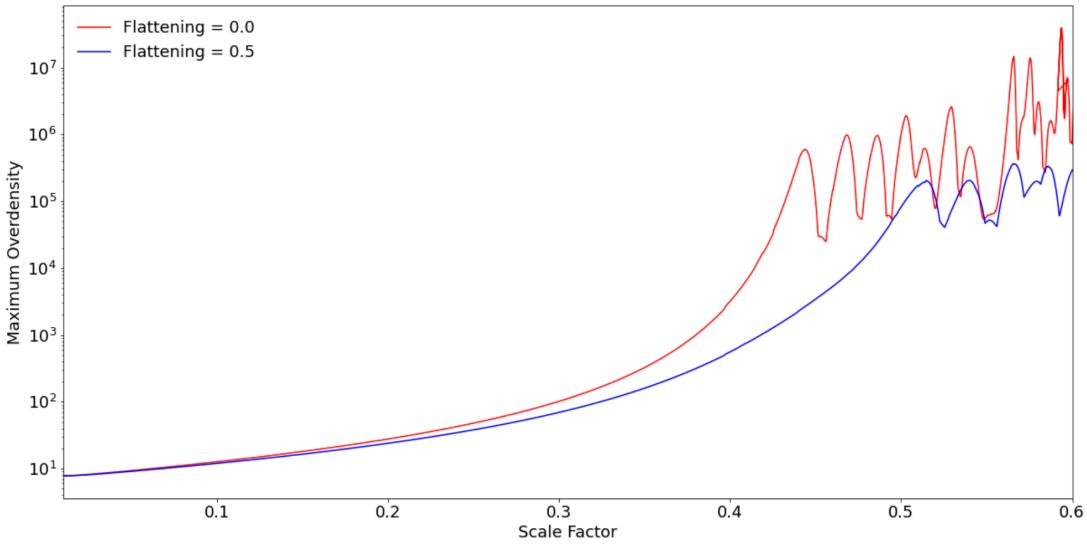

Figure 5.3: Plot of maximum overdensity as a function of the scale factor for initial overdensities with $f = 0.0$ and $f = 0.5$ only. The oscillation phase is clearly visible here.

It can also be observed in Figure 5.2 that the height of the overdensity peaks decrease with increasing flattening parameter. Given that the mass of each initial

overdensity is the same, this implies that the core regions of the collapsed halos have differing characteristics, and thus lends support to the idea of variation around the theoretical core-halo mass relation. We illustrate the systematic decrease in peak height as f increases in Figure 5.4, where we use the third peak as a typical example. Caution should be taken when analysing this figure, as each peak occurs at a different redshift. However, this figure serves as a helpful illustration of the overall phenomenon. The precise mechanism which leads to decreased peak height with increased flattening is unclear at this stage. However, it is anticipated that this may be elucidated through an eigenstate decomposition, such as that outlined in Ref. [237].

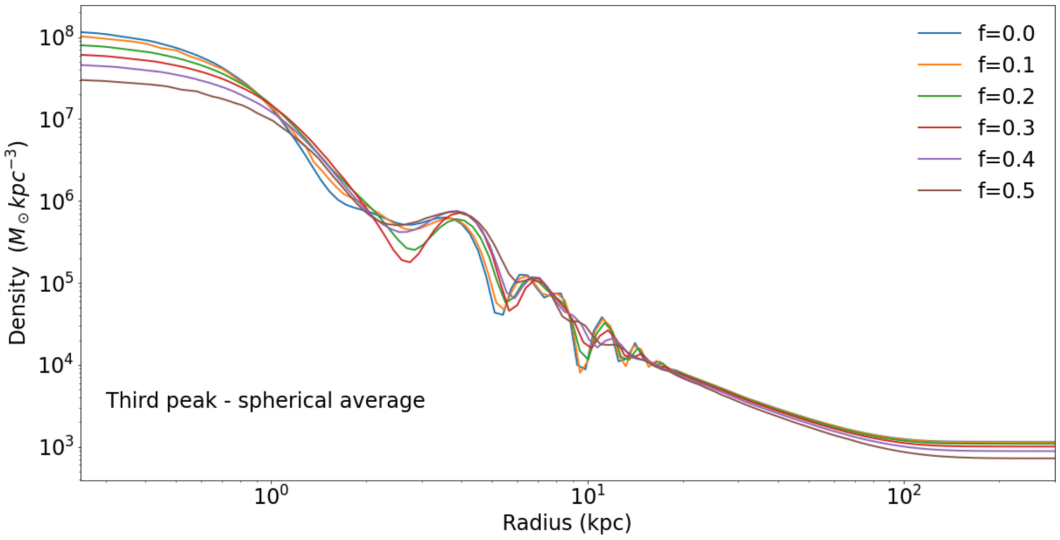

Figure 5.4: Comparison of density profiles at the third overdensity peak for increasing flattening parameter in the unperturbed case. For higher flattening values, a lower central density is achieved. Similar plots are obtained for other peaks.

Returning to Figure 5.2, we consider now the oscillation phase which begins after the first peak in the overdensity curve. This occurs due to the excess kinetic energy of infalling matter exciting ULDM field modes above the ground state. As a consequence, the inner region of the halo is not described by the time-independent soliton solution, as is often assumed in constructing theoretical piece-wise ULDM halo profiles [133].

Instead, the inner halo oscillates between a soliton-like profile and a more distorted superposition of excited states. To see how the morphology of the inner density profile changes, we consider the time interval between the first two peaks in the $f = 0.0$ overdensity curve. We illustrate the spherically-averaged density profile at the first and second peaks as red dotted curves in Figure 5.6. Meanwhile, density profiles from the inter-peak interval are shown in black. Though the inner halo appears roughly solitonic at overdensity peaks, the morphology varies markedly during the inter-peak interval.

Note that the profile at $a = 0.468$ in Figure 5.6 has a dramatic dip in density outside of the solitonic core. This is a consequence of the highly symmetric configuration, which results in a profile with concentric overdensity rings after collapse occurs. This is a manifestation of the gravitational cooling mechanism through which the collapsed object gradually emits excess energy. This configuration is illustrated in Figure 5.5. In Section 5.4.2, we will consider how explicit symmetry breaking affects this phenomenon.

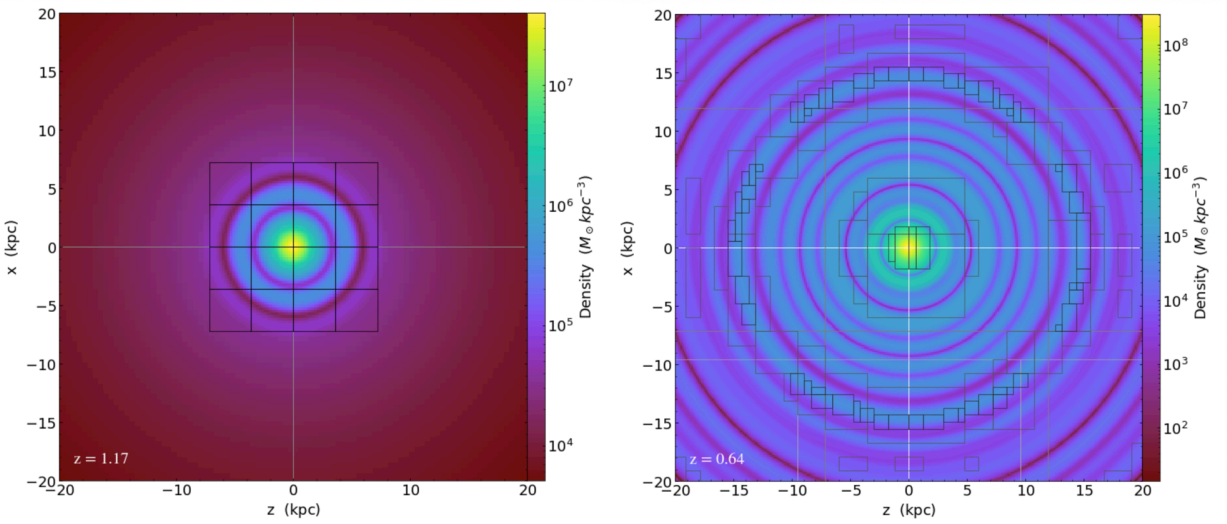

Figure 5.5: Illustration of concentric overdensity rings propagating outward after collapse occurs for the $f = 0$ unperturbed case. Refinement grids are also shown. Shortly after collapse (left) the rings have yet to spread through the whole simulation region. At late times (right) we see that the spread has increased. Through this gravitational cooling mechanism the collapsed halo is able to radiate excess energy.

The dramatic variability in the morphology of the inner halo during the extended

post-collapse oscillation phase is of great significance here. This variability suggests that the piece-wise 'solitonic core + NFW outer halo' construction for ULDM halos [133] is not universally valid. Moreover, this diminishes the applicability of the theoretical core-halo mass relation [132, 238], which implicitly assumes a piece-wise 'solitonic core + NFW outer halo' profile.

These results are supported by a number of other recent studies. In Ref. [239], it is found that the perturbation of a ULDM halo core by excited field modes can lead to a significant variability in the mass contained within the inner halo. Oscillating solitonic cores are also found in Ref. [240]. Our results suggest that further study of the variable morphology of the radial density profile during the oscillation phase is required, as this is likely to have direct observable consequences. Ultimately, this oscillatory behaviour suggests that the ULDM model may be compatible with a wide diversity of observed dark matter halos, which CDM may struggle to accommodate [241].

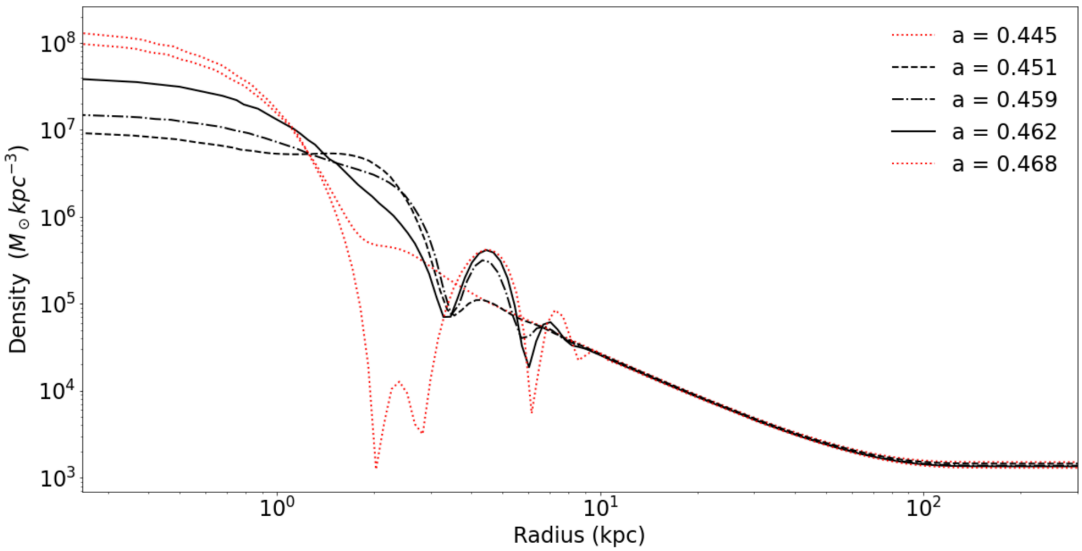

Figure 5.6: Variation in the spherically-averaged halo density profile between the first two peaks of the overdensity curve for the $f = 0.0$ collapse scenario.

While Figure 5.6 illustrates that even for a spherically symmetric case there exists significant deviation from a solitonic inner profile, we expect even greater discrepancy when the initial overdensity is not spherically symmetric. This is

because we anticipate that remnants of ellipticity (or in this case, flattening) will be present in the collapsed object, at least at early stages post-collapse. To see this, we consider the profile at successive peaks in the overdensity curve for one of the $f \neq 0$ cases. We choose the overdensity peaks because, as illustrated in Figure 5.6, it is here that inner profile most closely resembles that of a soliton.

In Figure 5.7, we illustrate the density profiles in the x and z directions for the first three overdensity peaks in the $f = 0.2$ case. We have chosen $f = 0.2$ for the sake of example, but note that similar results are obtained for other values of the flattening parameter. Importantly, though $f = 0.2$ is not a particularly extreme flattening parameter, we are still able to observe remnants of this flattening in Figure 5.7. In particular, we see that the profiles in the z direction are consistently narrower than those in the x direction, corresponding to the flattening direction in the initial overdensity. Moreover, there is no indication that this asphericity decreases quickly with time as it is still clearly observable at the third peak.

The fact that asphericity in the initial overdensity profile may be imprinted within collapsed objects is of great significance. Indeed, it is known that overdensities in Gaussian random field initial conditions (as in the early universe) are inherently triaxial [242]. Hence, our results suggest that asphericicity may be found in the central regions of ULDM halos, even in the late universe. Our simulations here act as proof of principle for this phenomenon, but we leave further investigation to more comprehensive simulations with cosmological initial conditions.

The simulations in the unperturbed case illustrate that variations in the shape of the initial overdensities can lead to dramatic changes in their evolution and collapse processes. Of particular importance is the fact that remnants of initial ellipticity remain after collapse has occured, and may therefore lead to variation around the theoretical core-halo relation. Moreover, irrespective of the precise shape of the initial overdensity, we have seen that the post-collapse oscillation phase causes variation in the morphology of the inner halos. This leads to further deviation from the theoretical core-halo relation, which assumes a solitonic inner density profile.

In order to assess the degree to which the core-halo relationship may vary, we will now perform simulations in the perturbed case. Because the symmetry is explicitly broken in this case, we anticipate that the results will be closer to realistic

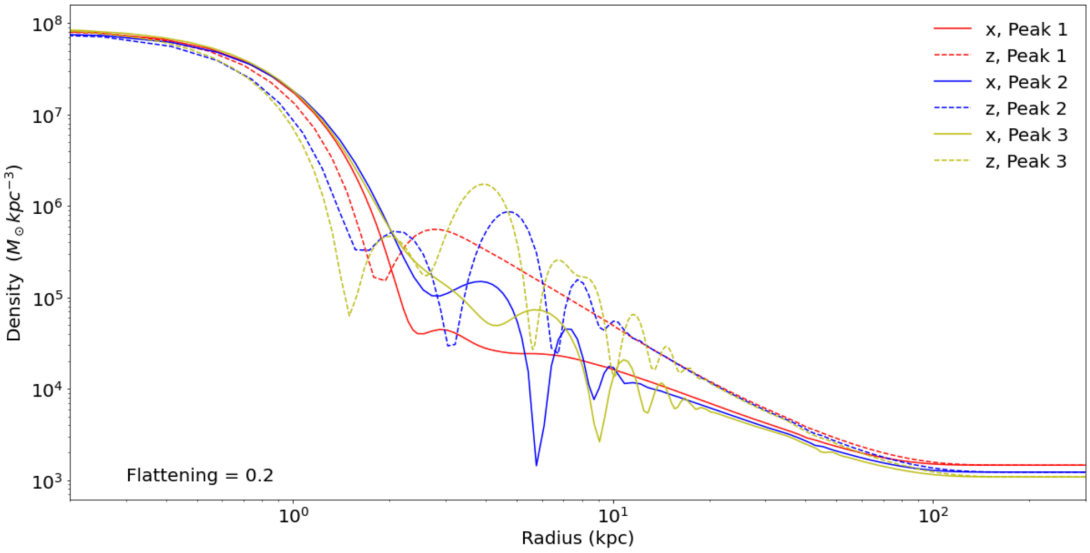

Figure 5.7: Density profiles in the x and z directions at the first three overdensity peaks for $f = 0.2$. In each case, we see that the inner profile in the z direction is systematically narrower than in the x direction.

astrophysical halos, which possess incoherent granular structure in the outer halo.

5.4.2 Perturbed Case

In this section, we perform simulations of overdensity collapse in the presence of a small-amplitude Gaussian random field, in accordance with Equation 5.6. We note that a Gaussian random background is more physically realistic than the perfectly smooth background of the previous section, though our overall setup still involves an artificially large central overdensity to ensure collapse. The perturbation of the background also serves to break the symmetry to a small degree, enabling more complex interference effects to give rise to incoherent substructure in the outer regions of collapsed halos. For these simulations, we choose comoving box side length $L = 2.0$ Mpc and $\delta_1 = 0.15$. These parameters result in halos with virial mass of order $10^9 M_\odot$. Meanwhile, δ_2 is chosen such that the maximum amplitude of fluctuations in the Gaussian random field is approximately 10% of that of the primary overdensity.

The initial configuration for the $f = 0$ case is shown in the left of Figure 5.8. We

see that the introduction of the Gaussian random background does not significantly impact the shape of the primary overdensity. However, it does serve to break the symmetry to a small degree. On the right of Figure 5.8 we see a typical density field at late times. In this case, we see that the concentric rings around the central overdensity have been slightly perturbed, but overall remain quite stable under this small perturbation. Moreover, we see that the solitonic peak is off-centre. This is indeed to be expected, as stochastic motion of the core has been observed in other ULDM simulations, and is a consequence of the interference of excited field modes [243].

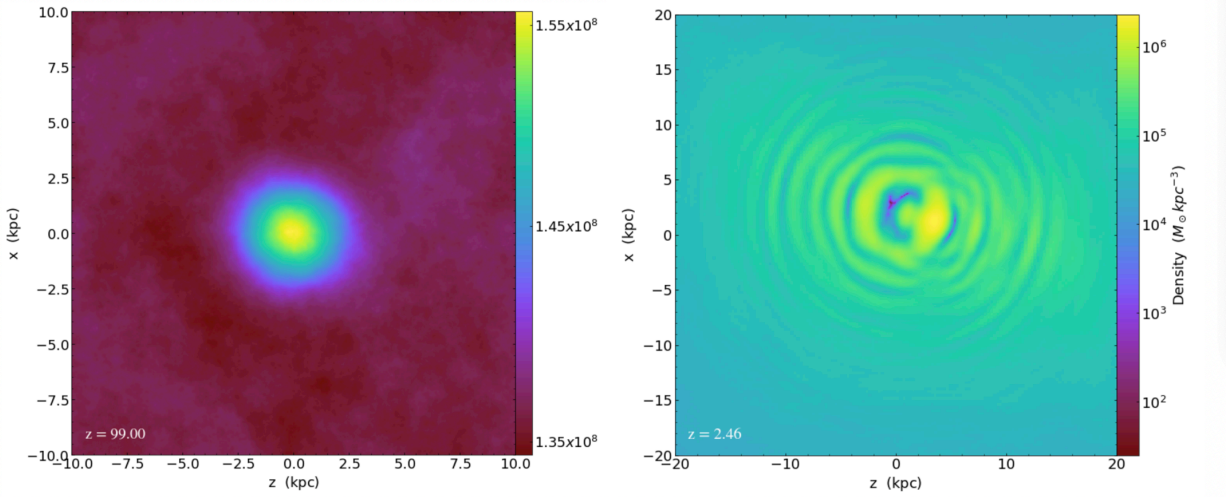

Figure 5.8: Left: initial field configuration for the perturbed case with $f = 0$. Right: late time density distribution, showing off-centre core and asphericity in the outer profile.

While we do not observe the typical granular outer halo structure in Figure 5.8, it is important to note that in a full cosmological structure formation simulation, the propagating rings around neighbouring collapsing overdensities would interfere. This would lead to the formation of the granular outer halos typical of ULDM. This phenomenon is not captured in these simulations of isolated collapse, yet our small perturbation does yield a small degree of asphericity.

As discussed in the previous section, the core region is not expected to remain solitonic throughout the oscillatory phase, and indeed we have shown that significant

changes in the morphology of the inner halo may occur. Nevertheless, the density profiles at the overdensity peaks provide a useful test case, as these profiles here appear to be roughly solitonic.

We identify our choices of three clear overdensity peaks for each value of f in Figure 5.9. In these plots, it can be observed that when f is large, there is clear evidence of triaxial collapse in the changes in slope of the overdensity curve.[1]

For each chosen output, we calculate the virial mass and radius of each collapsed halo according to the average internal density criterion $\bar{\rho} = 200\rho_{\text{crit}}$. From this virial mass, we compute the predicted core radius using Equation 2.70. We then compare this to the observed value of the core radius, and compute the deviation as:

$$\delta_{r_c} = \frac{r_{c\ (\text{true})} - r_{c\ (\text{predicted})}}{r_{c\ (\text{true})}} \times 100\%. \tag{5.7}$$

We also use Equation 2.67 to construct a solitonic fit to the observed inner profile. We illustrate a representative example of this process for the first peak in the $f = 0$ case in Figure 5.10, while similar plots for the remaining peaks are given in Appendix C. In all cases, we see that while the halo profile appears to possess the characteristic solitonic core surrounded by an NFW type halo, the core region is actually slightly narrower than the theoretical soliton, indicating a slightly 'compressed' configuration. We also observe varying degrees of granularity in the outer halo. We note that because these simulations involve the collapse of isolated halos, the granularity in the outer region is not fully captured. This is due to the lack of interference effects of matter propagating outward from neighbouring collapsing overdensities. In each figure we also observe a density plateau at large radial distances. This plateau occurs when the density approaches the critical density, confirming that the simulation box is sufficiently large to encompass the whole halo.

We summarise our results in Table 5.1. While this small sample is insufficient for a full statistical analysis of variability in the core-halo mass relation, it serves as a useful illustration of the relevant phenomena at play. We find that the theoretical core-halo relation systematically predicts a larger value of r_c than is observed.

[1]Note that the circles identifying the choice of density profiles may in some cases be shifted slightly from the maxima of the curve, as full field outputs are not saved at every individual timestep.

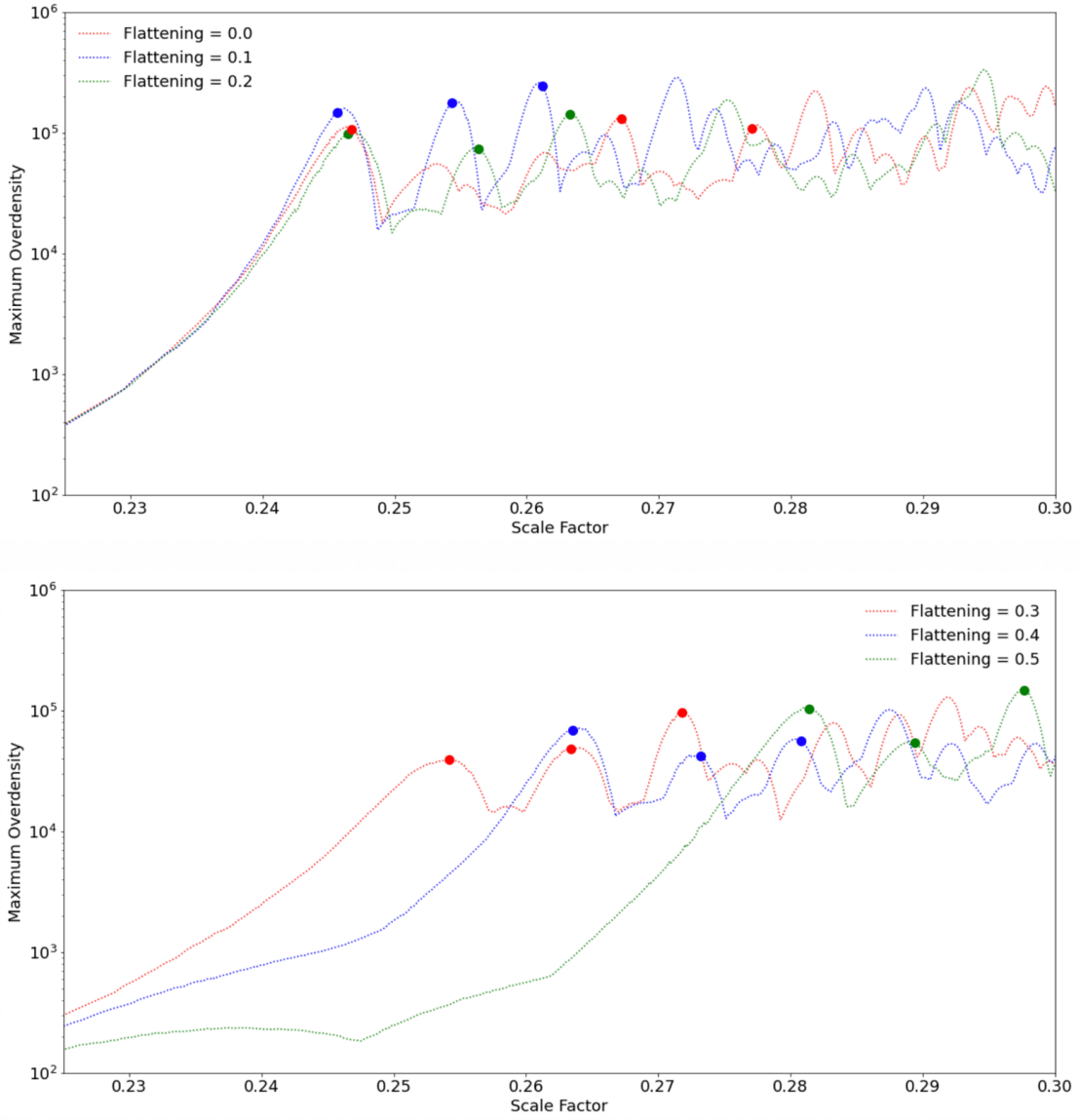

Figure 5.9: Curves of maximum overdensity at late times in the perturbed case. Choices of peaks are illustrated as circles on each curve. For $f = 0.4$ and $f = 0.5$, evidence of triaxial collapse is observed as changes to the slope of the overdensity curve.

Indeed, δ_{r_c} often exceeds 100%. This means that the solitonic cores predicted by the theoretical relation are systematically wider, with lower central densities than our simulated results. This is unsurprising, as we have selected outputs at the peaks of the overdensity oscillation phase. As previously discussed, the morphology

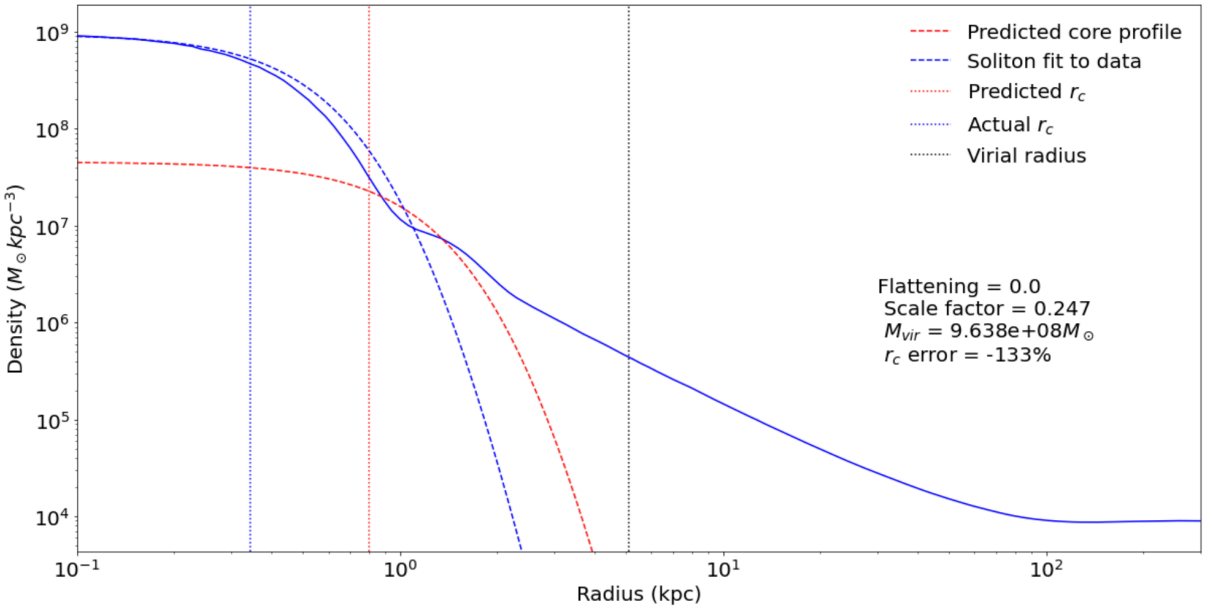

Figure 5.10: Spherically averaged density profile at the first overdensity peak in the perturbed $f = 0$ case. A soliton fit to the central profile is provided (blue), as is a soliton profile corresponding to the predicted core radius (red).

of the central halo varies widely during this phase, and it is natural to expect a narrower profile than that of the soliton at the maxima, transitioning to a wider profile as the overdensity curve begins to decrease.

	Peak 1	Peak 2	Peak 3
$f = 0.0$	-133%	-87%	-68%
$f = 0.1$	-136%	-131%	-140%
$f = 0.2$	-121%	-79%	-90%
$f = 0.3$	-63%	-62%	-76%
$f = 0.4$	-87%	-56%	-53%
$f = 0.5$	-89%	-90%	-63%

Table 5.1: Percentage deviation between predicted and actual core radii (δ_{r_c}) at the first three peaks in overdensity for each value of f. Negative values indicate cores which are narrower, with higher central densities than the theoretical prediction. Corresponding Figures are presented in Appendix C.

While we have analysed the core-halo variability only at peaks in the overdensity

curve, we expect further variation throughout the oscillation phase. In particular, we expect that at the minima of the oscillation phase, the predicted core radius would be smaller than the actual value. However, it is difficult to properly quantify this effect when the morphology of the core does not closely resemble a soliton.

One additional observation from Table 5.1 is that the theoretical core-halo relation appears to perform worst for the most spherical halos ($f = 0.1$ and $f = 0.1$). We note that these are also the instances in which the maximum halo overdensity is the highest. Further analysis is required to determine whether this is an indication that the core-halo relation varies as a function of halo mass.

5.5 Discussion

We have investigated the origins of deviation in the theoretical ULDM core-halo mass relation in isolated collapse scenarios. We make use of the AxioNyx code to perform these collapse simulations, enabling grid refinement around small core structures.

We have shown that even in the case of a spherically symmetric initial overdensity, the post-collapse oscillation phase naturally leads to deviations between the predicted and actual core profiles. This is because the oscillation phase involves complicated interference of excited eigenstates of the Schrödinger-Poisson system. The morphology of the core varies widely during this phase, and cannot reliably be modelled with a solitonic profile. We note that these results are supported by other studies, which have found similar core-halo variation, such as Ref. [227]. Our results motivate further investigation of post-collapse cores using an eigenstate decomposition method.

We have also shown that asphericity in the initial overdensity may be imprinted in the collapsed halo, further increasing tension between the theoretical ULDM halo piece-wise construction, which assumes a spherically symmetric solitonic core.

Though we have not performed a full statistical analysis of variation in the core-halo relation, which would require cosmological initial conditions, we have shown that the collapse of isolated overdensities can easily result in halos wherein the actual core radius differs from the predicted value by over 100%. Given this variability, we conclude that the dynamics of collapsed ULDM halos are such that a

wide variety of halo characteristics are naturally accommodated. This may be useful in reconciling theoretical models with the large variability found in astrophysical observations. By contrast, this is difficult to achieve in CDM models, which do not involve macroscopic quantum interference.

Chapter 6

Ongoing Investigations

6.1 Statistical Signatures of Anisotropies in the ULDM Density Distribution

One unique characteristic of the ULDM model is the presence of extended wavefronts, which arise during events such as overdensity collapse or halo collisions. Such wavefronts are a manifestation of the macroscopic quantum behaviour of ULDM, and do not have an analogue within CDM. Indeed, recent high-resolution cosmological simulations suggest the presence of additional structure in the filaments of the cosmic web in the ULDM model as compared to CDM. This is again due to quantum interference effects [244].

Such extended anisotropies cannot be completely characterised using the 2-point correlator, which is typically employed to analyse the statistics of the distribution of matter in the universe [245, 246, 247]. Instead, in order to comprehensively characterise these unique structures, we require a statistical tool which preserves information about anisotropy [248]. A natural candidate here is the traceless tidal tensor (TTT).

The traceless tidal tensor at each point in a density field gives the deformation of the corresponding volume element relative to purely spherical expansion or collapse. It is therefore an ideal tool to characterise fields in which structures possessing directional dependence arise. Following [249], to see how this is calculated for a density field $\rho(\mathbf{x})$, we first construct the dimensionless overdensity field $\delta(\mathbf{x})$:

$$\delta(\mathbf{x}) = \frac{\rho(\mathbf{x}) - \bar{\rho}}{\bar{\rho}}, \tag{6.1}$$

We then take the Fourier transform to obtain the dimensionless density contrast in Fourier space, $\delta(\mathbf{k})$. From here we can calculate the peculiar gravitational field from the Poisson equation, and finally compute the tidal tensor as the Hessian of the peculiar gravitational potential. In Fourier space we have:

$$\phi(\mathbf{k}) = k^{-2}\delta(\mathbf{k}), \qquad T_{ij}(\mathbf{k}) = k_i k_j \phi(\mathbf{k}). \tag{6.2}$$

At each point, the dimensionless density contrast is given by the trace of the tidal tensor. Therefore, in order to isolate tidal effects, we compute the Fourier space TTT:

$$\tilde{T}_{ij}(\mathbf{k}) = T_{ij}(\mathbf{k}) - \frac{\delta(\mathbf{k})}{3}\mathbb{I}_{ij}. \tag{6.3}$$

Finally, we perform an inverse Fourier transform to obtain the TTT in real space.

In order to make use of the TTT for statistical analysis of simulation output data, we randomly select a sample of several thousand grid points at which we compute the TTT and diagonalise it to find the eigenvalues, λ_1, λ_2, λ_3, and unit eigenvectors $\mathbf{e}_1$, $\mathbf{e}_2$, $\mathbf{e}_3$. We label the eigenvalues such that $\lambda_1 > \lambda_2 > \lambda_3$. Because these are the eigenvalues of the *traceless* tensor, we also have $\lambda_1 > 0$ and $\lambda_3 < 0$, while λ_2 may be either positive or negative.

Having obtained the eigenvalues of the TTT at each of our sample grid points, we may examine their probability distributions, and use this to differentiate between fields with differing anisotropic features.

In general, we expect the presence of repeated anisotropic structures such as wavefronts to induce peaks in the probability distributions of the eigenvalues, as in such cases there will be a number of volume elements exhibiting the same characteristic anisotropic deformation. To illustrate this, we consider two artificial distributions. The first distribution is simply a Gaussian random field, while the second is a 2-dimensional plane wavefront, generated by $\rho(x, y, z) = \sin^2(x)$. Figure 6.1 shows the eigenvalue distributions for the two cases. For the Gaussian random field, in which the statistical fluctuations are isotropic, the eigenvalues themselves

are characterised by Gaussian distributions. Meanwhile, the 2-dimensional plane wavefront yields eigenvalue distributions with distinct, prominent peaks. The exact position and height of the peaks will, in general, depend on the precise parameters of the waveform.

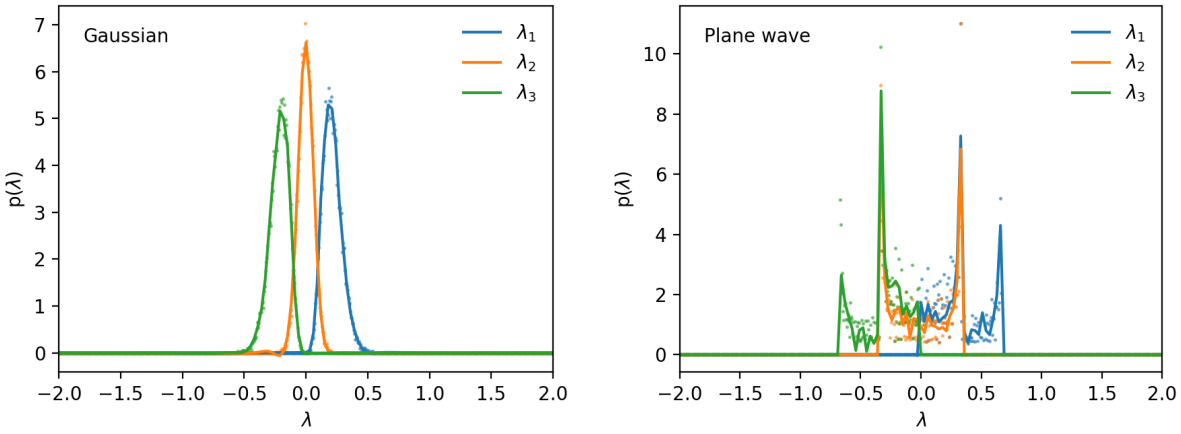

Figure 6.1: Probability distributions of the eigenvalues of the traceless tidal tensor for sample density distributions. Left: Gaussian random field, Right: $\rho(x, y, z) = \sin^2(x)$.

As a preliminary study, we examine the distribution of eigenvalues of the TTT for density distributions arising from collapsing ellipsoidal overdensities in PyUltraLight. We run the same simulation twice, changing only the value of the ULDM particle mass by one order of magnitude between the two simulations. As this is simply a proof-of-principle demonstration, we work in dimensionless code units and do not ascribe physical parameters to these simulations.

Near the onset of collapse, we obtain density distributions with differing properties depending on the ULDM particle mass. We illustrate a characteristic example of the (log) density fields obtained near the onset of collapse in the two cases in Figure 6.2. In the left of this figure, we see that broad wavefronts are present in the small ULDM mass case. This is to be expected as this case corresponds to the larger de Broglie wavelength. By contrast, the wavefronts illustrated on the right of the figure have a smaller wavelength, corresponding to the larger ULDM mass case.

From each of the density distributions illustrated in Figure 6.2, we draw a

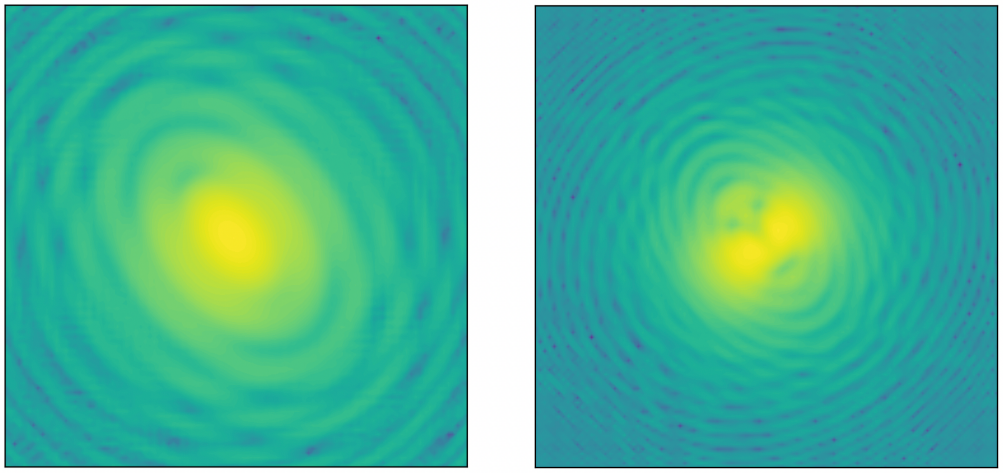

Figure 6.2: Snapshots of the log-scaled density field near the onset of collapse for the small ULDM mass case (left), and the case where this mass is increased by an order of magnitude (right).

sample of 15,000 randomly chosen grid points at which to compute the TTT of the (log-scaled) density field. We then compute the eigenvalues at each point. We divide the obtained eigenvalue range $\{-0.5, 0.5\}$ into 1500 bins, tallying the number of points which fall into each bin. We represent the outcome of this procedure using the scattered points in Figure 6.3. Because of the finite number of samples, we then apply a smoothing method to obtain a continuous distribution. In this case, we overlay the binned points with a best-fit cubic spline interpolation. The degree of smoothing will of course affect the visible level of substructure, however we note that the smoothing procedure applied here is sufficient to identify qualitative differences in the probability distributions of the two cases, which is sufficient for this proof-of-principle analysis.

Our results are presented in Figure 6.3, where the differences in the distributions for the smaller (left) and larger (right) ULDM mass cases are clearly visible. In particular, we see that the distribution of λ_2 has a higher peak around zero in the larger mass case, while the distributions of λ_1 and λ_3 possess small peaks at values away from zero which are not present in the smaller mass case. Instead, the distributions in the smaller mass case are indicative of a density field where the

anisotropies are smoothed on a larger scale, as expected.

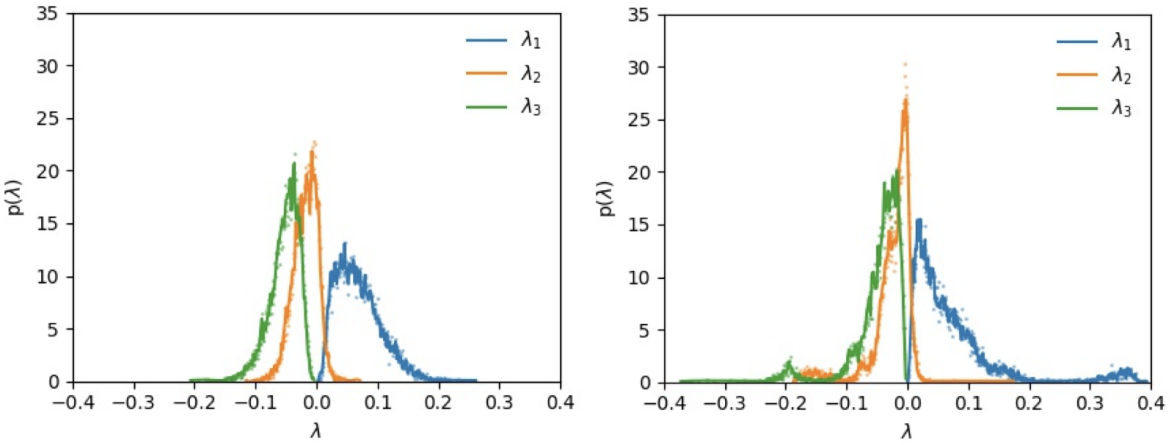

Figure 6.3: Probability distributions of the eigenvalues of the TTT for the smaller ULDM mass (left) and larger ULDM mass (right).

Clearly, much more work is required in order to apply these methods to physically realistic scenarios. However, the preliminary study presented here illustrates that the statistics of the TTT may serve as a useful quantitative tool for characterising the substructure of density distributions arising in ULDM models. Indeed, developing analysis techniques based on statistics beyond the two-point correlation function is anticipated to be of great utility in the context of current and upcoming weak lensing surveys [250]. Further investigation, including a detailed analysis of the anisotropic 2-point correlation functions of the eigenvalues of the TTT are planned for future work, using outputs generated using AxioNyx.

6.2 Effects of Angular Momentum on ULDM Halo Core Formation

As discussed in detail in Chapter 5, there is reason to believe that the 'typical' ULDM halo core may not be well-described by the ground-state soliton solution to the Schrödinger-Poisson equations. One factor which may have important

implications for halo core properties is angular momentum, which we have yet to explore in detail.

In Chapter 3, we briefly studied the internal velocity field of a soliton orbiting a central potential, and showed that it possessed the characteristics of the non-axisymmetric Riemann-S ellipsoid. However, this scenario only involved a tidally-locked soliton. More complex behaviours are expected when angular momentum is imparted to a halo through, for example, merger dynamics. It is necessary to understand the velocity distribution in the cores of such ULDM halos in order to characterise them as truly 'solitonic', rather than simply possessing profiles similar to that of the soliton under spherical averaging. In this section, we briefly outline a method for imparting angular momentum to collapsing ULDM overdensities. We intend to employ this method in future research using AxioNyx.

In order to initialise an ellipsoidal overdensity with zero net angular momentum, as was done in Chapter 5, we may simply set the phase of the ULDM field to zero throughout the simulation region. By contrast, in order to impart angular momentum to the ellipsoid, we also construct a second ellipsoid to control the phase of the ULDM field. This phase ellipsoid is concentric with the overdensity ellipsoid, and has a magnitude following an ellipsoidal Gaussian distribution with the same three axis parameters as the overdensity itself. Critically, however, we offset the orientations of the two ellipsoids by a non-zero angle.

We then assign a phase θ to each field point, with the magnitude of the phase determined by the amplitude θ, of the phase ellipsoid at that grid position. That is, $\psi \rightarrow \psi \times \exp(i\theta)$. Because the velocity of the ULDM field is given by $\mathbf{v} = \nabla\theta$, this process imparts rotational velocity to the original ellipsoidal overdensity. By varying the amplitude of the phase ellipsoid, we can change the magnitude of the angular momentum imparted to the overdensity.

We illustrate the outcome of this setup applied to PyUltraLight ellipsoidal overdensities at the onset of collapse in Figure 6.4 (again in dimensionless code units). From left to right we increase the angular momentum from zero, observing a corresponding distortion of the wavefronts in the density field (top), and an increasingly complicated internal velocity field (bottom).

In the zero angular momentum case, we see that at early times there is a competition between matter infalling under gravitational collapse and outgoing

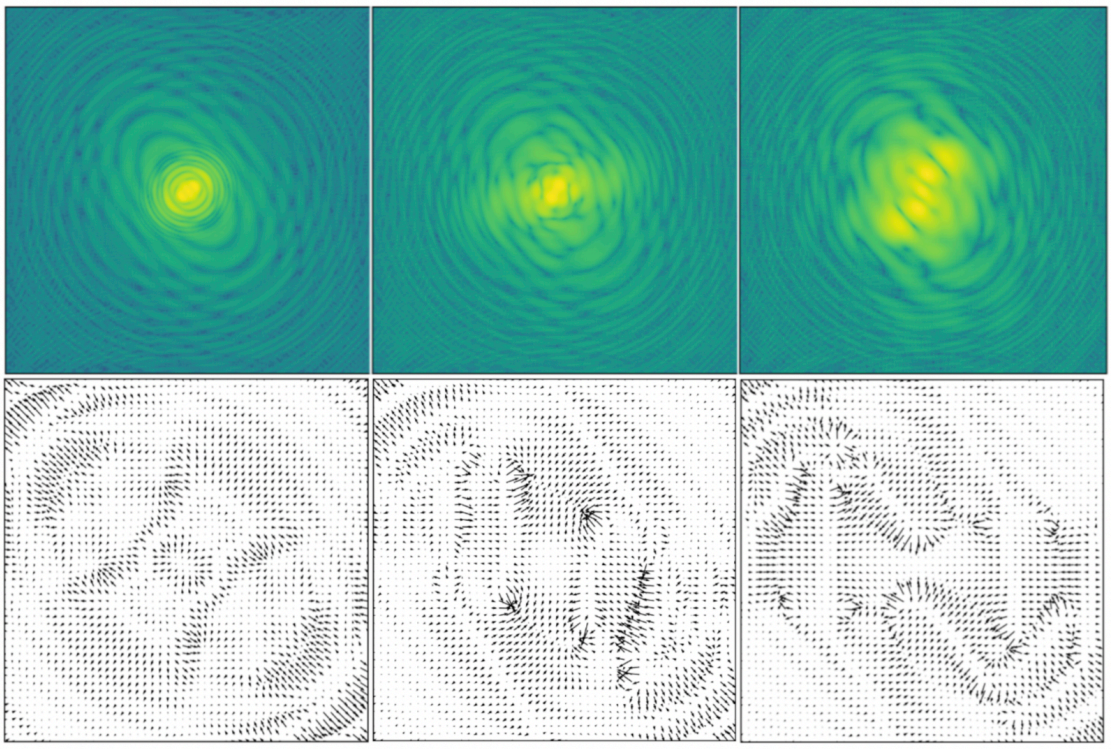

Figure 6.4: Top: density contours corresponding to an ellipsoidal overdensity initialised with increasing angular momentum (from zero on the left), on a 128^3 grid. Bottom: corresponding internal velocity fields of internal 50^3 grid region.

wavefronts due to quantum interference. This initial velocity distribution is clearly distorted due to rotation as angular momentum increases to the right. This, in turn, results in a proportion of the matter which would otherwise be propagating outward attaining a rotational velocity component, which is likely to affect core formation. Indeed, we expect that the late-time non-trivial velocity distributions in the core of the collapsed object. This ongoing activity is likely to have implications for the core-halo mass relation, particularly in regards to the criteria under which a halo may be considered to be 'relaxed'. Indeed, above a certain initial angular momentum threshold, we expect collapse to be prevented entirely.

A detailed study of the internal velocity fields of halo cores will be undertaken in future work using the AxioNyx simulation tool. Focus will be directed to the implications of angular momentum on the core-halo structure of ULDM, as well as

the identification of potentially observable astrophysical signatures.

Chapter 7

Conclusions and Discussion

In this thesis I have investigated the theory and computational modelling of ultra-light dark matter (ULDM). Macroscopic quantum effects in this model seem to present a natural solution to many aspects of the 'small-scale crisis' in the competing CDM model. In order to verify whether the ULDM model does indeed provide a more suitable dark matter candidate than CDM, I have highlighted the need for detailed numerical analysis of ULDM dynamics.

In Chapter 3, I introduced the simulation tool PyUltraLight, which has proved useful in investigating ULDM dynamics on galactic scales. Using PyUltraLight, we have been able to generate ULDM halos with the characteristic solitonic core + incoherent outer halo configuration. We have also been able to investigate merger scenarios in the ULDM model, and verify the outputs of the code by comparison to analytic models in simple test cases. PyUltraLight is available for public download, and has since been modified to treat a number of specific problems within ULDM phenomenology. I anticipate further adaptations of this code to be developed, with modifications tailored to specific problems in ULDM physics.

In Chapter 4, I investigated the implications of the theoretical core-halo mass relation of ULDM halos in the context of the core-cusp problem. I showed that whether the ULDM model is able to outperform CDM in reproducing observations of galaxies from the SPARC database is largely dependent on the degree of scatter around the theoretical core-halo relation. I concluded that further investigation

of typical ULDM halo characteristics and more extensive observational data are needed in order to settle this debate.

In Chapter 5, I studied the applicability of the theoretical core-halo mass relation to halos formed by collapse of ellipsoidal overdensities in AxioNyx. I found multiple lines of evidence for significant scatter about the theoretical prediction. In particular, I found that oscillations within the cores of collapsed ULDM objects can lead to dramatic variations in the morphology of the inner halo profile, which has direct implications for the applicability of the core-halo mass relation. I also found that asphericity in the initial overdensity may be imprinted in the halo cores post-collapse, further increasing tension with the traditional solitonic core + NFW outer halo assumption used to derive the theoretical core-halo mass relation.

Finally, in Chapter 6, I introduced a number of avenues for ongoing research. One such avenue involves the development of statistical tools beyond the two-point correlation function, which take into account the presence of anisotropies. It is anticipated that the statistics of the eigenvalue distributions of the traceless tidal tensor may prove useful in characterising wavelike anisotropies in the ULDM model. I also briefly introduced angular momentum in ULDM halos, which I anticipate will further affect the applicability of the theoretical core-halo mass relation. Detailed studies of angular momentum within ULDM halos are planned for future work.

There remains a broad range of phenomenology within the ULDM model which has yet to be investigated in detail. Scope for further research includes the introduction of baryonic physics such as stellar formation and feedback into ULDM-only models, as well as an exploration of mixtures of different dark matter components. As more advanced simulation tools continue to be developed, I anticipate a wide range of important investigations to be undertaken in the near future.

Appendix A

Scaling Properties of the Shrödinger-Poisson System

The coupled differential equations of the Schrödinger-Poisson system obey a particularly simple scale invariance [251, 129]. To see this, let us suppress factors of m, $\hbar$ and G for notational convenience (these factors can be restored later), and write the Schrödinger-Poisson system as:

$$i\dot{\psi} = -\frac{1}{2}\nabla^2\psi + \Phi\psi, \tag{A.1}$$

$$\nabla^2\Phi = 4\pi|\psi|^2, \tag{A.2}$$

where $\psi = \psi(\mathbf{x}, t)$ and $\Phi = \Phi(\mathbf{x}, t)$. If we consider only spherically symmetric solutions, the Schrödinger-Poisson system becomes:

$$i\dot{\psi} = -\frac{1}{2}\frac{d^2\psi}{dr^2} + \Phi\psi, \tag{A.3}$$

$$\frac{d^2\Phi}{dr^2} = 4\pi|\psi|^2, \tag{A.4}$$

where $\psi = \psi(r, t)$ and $\Phi = \Phi(r, t)$. Let us now suppose we have a spherically symmetric solution of the form $\psi(r, t) = e^{i\beta t}f(r)$. Substituting this solution into the Poisson equation (A.4) we obtain:

$$\frac{d^2\Phi(r)}{dr^2} = 4\pi|f(r)|^2, \tag{A.5}$$

which automatically gives

$$\frac{d^2\Phi(\sqrt{\alpha}r)}{d(\sqrt{\alpha}r)^2} = 4\pi|f(\sqrt{\alpha}r)|^2, \tag{A.6}$$

where α is some positive constant. Using the chain rule, this may also be expressed as

$$\frac{d^2\Phi(\sqrt{\alpha}r)}{dr^2} = 4\pi\alpha|f(\sqrt{\alpha}r)|^2. \tag{A.7}$$

Now imagine that we have another function of the form $g(r,t) = e^{i\alpha\beta t}\alpha f(\sqrt{\alpha r})$. For this function to also satisfy the Poisson equation (A.4), we require:

$$\frac{d^2\Phi(r)}{dr^2} = 4\pi|g(r)|^2 = 4\pi\alpha^2|f(\sqrt{a}r)|^2. \tag{A.8}$$

Comparing Equations A.7 and A.8, this condition translates to

$$\alpha\frac{d^2\Phi(\sqrt{\alpha}r)}{dr^2} = \frac{d^2\Phi(r)}{dr^2}. \tag{A.9}$$

Integrating twice with respect to r gives us a scaling condition on Φ for $g(r,t)$ to satisfy the Poisson equation:

$$\alpha\Phi(\sqrt{\alpha}r) = \Phi(r). \tag{A.10}$$

Let us now consider the Schrödinger equation. Substituting the known solution, $\psi(r,t) = e^{i\beta t}f(r)$ into the Schrödinger equation A.3, we obtain:

$$-\beta f(r) = -\frac{1}{2}\frac{d^2f(r)}{dr^2} + \Phi(r)f(r), \tag{A.11}$$

which automatically gives us

$$-\beta f(\sqrt{\alpha}r) = -\frac{1}{2}\frac{d^2f(\sqrt{\alpha}r)}{d(\sqrt{\alpha}r)^2} + \Phi(\sqrt{\alpha}r)f(\sqrt{\alpha}r). \tag{A.12}$$

In order that $g(r,t) = e^{i\alpha\beta t}\alpha f(\sqrt{\alpha}r)$ also satisfy Equation A.3 we require:

$$-\alpha^2\beta f(\sqrt{\alpha}r) = -\frac{\alpha}{2}\frac{d^2f(\sqrt{\alpha}r)}{dr^2} + \alpha\Phi(r)f(\sqrt{\alpha}r). \tag{A.13}$$

Dividing through by α^2 this gives:

$$-\beta f(\sqrt{\alpha}r) = -\frac{\alpha^{-1}}{2}\frac{d^2 f(\sqrt{\alpha}r)}{dr^2} + \alpha^{-1}\Phi(r) f(\sqrt{\alpha}r). \tag{A.14}$$

Comparing Equation A.14 with Equation A.12, we see that this is true if

$$\frac{d^2 f(\sqrt{\alpha}r)}{dr^2} = \alpha \frac{d^2 f(\sqrt{\alpha}r)}{d((\sqrt{\alpha}r))^2}, \tag{A.15}$$

and

$$\Phi(r) = \alpha\Phi(\sqrt{\alpha}r). \tag{A.16}$$

Equation A.15 is true by the chain rule, while Equation A.16 is the same requirement given in Equation A.10 for $g(r,t)$ to satisfy the Poisson equation.

Hence, a single spherically symmetric solution to the Schrödinger-Poisson system of the form $\psi(r,t) = e^{i\beta t} f(r)$ admits an entire family of solutions, characterised by the single scaling parameter α. The ground-state solutions are referred to as solitons. The α scaling of the solitons has important consequences for calculating mass, radius and density parameters for ULDM halos. One quantity of particular interest is the 'core radius', r_c, defined as the radius at which the density drops to one half its central value. Let us compare how this radius compares for Schrödinger-Poisson solutions parametrised by α.

The central density for a soliton with $\alpha = 1$ is given by $\rho_{c,1} = |f(0)|^2$, while for arbitrary α we have $\rho_{c,\alpha} = \alpha^2 |f(0)|^2$. The densities at r_c are therefore

$$\rho(r_c)_1 = \frac{|f(0)|^2}{2} = |f(r_{c,1})|^2, \tag{A.17}$$

and

$$\rho(r_c)_\alpha = \frac{\alpha^2|f(0)|^2}{2} = \alpha^2 |f(\sqrt{\alpha}r_{c,\alpha})|^2. \tag{A.18}$$

Combining these expressions, we find:

$$\rho(r_c)_\alpha = \frac{\alpha^2|f(0)|^2}{2} = \alpha^2|f(r_{c,1})|^2 = \alpha^2|f(\sqrt{\alpha}r_{c,\alpha})|^2 \tag{A.19}$$

which therefore implies a scaling relationship for the core radius:

$$r_{c,\alpha} = \frac{1}{\sqrt{\alpha}} r_{c,1}. \tag{A.20}$$

Note that this means that solitons with larger central densities have a smaller core radius. In other words, their density distributions are more 'peaked'. Having obtained the scaling relationship for the core radius, we can calculate the scaling also for the core mass, M_c, defined as the mass within r_c. We have:

$$M_{c,1} = 4\pi \int_0^{r_{c,1}} r^2 |f(r)|^2 dr \tag{A.21}$$

and

$$M_{c,\alpha} = 4\pi \int_0^{r_{c,\alpha}} r^2 \alpha^2 |f(\sqrt{\alpha} r)|^2 dr. \tag{A.22}$$

Letting $x = \sqrt{\alpha} r$ this integral becomes

$$M_{c,\alpha} = 4\pi \sqrt{\alpha} \int_0^{r_{c,1}} x^2 |f(x)|^2 dx = \sqrt{\alpha} M_{c,1}. \tag{A.23}$$

Overall, therefore, there exists a class of spherically symmetric ground state solutions paramaterised by α for which the central density, core mass, and core radius scale as $\rho_c \propto \alpha^2$, $M_c \propto \sqrt{\alpha}$ and $r_c \propto 1/\sqrt{\alpha}$, respectively [252]. Often, we will find it a convenient alternative to parametrise by M_c, in which case $r_c \propto 1/M_c$ and $\rho_c \propto M_c^4$.

Appendix B

Core-halo Mass Relation

The core-halo mass relation can be simply interpreted as the statement that the average internal velocity of a tracer mass in the core must be equal to the virial velocity of a tracer mass in the wider halo. If this were not the case, and instead the average velocity were higher within the core, these higher velocity particles would move outward, resulting in dynamical mass redistribution within the halo. During this process, the halo would not be in equilibrium and would thus not be virialised.

From the virial theorem we have that $E_K = -1/2\ E_P$, where E_K and E_P represent kinetic and potential energies, respectively. Alternatively we can write:

$$\frac{1}{2}M_{tot}v^2 = \frac{1}{4}\frac{GM_{tot}^2}{R_{tot}}, \tag{B.1}$$

where G is the gravitational constant, M_{tot} and R_{tot} are the total mass and radius, and v^2 is the mean of the squares of individual tracer velocities. Demanding that v^2 is the same for the core as for the total virialised halo allows us to then write:

$$\begin{aligned} v^2 &= \frac{G\mathrm{M_{vir}}}{2R_{\mathrm{vir}}} = \frac{GM_{core}}{2R_{core}} \\ \rightarrow R_{core} &= \frac{M_{core}R_{\mathrm{vir}}}{\mathrm{M_{vir}}}. \end{aligned} \tag{B.2}$$

We know from the soliton scaling properties that $R_{core} \propto M_{core}^{-1}$, and since $\mathrm{M_{vir}} =$

$4/3\ \pi R_{\rm vir}^3 \bar{\rho}$, we also have $R_{\rm vir} \propto {\rm M_{vir}}^{1/3}$. Hence, Equation B.2 becomes

$$\begin{aligned} R_{core}^2 &\propto \frac{R_{\rm vir}}{\rm M_{vir}} \\ \rightarrow R_{core}^2 &\propto \frac{{\rm M_{vir}}^{1/3}}{\rm M_{vir}} \\ \rightarrow R_{core} &\propto \left({\rm M_{vir}}^{-2/3}\right)^{1/2} \\ \rightarrow R_{core} &\propto {\rm M_{vir}}^{-1/3}. \end{aligned} \tag{B.3}$$

With this scaling relation in mind, the constant of proportionality may be determined through analysis of simulated halos.

Appendix C

Supplementary Figures

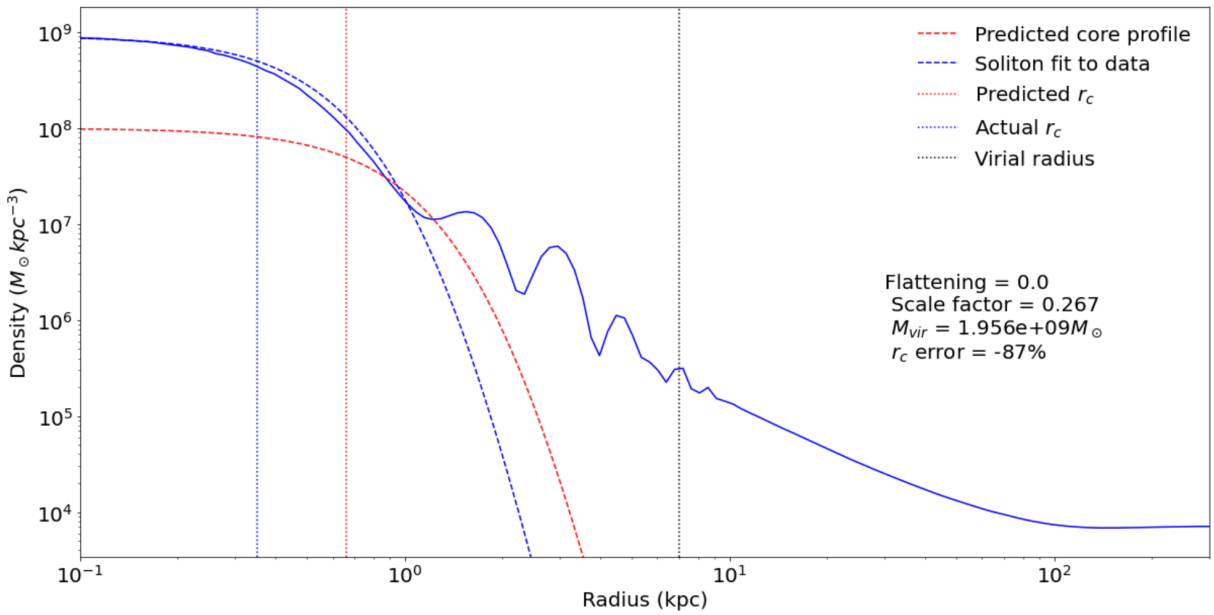

Figure C.1: Spherically averaged density profile at the second overdensity peak in the perturbed $f = 0$ case. A soliton fit to the central profile is provided (blue), as is a soliton profile corresponding to the predicted core radius (red).

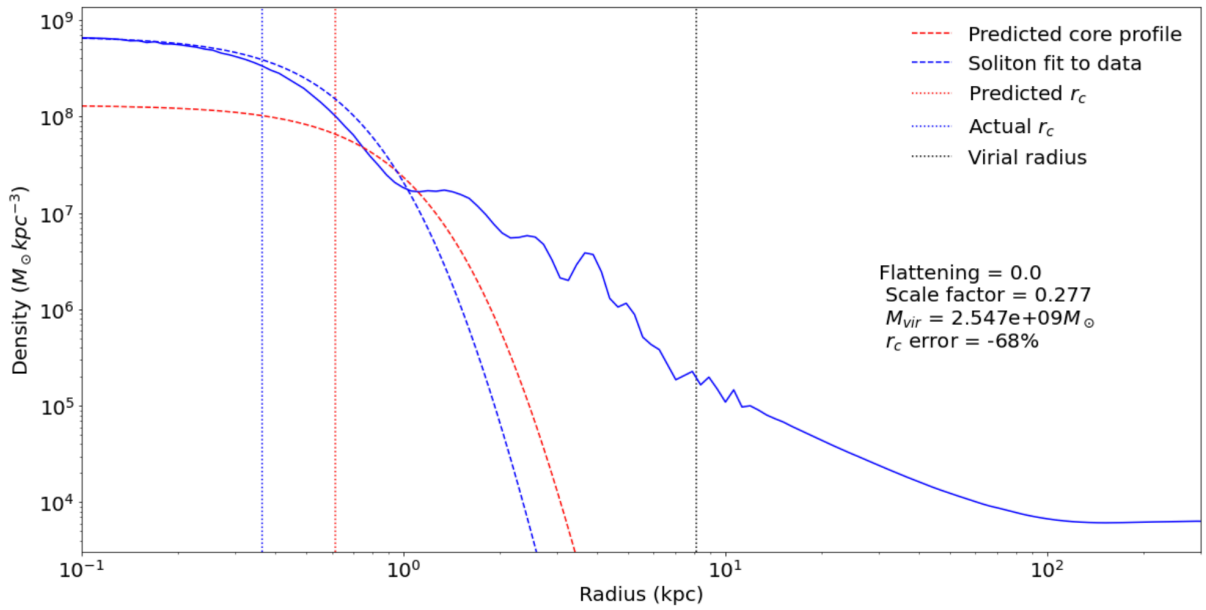

Figure C.2: Spherically averaged density profile at the third overdensity peak in the perturbed $f = 0$ case. A soliton fit to the central profile is provided (blue), as is a soliton profile corresponding to the predicted core radius (red).

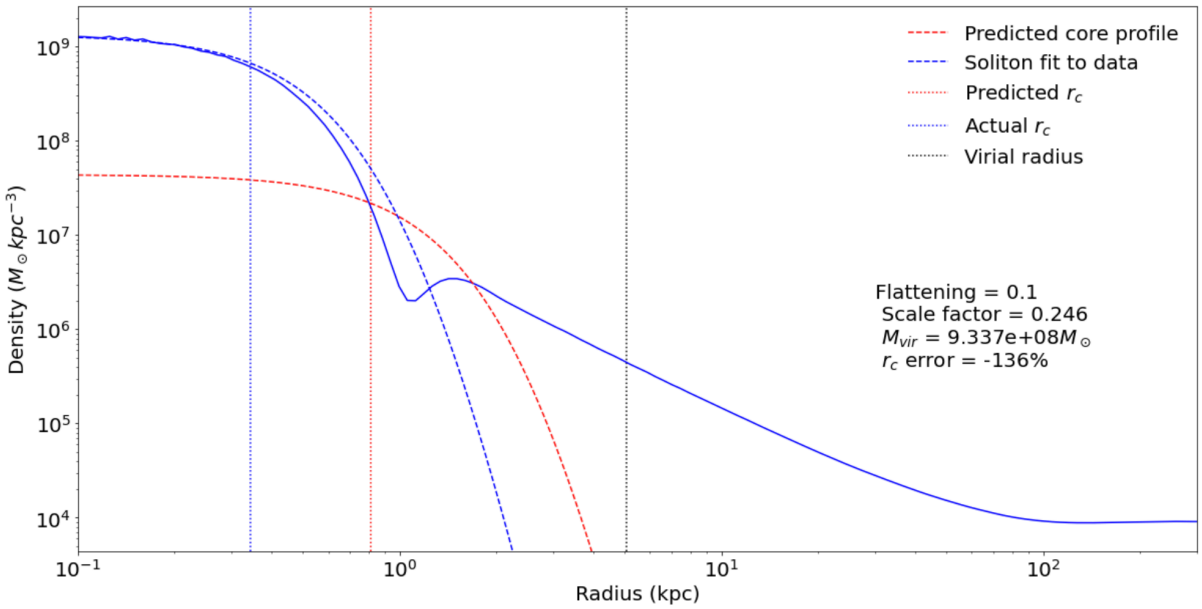

Figure C.3: Spherically averaged density profile at the first overdensity peak in the perturbed $f = 0.1$ case. A soliton fit to the central profile is provided (blue), as is a soliton profile corresponding to the predicted core radius (red).

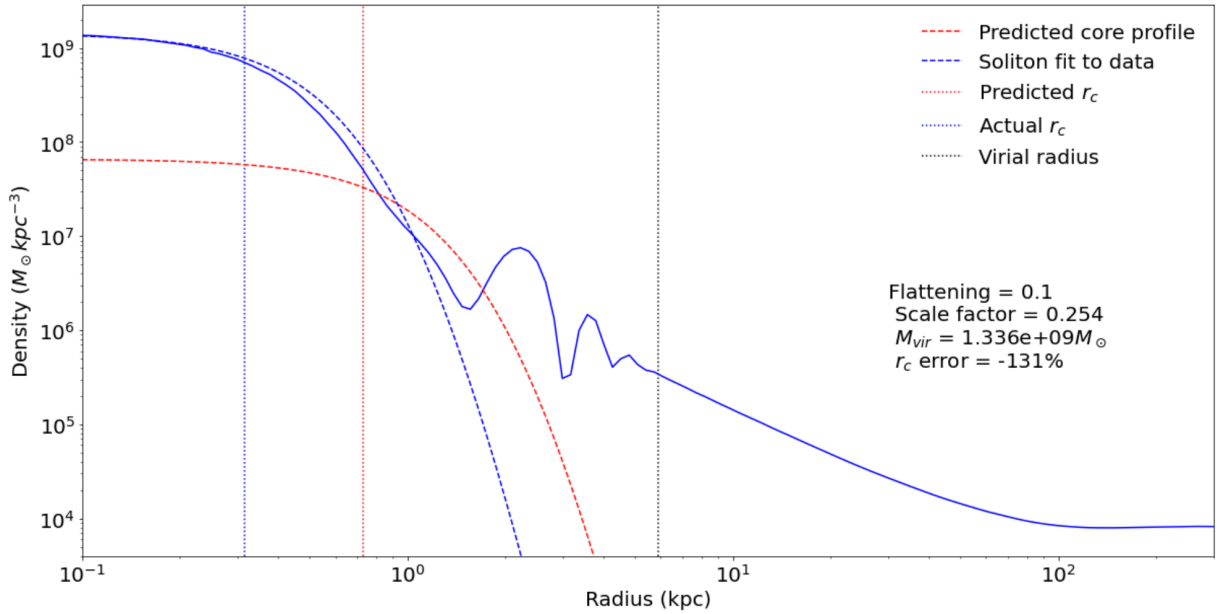

Figure C.4: Spherically averaged density profile at the second overdensity peak in the perturbed $f = 0.1$ case. A soliton fit to the central profile is provided (blue), as is a soliton profile corresponding to the predicted core radius (red).

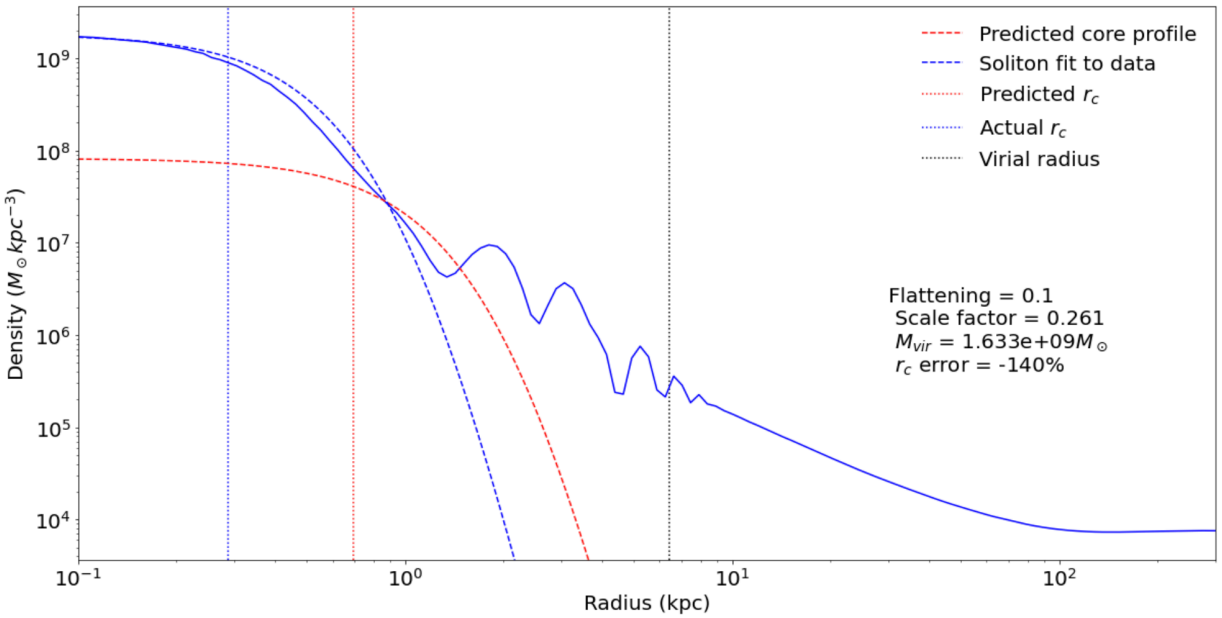

Figure C.5: Spherically averaged density profile at the third overdensity peak in the perturbed $f = 0.1$ case. A soliton fit to the central profile is provided (blue), as is a soliton profile corresponding to the predicted core radius (red).

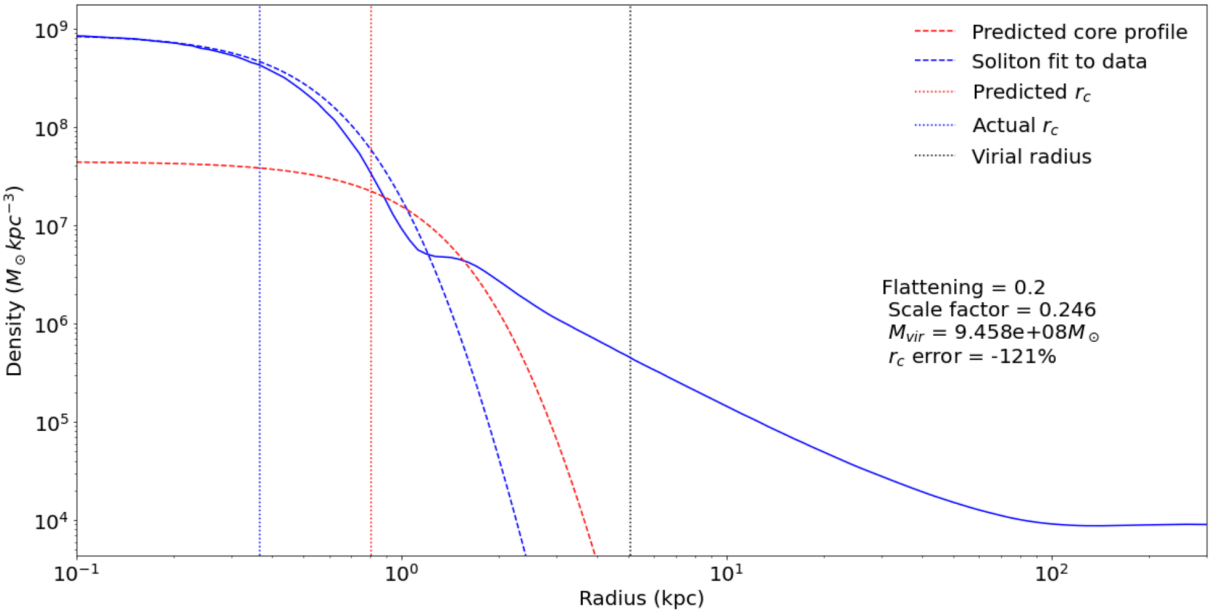

Figure C.6: Spherically averaged density profile at the first overdensity peak in the perturbed $f = 0.2$ case. A soliton fit to the central profile is provided (blue), as is a soliton profile corresponding to the predicted core radius (red).

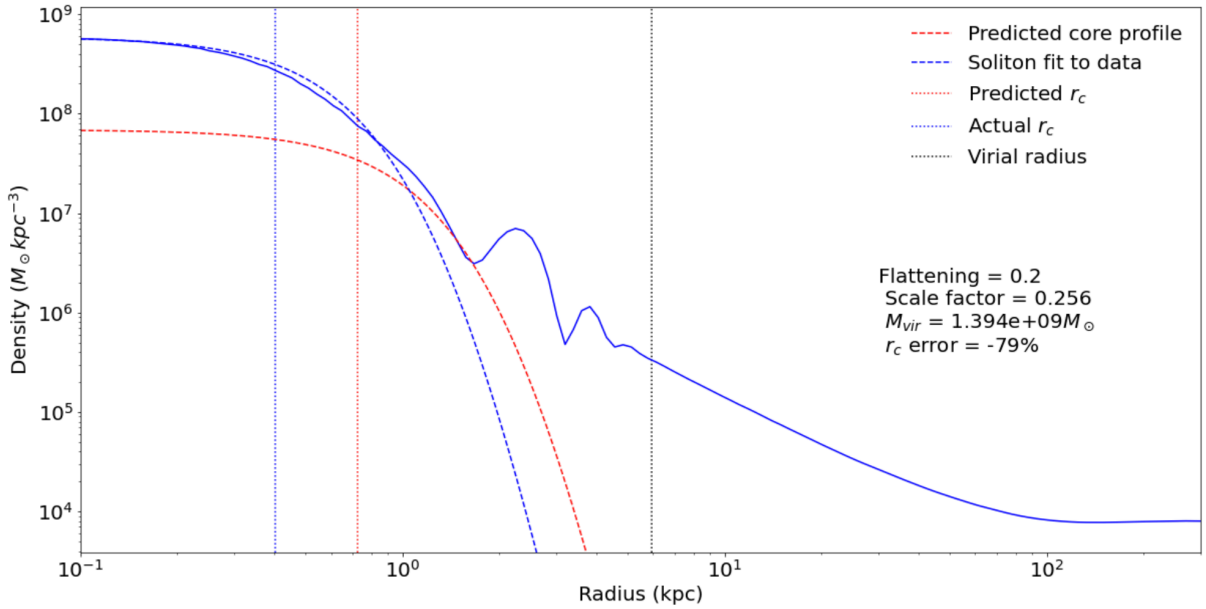

Figure C.7: Spherically averaged density profile at the second overdensity peak in the perturbed $f = 0.2$ case. A soliton fit to the central profile is provided (blue), as is a soliton profile corresponding to the predicted core radius (red).

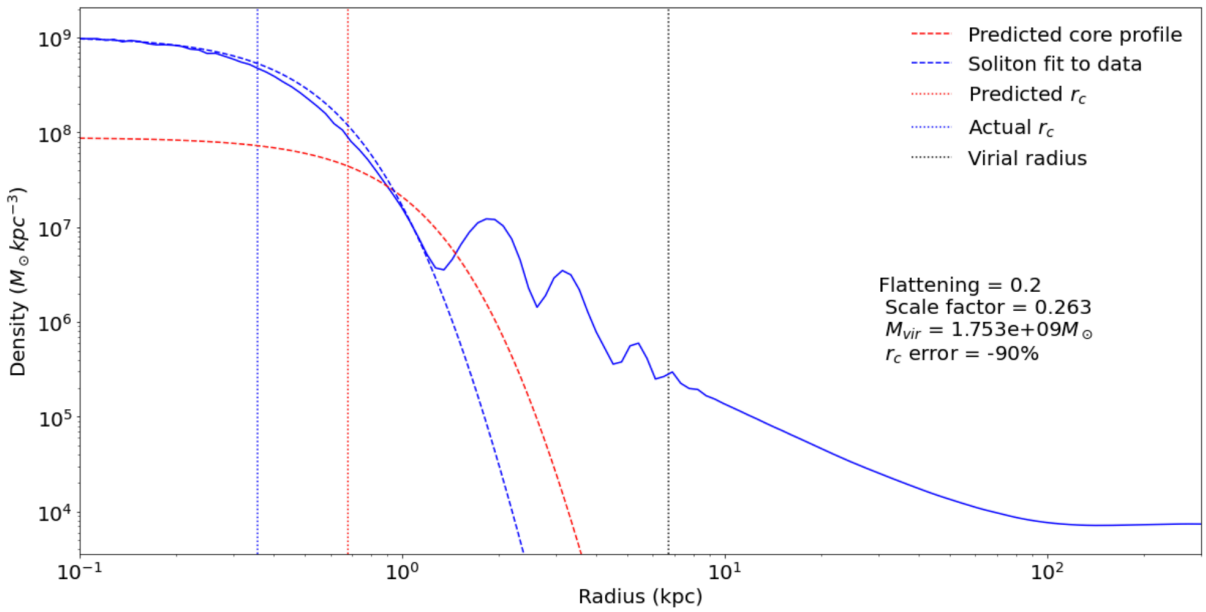

Figure C.8: Spherically averaged density profile at the third overdensity peak in the perturbed $f = 0.2$ case. A soliton fit to the central profile is provided (blue), as is a soliton profile corresponding to the predicted core radius (red).

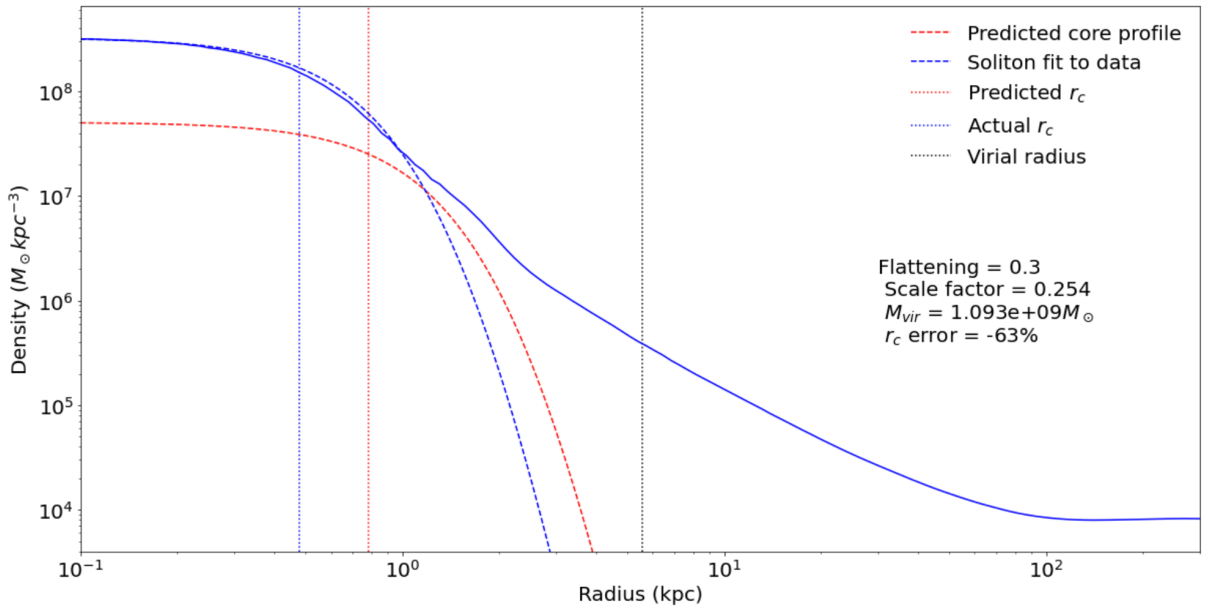

Figure C.9: Spherically averaged density profile at the first overdensity peak in the perturbed $f = 0.3$ case. A soliton fit to the central profile is provided (blue), as is a soliton profile corresponding to the predicted core radius (red).

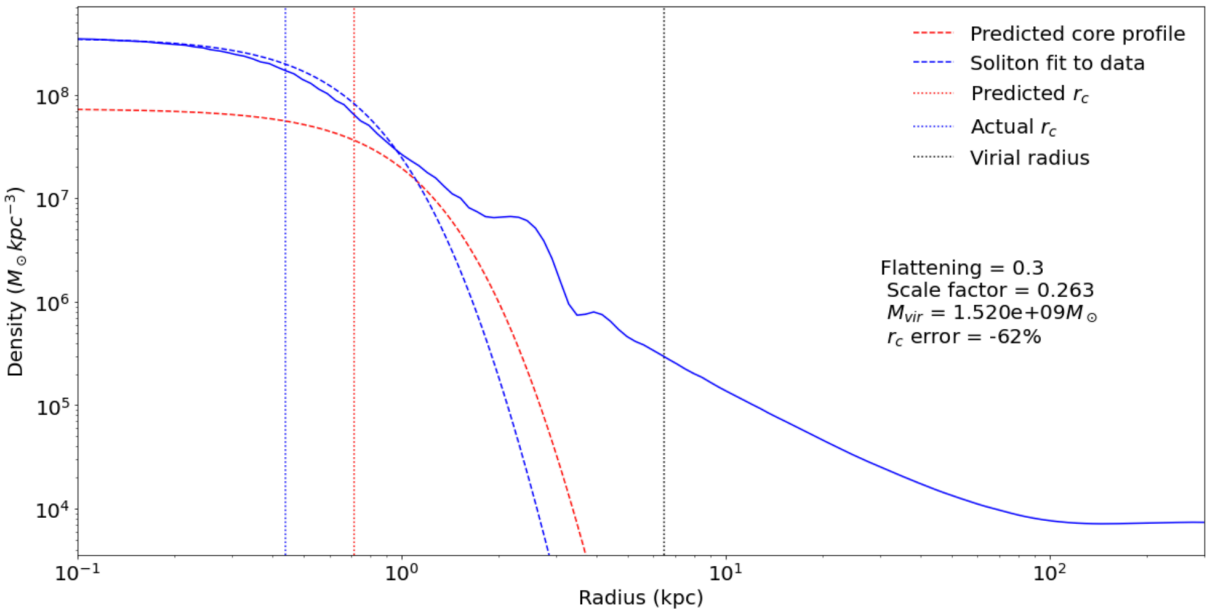

Figure C.10: Spherically averaged density profile at the second overdensity peak in the perturbed $f = 0.3$ case. A soliton fit to the central profile is provided (blue), as is a soliton profile corresponding to the predicted core radius (red).

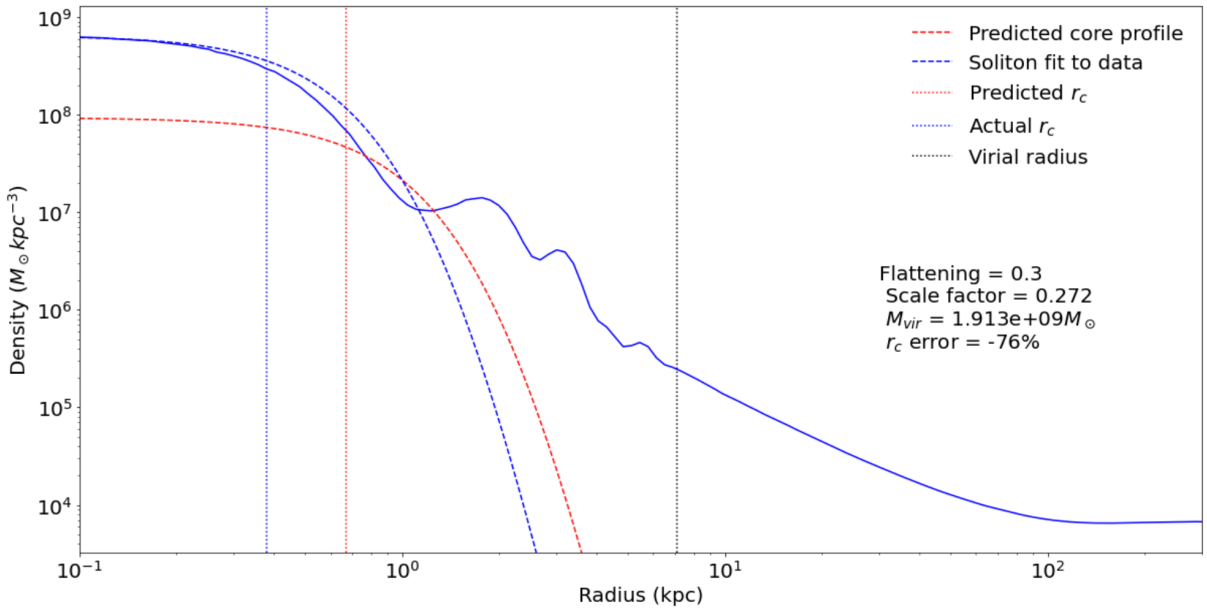

Figure C.11: Spherically averaged density profile at the third overdensity peak in the perturbed $f = 0.3$ case. A soliton fit to the central profile is provided (blue), as is a soliton profile corresponding to the predicted core radius (red).

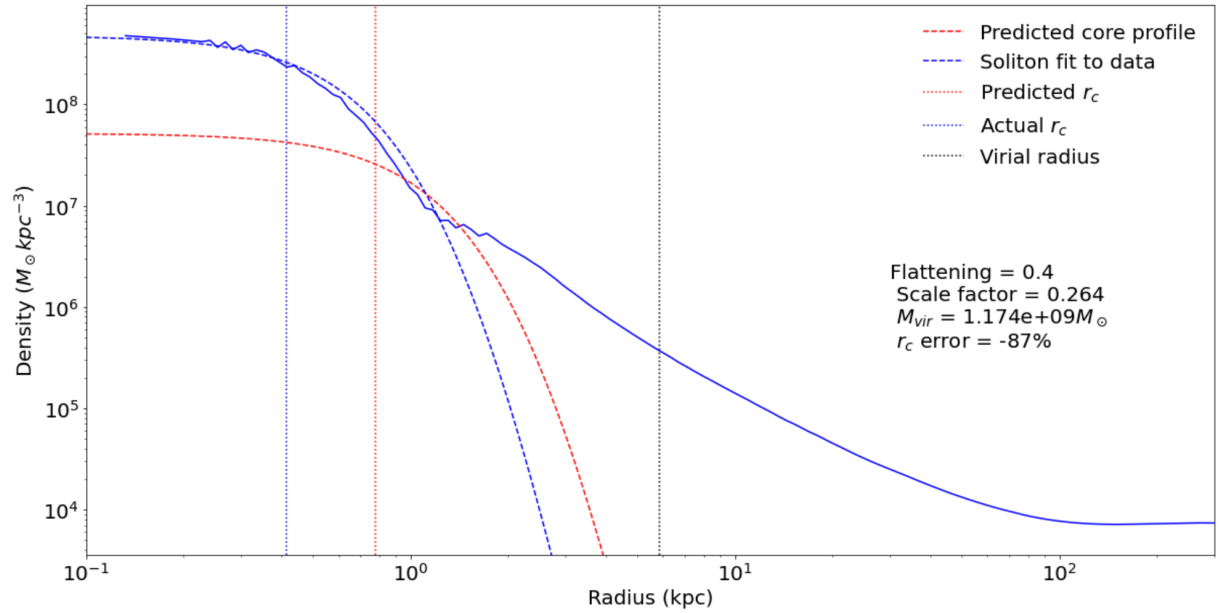

Figure C.12: Spherically averaged density profile at the first overdensity peak in the perturbed $f = 0.4$ case. A soliton fit to the central profile is provided (blue), as is a soliton profile corresponding to the predicted core radius (red).

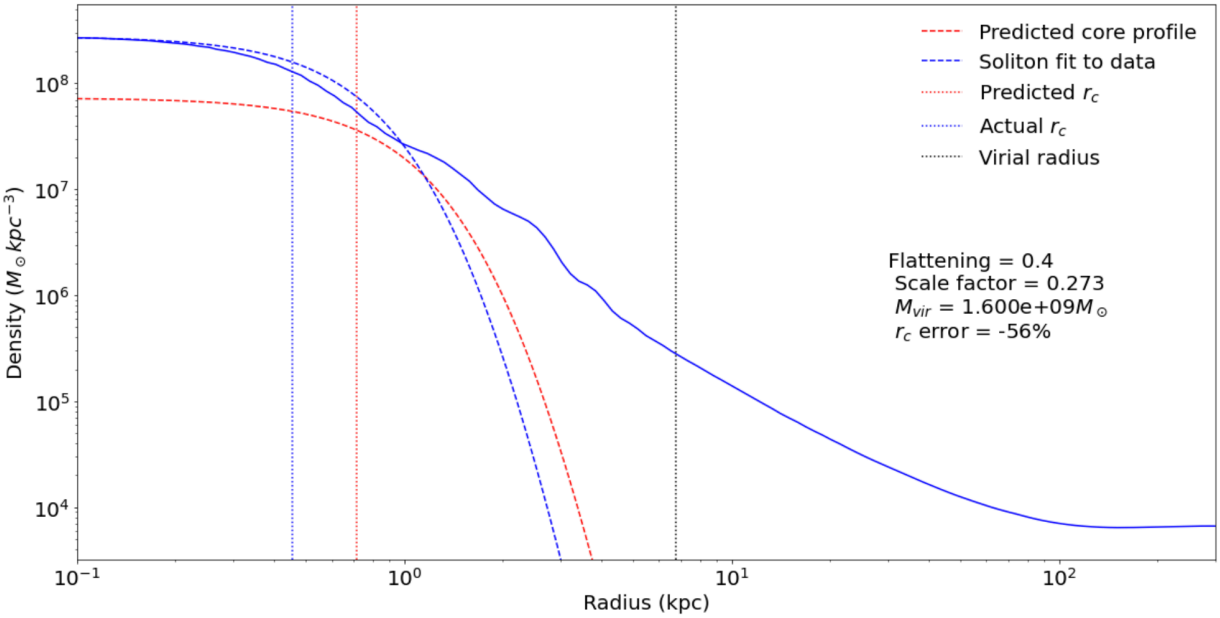

Figure C.13: Spherically averaged density profile at the second overdensity peak in the perturbed $f = 0.4$ case. A soliton fit to the central profile is provided (blue), as is a soliton profile corresponding to the predicted core radius (red).

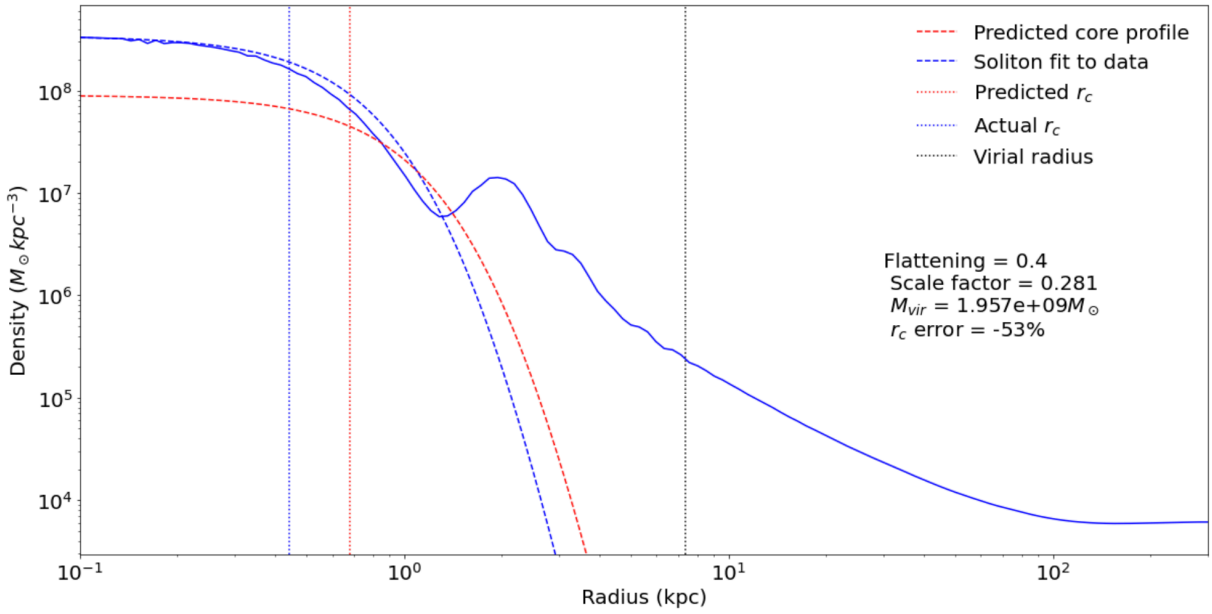

Figure C.14: Spherically averaged density profile at the third overdensity peak in the perturbed $f = 0.4$ case. A soliton fit to the central profile is provided (blue), as is a soliton profile corresponding to the predicted core radius (red).

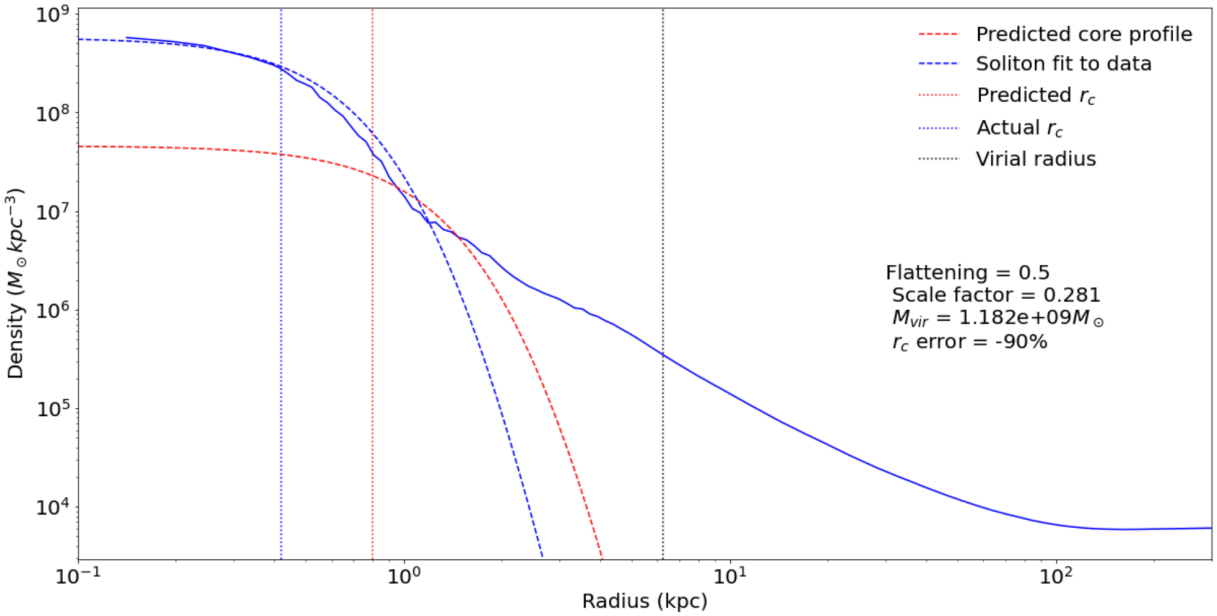

Figure C.15: Spherically averaged density profile at the first overdensity peak in the perturbed $f = 0.5$ case. A soliton fit to the central profile is provided (blue), as is a soliton profile corresponding to the predicted core radius (red).

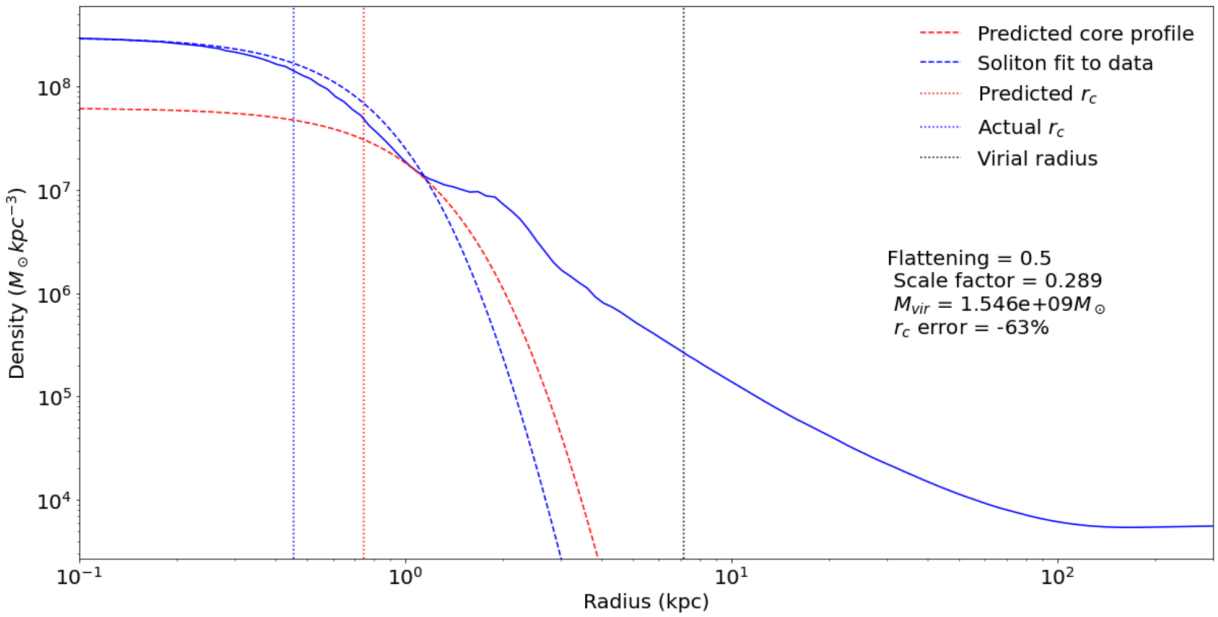

Figure C.16: Spherically averaged density profile at the second overdensity peak in the perturbed $f = 0.5$ case. A soliton fit to the central profile is provided (blue), as is a soliton profile corresponding to the predicted core radius (red).

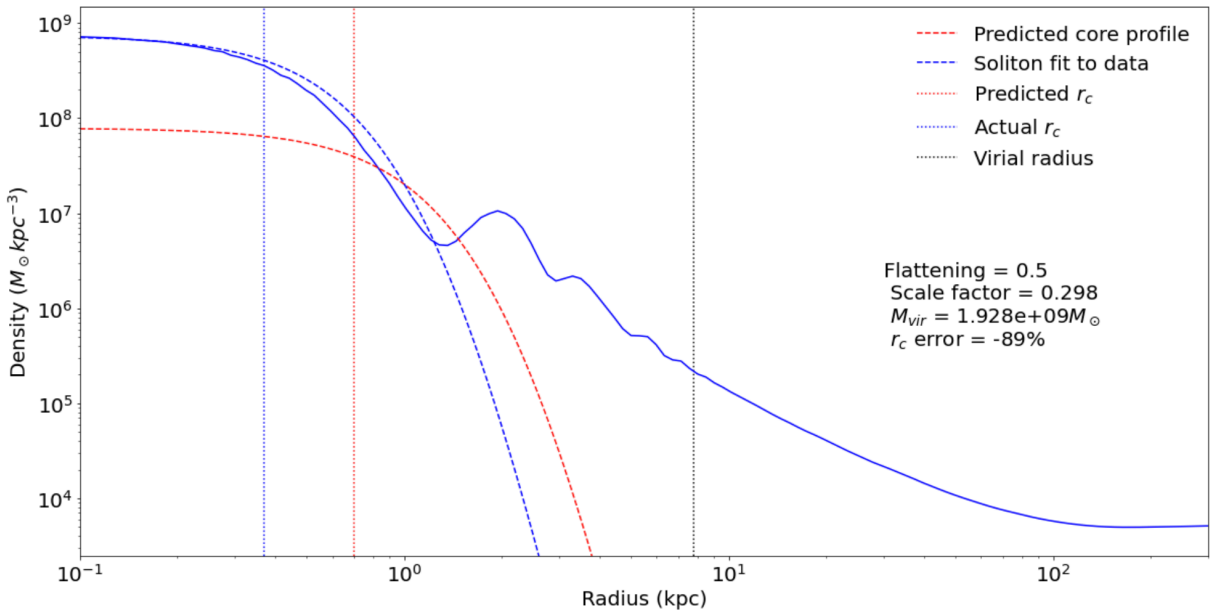

Figure C.17: Spherically averaged density profile at the third overdensity peak in the perturbed $f = 0.5$ case. A soliton fit to the central profile is provided (blue), as is a soliton profile corresponding to the predicted core radius (red).

Bibliography

[1] J. D. Hunter, *Matplotlib: A 2D Graphics Environment*, *Comput. Sci. Eng.* **9** (2007) 90–95.

[2] M. J. Turk, B. D. Smith, J. S. Oishi, S. Skory, S. W. Skillman, T. Abel et al., *yt: A Multi-Code Analysis Toolkit for Astrophysical Simulation Data*, *Astrophys. J. Suppl.* **192** (2011) 9, [1011.3514].

[3] S. van der Walt, S. C. Colbert and G. Varoquaux, *The NumPy Array: A Structure for Efficient Numerical Computation*, *Comput. Sci. Eng.* **13** (2011) 22–30.

[4] P. Virtanen et al., *SciPy 1.0–Fundamental Algorithms for Scientific Computing in Python*, 1907.10121.

[5] A. Meurer et al., *SymPy: symbolic computing in Python*, *PeerJ Comput. Sci.* **3** (2017) e103.

[6] H. Gomersall, *pyFFTW*, June, 2016. 10.5281/zenodo.59508.

[7] M. Frigo and S. G. Johnson, *The Design and Implementation of FFTW3*, *IEEE Proc.* **93** (2005) 216–231.

[8] D. Cooke, T. Hochberg, F. Alted, I. Vilata, M. Wiebe, G. de Menten et al., *NumExpr: Fast numerical expression evaluator for NumPy*, Aug., 2018. 10.5281/zenodo.1492916.

[9] F. Edwards, E. Kendall, S. Hotchkiss and R. Easther, *PyUltraLight: A Pseudo-Spectral Solver for Ultralight Dark Matter Dynamics*, *JCAP* **10** (2018) 027, [1807.04037].

[10] E. Kendall and R. Easther, *The Core-Cusp Problem Revisited: ULDM vs. CDM*, *Publ. Astron. Soc. Austral.* **37** (2020) e009, [1908.02508].

[11] A. Einstein, *A Generalized Theory of Gravitation*, *Rev. Mod. Phys.* **20** (1948) 35–39.

[12] F. W. Dyson, A. S. Eddington and C. Davidson, *IX. A determination of the deflection of light by the sun's gravitational field, from observations made at the total eclipse of May 29, 1919*, *Philosophical Transactions of the Royal Society of London A* **220** (1920) 291—-333.

[13] R. S. "Park, W. M. Folkner, A. S. Konopliv, J. G. Williams, D. E. Smith and M. T. Zuber, *Precession of Mercury's Perihelion from Ranging to the MESSENGER Spacecraft*, *The Astronomical Journal* **153** (2017) .

[14] C. M. Will, *The Confrontation between General Relativity and Experiment*, *Living Rev. Rel.* **17** (2014) 4, [1403.7377].

[15] D. Castelvecchi and A. Witze, *Einstein's gravitational waves found at last*, *Nature* (Feb, 2016) .

[16] Event Horizon Telescope collaboration, K. Akiyama et al., *First M87 Event Horizon Telescope Results. I. The Shadow of the Supermassive Black Hole*, *Astrophys. J. Lett.* **875** (2019) L1, [1906.11238].

[17] B. Schulz, *Review on the quantization of gravity*, 1409.7977.

[18] Planck collaboration, P. A. R. Ade et al., *Planck 2015 results. XIII. Cosmological parameters*, *Astron. Astrophys.* **594** (2016) A13, [1502.01589].

[19] R. Scarpa, *Modified newtonian dynamics, an introductory review*, *AIP Conf. Proc.* **822** (2006) 253–265, [astro-ph/0601478].

[20] E. Pointecouteau and J. Silk, *New constraints on modified Newtonian dynamics from galaxy clusters*, *Monthly Notices of the Royal Astronomical Society* **364** (12, 2005) 654–658.

[21] B. Famaey and S. S. McGaugh, *Modified Newtonian Dynamics (MOND): Observational Phenomenology and Relativistic Extensions*, *Living Reviews in Relativity* **15** (Sep, 2012) 10.

[22] J. Lighthill, J. M. T. Thompson, A. K. Sen, A. G. M. Last, D. T. Tritton and P. Mathias, *The recently recognized failure of predictability in newtonian dynamics [and discussion]*, *Proceedings of the Royal Society of London. Series A, Mathematical and Physical Sciences* **407** (1986) 35–50.

[23] Y. Sofue and V. Rubin, *Rotation curves of spiral galaxies*, *Ann. Rev. Astron. Astrophys.* **39** (2001) 137–174, [astro-ph/0010594].

[24] S. S. McGaugh, V. C. Rubin and W. J. G. de Blok, *High - resolution rotation curves of low surface brightness galaxies: Data*, *Astron. J.* **122** (2001) 2381–2395, [astro-ph/0107326].

[25] T. E. Pickering, J. F. Navarro, H. W. Rix and C. D. Impey, *Optical Rotation Curves of Low Surface Brightness Galaxies*, in *Galactic Halos* (D. Zaritsky, ed.), vol. 136 of *Astronomical Society of the Pacific Conference Series*, p. 199, Jan., 1998.

[26] T. P. K. Martinsson, M. A. W. Verheijen, K. B. Westfall, M. A. Bershady, D. R. Andersen and R. A. Swaters, *The DiskMass Survey. VII. The distribution of luminous and dark matter in spiral galaxies*, **557** (Sept., 2013) A131, [1308.0336].

[27] S. S. McGaugh, F. Lelli and J. M. Schombert, *Radial Acceleration Relation in Rotationally Supported Galaxies*, **117** (Nov., 2016) 201101, [1609.05917].

[28] K. Umetsu, *Cluster–galaxy weak lensing*, *The Astronomy and Astrophysics Review* **28** (Nov, 2020) 7.

[29] H. Hoekstra and B. Jain, *Weak gravitational lensing and its cosmological applications*, *Annual Review of Nuclear and Particle Science* **58** (2008) 99–123.

[30] D. Clowe, M. Bradac, A. H. Gonzalez, M. Markevitch, S. W. Randall, C. Jones et al., *A direct empirical proof of the existence of dark matter*, *Astrophys. J. Lett.* **648** (2006) L109–L113, [astro-ph/0608407].

[31] M. Bradač, S. W. Allen, T. Treu, H. Ebeling, R. Massey, R. G. Morris et al., *Revealing the Properties of Dark Matter in the Merging Cluster MACS J0025.4-1222*, **687** (Nov., 2008) 959–967, [0806.2320].

[32] S.-I. Tam et al., *The distribution of dark matter and gas spanning 6 Mpc around the post-merger galaxy cluster MS 0451−03*, *Mon. Not. Roy. Astron. Soc.* **496** (2020) 4032–4050, [2006.10156].

[33] W. A. Dawson, D. Wittman, M. J. Jee, P. Gee, J. P. Hughes, J. A. Tyson et al., *Discovery of a dissociative galaxy cluster merger with large physical separation*, *The Astrophysical Journal* **747** (feb, 2012) L42.

[34] K. Freese, *Status of Dark Matter in the Universe*, *Int. J. Mod. Phys.* **1** (2017) 325–355, [1701.01840].

[35] J. Chluba and D. Grin, *CMB spectral distortions from small-scale isocurvature fluctuations*, *Mon. Not. Roy. Astron. Soc.* **434** (2013) 1619–1635, [1304.4596].

[36] J. B. Dent, D. A. Easson and H. Tashiro, *Cosmological constraints from cmb distortion*, *Phys. Rev. D* **86** (Jul, 2012) 023514.

[37] LUX collaboration, D. S. Akerib et al., *Effective field theory analysis of the first LUX dark matter search*, *Phys. Rev. D* **103** (2021) 122005, [2003.11141].

[38] G. Adhikari, P. Adhikari, E. B. de Souza, N. Carlin, S. Choi, M. Djamal et al., *An experiment to search for dark-matter interactions using sodium iodide detectors*, *Nature* **564** (Dec, 2018) 83–86.

[39] J. Billard et al., *Direct Detection of Dark Matter – APPEC Committee Report*, 2104.07634.

[40] C. Alcock, C. W. Akerlof, R. A. Allsman, T. S. Axelrod, D. P. Bennett, S. Chan et al., *Possible gravitational microlensing of a star in the large magellanic cloud*, *Nature* **365** (Oct, 1993) 621–623.

[41] K. Griest, *The Nature of the dark matter*, *Proc. Int. Sch. Phys. Fermi* **132** (1996) 343–378, [astro-ph/9510089].

[42] S. Clark, B. Dutta, Y. Gao, L. E. Strigari and S. Watson, *Planck Constraint on Relic Primordial Black Holes*, *Phys. Rev. D* **95** (2017) 083006, [1612.07738].

[43] H. Kim, *A constraint on light primordial black holes from the interstellar medium temperature*, 2007.07739.

[44] R. D. Peccei and H. R. Quinn, *Constraints imposed by* CP *conservation in the presence of pseudoparticles*, *Phys. Rev. D* **16** (Sep, 1977) 1791–1797.

[45] R. A. Battye, B. Garbrecht, J. I. McDonald, F. Pace and S. Srinivasan, *Dark matter axion detection in the radio/mm waveband*, *Phys. Rev. D* **102** (Jul, 2020) 023504.

[46] J. Kopp, *Sterile Neutrinos as Dark Matter Candidates*, in *Les Houches summer school on Dark Matter*, 9, 2021. 2109.00767.

[47] R. Kumar Barman, G. Belanger and R. M. Godbole, *Status of low mass LSP in SUSY*, *Eur. Phys. J. ST* **229** (2020) 3159–3185, [2010.11674].

[48] G. Bertone and D. Hooper, *History of dark matter*, *Rev. Mod. Phys.* **90** (2018) 045002, [1605.04909].

[49] Planck Collaboration, Y. Akrami, M. Ashdown, J. Aumont, C. Baccigalupi, M. Ballardini et al., *Planck 2018 results. VII. Isotropy and statistics of the CMB*, **641** (Sept., 2020) A7, [1906.02552].

[50] Planck collaboration, N. Aghanim et al., *Planck 2018 results. VI. Cosmological parameters*, *Astron. Astrophys.* **641** (2020) A6, [1807.06209].

[51] C. L. Bennett, D. Larson, J. L. Weiland, N. Jarosik, G. Hinshaw, N. Odegard et al., *Nine-year Wilkinson Microwave Anisotropy Probe (WMAP) Observations: Final Maps and Results*, **208** (Oct., 2013) 20, [1212.5225].

[52] WMAP collaboration, D. N. Spergel et al., *First year Wilkinson Microwave Anisotropy Probe (WMAP) observations: Determination of cosmological parameters*, *Astrophys. J. Suppl.* **148** (2003) 175–194, [astro-ph/0302209].

[53] G. F. R. Ellis and H. van Elst, *Cosmological models: Cargese lectures 1998*, *NATO Sci. Ser. C* **541** (1999) 1–116, [gr-qc/9812046].

[54] J. R. Ellis, J. S. Hagelin, D. V. Nanopoulos, K. A. Olive and M. Srednicki, *Supersymmetric Relics from the Big Bang*, *Nucl. Phys. B* **238** (1984) 453–476.

[55] G. Jungman, M. Kamionkowski and K. Griest, *Supersymmetric dark matter*, *Phys. Rept.* **267** (1996) 195–373, [hep-ph/9506380].

[56] A. Canepa, *Searches for supersymmetry at the large hadron collider*, *Reviews in Physics* **4** (2019) 100033.

[57] G. Kauffmann, J. M. Colberg, A. Diaferio and S. D. M. White, *Clustering of galaxies in a hierarchical universe — I. Methods and results at z = 0*, *Monthly Notices of the Royal Astronomical Society* **303** (02, 1999) 188–206.

[58] A. M. Hopkins, *On the Evolution of Star-forming Galaxies*, **615** (Nov., 2004) 209–221, [astro-ph/0407170].

[59] P. J. E. Peebles, *Large-scale background temperature and mass fluctuations due to scale-invariant primeval perturbations*, **263** (Dec., 1982) L1–L5.

[60] T. K. Chan, D. Kereš, J. Oñorbe, P. F. Hopkins, A. L. Muratov, C.-A. Faucher-Giguère et al., *The impact of baryonic physics on the structure of dark matter haloes: the view from the FIRE cosmological simulations*, *Monthly Notices of the Royal Astronomical Society* **454** (10, 2015) 2981–3001.

[61] V. Springel, S. D. M. White, A. Jenkins, C. S. Frenk, N. Yoshida, L. Gao et al., *Simulations of the formation, evolution and clustering of galaxies and quasars*, **435** (June, 2005) 629–636, [astro-ph/0504097].

[62] M. Boylan-Kolchin, V. Springel, S. D. M. White, A. Jenkins and G. Lemson, *Resolving cosmic structure formation with the Millennium-II Simulation*, **398** (Sept., 2009) 1150–1164, [0903.3041].

[63] Q. Guo et al., *Galaxies in the EAGLE hydrodynamical simulation and in the Durham and Munich semi-analytical models*, *Mon. Not. Roy. Astron. Soc.* **461** (2016) 3457–3482, [1512.00015].

[64] T. Sawala et al., *The APOSTLE simulations: solutions to the Local Group's cosmic puzzles*, *Mon. Not. Roy. Astron. Soc.* **457** (2016) 1931–1943, [1511.01098].

[65] D. S. Aguado, R. Ahumada, A. Almeida, S. F. Anderson, B. H. Andrews, B. Anguiano et al., *The Fifteenth Data Release of the Sloan Digital Sky Surveys: First Release of MaNGA-derived Quantities, Data Visualization Tools, and Stellar Library*, **240** (Feb., 2019) 23, [1812.02759].

[66] M. Lares, H. E. Luparello, V. Maldonado, A. N. Ruiz, D. J. Paz, L. Ceccarelli et al., *Voids and Superstructures: correlations and induced large-scale velocity flows*, *Mon. Not. Roy. Astron. Soc.* **470** (2017) 85–94, [1705.06541].

[67] M. V. Costa-Duarte, J. Sodré, L. and F. Durret, *Morphological properties of superclusters of galaxies*, **411** (Mar., 2011) 1716–1726, [1010.0981].

[68] J. Ruiz-Zapatero et al., *Geometry vs growth: Internal consistency of the flat ΛCDM model with KiDS-1000*, 2105.09545.

[69] A. Shafieloo and D. K. Hazra, *Consistency of the Planck CMB data and ΛCDM cosmology*, *JCAP* **04** (2017) 012, [1610.07402].

[70] DES collaboration, T. M. C. Abbott et al., *Dark Energy Survey Year 3 Results: Cosmological Constraints from Galaxy Clustering and Weak Lensing*, 2105.13549.

[71] M. Drees, R. Godbole and P. Roy, *Theory and phenomenology of sparticles: An account of four-dimensional N=1 supersymmetry in high energy physics*. 2004.

[72] G. Belanger, F. Boudjema, A. Pukhov and A. Semenov, *MicrOMEGAs: A Program for calculating the relic density in the MSSM*, *Comput. Phys. Commun.* **149** (2002) 103–120, [hep-ph/0112278].

[73] K. Griest and M. Kamionkowski, *Supersymmetric dark matter*, *Physics Reports* **333-334** (2000) 167–182.

[74] N. Craig and A. Katz, *The Fraternal WIMP Miracle*, *JCAP* **10** (2015) 054, [1505.07113].

[75] P. Draper and H. Rzehak, *A Review of Higgs Mass Calculations in Supersymmetric Models*, *Phys. Rept.* **619** (2016) 1–24, [1601.01890].

[76] B. Liu, *Supersymmetry and the Minimal Supersymmetric Standard Model*, pp. 19–24. Springer New York, New York, NY, 2011.

[77] M. Badziak and K. Sakurai, *Explanation of electron and muon $g-2$ anomalies in the MSSM*, *JHEP* **10** (2019) 024, [1908.03607].

[78] M. W. Goodman and E. Witten, *Detectability of certain dark-matter candidates*, *Phys. Rev. D* **31** (Jun, 1985) 3059–3063.

[79] G. Duda, A. Kemper and P. Gondolo, *Model Independent Form Factors for Spin Independent Neutralino-Nucleon Scattering from Elastic Electron Scattering Data*, *JCAP* **04** (2007) 012, [hep-ph/0608035].

[80] O. Fischer et al., *Unveiling Hidden Physics at the LHC*, 2109.06065.

[81] X. Tata, *Natural supersymmetry: status and prospects*, *Eur. Phys. J. ST* **229** (2020) 3061–3083, [2002.04429].

[82] H. Baer, V. Barger, S. Salam, D. Sengupta and K. Sinha, *Status of weak scale supersymmetry after LHC Run 2 and ton-scale noble liquid WIMP searches*, *Eur. Phys. J. ST* **229** (2020) 3085–3141, [2002.03013].

[83] R. Bernabei et al., *Final model independent result of DAMA/LIBRA-phase1*, *Eur. Phys. J. C* **73** (2013) 2648, [1308.5109].

[84] A. H. G. Peter, V. Gluscevic, A. M. Green, B. J. Kavanagh and S. K. Lee, *WIMP physics with ensembles of direct-detection experiments*, *Phys. Dark Univ.* **5-6** (2014) 45–74, [1310.7039].

[85] PICASSO collaboration, M.-C. Piro, *Status of the PICASSO experiment for spin-dependent Dark Matter searches*, 1005.5455.

[86] TEXONO Collaboration collaboration, H. B. Li, H. Y. Liao, S. T. Lin, S. K. Liu, L. Singh, M. K. Singh et al., *Limits on spin-independent couplings of wimp dark matter with a p-type point-contact germanium detector*, *Phys. Rev. Lett.* **110** (Jun, 2013) 261301.

[87] CDMS-II collaboration, Z. Ahmed et al., *Dark Matter Search Results from the CDMS II Experiment*, *Science* **327** (2010) 1619–1621, [0912.3592].

[88] PandaX-II collaboration, A. Tan et al., *Dark Matter Results from First 98.7 Days of Data from the PandaX-II Experiment*, *Phys. Rev. Lett.* **117** (2016) 121303, [1607.07400].

[89] LUX collaboration, D. S. Akerib et al., *Results from a search for dark matter in the complete LUX exposure*, *Phys. Rev. Lett.* **118** (2017) 021303, [1608.07648].

[90] D. H. Weinberg, J. S. Bullock, F. Governato, R. Kuzio de Naray and A. H. G. Peter, *Cold dark matter: controversies on small scales*, *Proc. Nat. Acad. Sci.* **112** (2015) 12249–12255, [1306.0913].

[91] T. Nakama, J. Chluba and M. Kamionkowski, *Shedding light on the small-scale crisis with CMB spectral distortions*, *Phys. Rev. D* **95** (2017) 121302, [1703.10559].

[92] J. F. Navarro, C. S. Frenk and S. D. M. White, *The Structure of cold dark matter halos*, *Astrophys. J.* **462** (1996) 563–575, [astro-ph/9508025].

[93] W. J. G. de Blok, *The core-cusp problem*, *Advances in Astronomy* **2010** (Nov, 2009) 789293.

[94] J. S. Bullock and M. Boylan-Kolchin, *Small-scale challenges to the cdm paradigm*, *Annual Review of Astronomy and Astrophysics* **55** (2017) 343–387, [https://doi.org/10.1146/annurev-astro-091916-055313].

[95] B. Moore, T. R. Quinn, F. Governato, J. Stadel and G. Lake, *Cold collapse and the core catastrophe*, *Mon. Not. Roy. Astron. Soc.* **310** (1999) 1147–1152, [astro-ph/9903164].

[96] A. Genina, A. Benítez-Llambay, C. S. Frenk, S. Cole, A. Fattahi, J. F. Navarro et al., *The core-cusp problem: a matter of perspective*, **474** (Feb., 2018) 1398–1411, [1707.06303].

[97] G. Dashyan, J. Silk, G. A. Mamon, Y. Dubois and T. Hartwig, *AGN feedback in dwarf galaxies?*, **473** (Feb., 2018) 5698–5703, [1710.05900].

[98] P. Madau, S. Shen and F. Governato, *Dark Matter Heating and Early Core Formation in Dwarf Galaxies*, **789** (July, 2014) L17, [1405.2577].

[99] J. I. Read, O. Agertz and M. L. M. Collins, *Dark matter cores all the way down*, *Monthly Notices of the Royal Astronomical Society* **459** (03, 2016) 2573–2590.

[100] A. A. Klypin, A. V. Kravtsov, O. Valenzuela and F. Prada, *Where are the missing Galactic satellites?*, *Astrophys. J.* **522** (1999) 82–92, [astro-ph/9901240].

[101] B. Moore, S. Ghigna, F. Governato, G. Lake, T. R. Quinn, J. Stadel et al., *Dark matter substructure within galactic halos*, *Astrophys. J. Lett.* **524** (1999) L19–L22, [astro-ph/9907411].

[102] J. S. Bullock, A. V. Kravtsov and D. H. Weinberg, *Hierarchical galaxy formation and substructure in the galaxy's stellar halo*, *The Astrophysical Journal* **548** (feb, 2001) 33–46.

[103] S. Y. Kim, A. H. G. Peter and J. R. Hargis, *Missing satellites problem: Completeness corrections to the number of satellite galaxies in the milky way are consistent with cold dark matter predictions*, *Phys. Rev. Lett.* **121** (Nov, 2018) 211302.

[104] S. Garrison-Kimmel, M. Boylan-Kolchin, J. S. Bullock and E. N. Kirby, *Too big to fail in the Local Group*, *Monthly Notices of the Royal Astronomical Society* **444** (08, 2014) 222–236.

[105] S. Garrison-Kimmel, M. Boylan-Kolchin, J. S. Bullock and E. N. Kirby, *Too big to fail in the Local Group*, **444** (Oct., 2014) 222–236, [1404.5313].

[106] J. P. Ostriker, E. Choi, A. Chow and K. Guha, *Mind the Gap: Is the Too Big to Fail Problem Resolved?*, **885** (Nov., 2019) 97, [1904.10471].

[107] V. H. Robles and J. S. Bullock, *Orbital pericenters and the inferred dark matter halo structure of satellite galaxies*, *Mon. Not. Roy. Astron. Soc.* **503** (2021) 5232–5237, [2012.07865].

[108] W. Hu, R. Barkana and A. Gruzinov, *Cold and fuzzy dark matter*, *Phys. Rev. Lett.* **85** (2000) 1158–1161, [astro-ph/0003365].

[109] R. Hlozek, D. Grin, D. J. E. Marsh and P. G. Ferreira, *A search for ultralight axions using precision cosmological data*, *Phys. Rev. D* **91** (2015) 103512, [1410.2896].

[110] W. J. Marciano, A. Masiero, P. Paradisi and M. Passera, *Contributions of axionlike particles to lepton dipole moments*, *Phys. Rev. D* **94** (2016) 115033, [1607.01022].

[111] D. Chang, W.-F. Chang, C.-H. Chou and W.-Y. Keung, *Large two loop contributions to g-2 from a generic pseudoscalar boson*, *Phys. Rev. D* **63** (2001) 091301, [hep-ph/0009292].

[112] C. Baldenegro, S. Fichet, G. von Gersdorff and C. Royon, *Searching for axion-like particles with proton tagging at the LHC*, *JHEP* **06** (2018) 131, [1803.10835].

[113] F. Lelli, S. S. McGaugh and J. M. Schombert, *SPARC: Mass Models for 175 Disk Galaxies with Spitzer Photometry and Accurate Rotation Curves*, *Astron. J.* **152** (2016) 157, [1606.09251].

[114] B. Schwabe, M. Gosenca, C. Behrens, J. C. Niemeyer and R. Easther, *Simulating mixed fuzzy and cold dark matter*, *Phys. Rev. D* **102** (2020) 083518, [2007.08256].

[115] D. J. Gross, *The role of symmetry in fundamental physics*, *Proceedings of the National Academy of Sciences* **93** (1996) 14256–14259, [https://www.pnas.org/content/93/25/14256.full.pdf].

[116] B. Pontecorvo, *Neutrino Experiments and the Problem of Conservation of Leptonic Charge*, *Soviet Journal of Experimental and Theoretical Physics* **26** (May, 1968) 984.

[117] L. Hui, J. P. Ostriker, S. Tremaine and E. Witten, *Ultralight scalars as cosmological dark matter*, *Phys. Rev. D* **95** (2017) 043541, [1610.08297].

[118] A. Arvanitaki, S. Dimopoulos, S. Dubovsky, N. Kaloper and J. March-Russell, *String Axiverse*, *Phys. Rev. D* **81** (2010) 123530, [0905.4720].

[119] M. Safarzadeh and D. N. Spergel, *Ultra-light Dark Matter is Incompatible with the Milky Way's Dwarf Satellites*, 1906.11848.

[120] L. Hui, *Wave Dark Matter*, 2101.11735.

[121] A. Maleki, S. Baghram and S. Rahvar, *Constraint on the mass of fuzzy dark matter from the rotation curve of the Milky Way*, *Phys. Rev. D* **101** (2020) 103504, [2001.04454].

[122] J. L. Cervantes-Cota and G. Smoot, *Cosmology today-A brief review*, *AIP Conf. Proc.* **1396** (2011) 28–52, [1107.1789].

[123] D. J. E. Marsh, *Axion Cosmology*, *Phys. Rept.* **643** (2016) 1–79, [1510.07633].

[124] J. Preskill, M. B. Wise and F. Wilczek, *Cosmology of the invisible axion*, *Physics Letters B* **120** (1983) 127–132.

[125] G. Gelmini and P. Gondolo, *DM Production Mechanisms*, 1009.3690.

[126] L. Husdal, *On Effective Degrees of Freedom in the Early Universe*, *Galaxies* **4** (2016) 78, [1609.04979].

[127] Particle Data Group collaboration, P. A. Zyla et al., *Review of Particle Physics*, *PTEP* **2020** (2020) 083C01.

[128] J. Veltmaat, J. C. Niemeyer and B. Schwabe, *Formation and structure of ultralight bosonic dark matter halos*, *Phys. Rev. D* **98** (2018) 043509, [1804.09647].

[129] H.-Y. Schive, T. Chiueh and T. Broadhurst, *Cosmic Structure as the Quantum Interference of a Coherent Dark Wave*, *Nature Phys.* **10** (2014) 496–499, [1406.6586].

[130] T.-P. Woo and T. Chiueh, *High-Resolution Simulation on Structure Formation with Extremely Light Bosonic Dark Matter*, *Astrophys. J.* **697** (2009) 850–861, [0806.0232].

[131] M. Garny and T. Konstandin, *Gravitational collapse in the schrödinger-poisson system*, .

[132] H.-Y. Schive, M.-H. Liao, T.-P. Woo, S.-K. Wong, T. Chiueh, T. Broadhurst et al., *Understanding the core-halo relation of quantum wave dark matter from 3d simulations*, *Phys. Rev. Lett.* **113** (Dec, 2014) 261302.

[133] V. H. Robles, J. S. Bullock and M. Boylan-Kolchin, *Scalar Field Dark Matter: Helping or Hurting Small-Scale Problems in Cosmology?*, *Mon. Not. Roy. Astron. Soc.* **483** (2019) 289–298, [1807.06018].

[134] G. L. Bryan and M. L. Norman, *Statistical properties of x-ray clusters: Analytic and numerical comparisons*, *Astrophys. J.* **495** (1998) 80, [astro-ph/9710107].

[135] P.-H. Chavanis, *Mass-radius relation of Newtonian self-gravitating Bose-Einstein condensates with short-range interactions. I. Analytical results*, **84** (Aug., 2011) 043531, [1103.2050].

[136] R. Harrison, I. Moroz and K. P. Tod, *A numerical study of the Schrodinger-Newton equation 1: Perturbing the spherically-symmetric stationary states*, *arXiv e-prints* (Aug., 2002) math–ph/0208045, [math-ph/0208045].

[137] F. S. Guzman and L. A. Urena-Lopez, *Evolution of the Schrodinger-Newton system for a self-gravitating scalar field*, *Phys. Rev. D* **69** (2004) 124033, [gr-qc/0404014].

[138] S. Owusu and F. A. Brito, *Oscillating soliton stars with network of domain walls*, 1706.00406.

[139] A. W. McConnachie, *The Observed Properties of Dwarf Galaxies in and around the Local Group*, **144** (July, 2012) 4, [1204.1562].

[140] M. J. White, *The Mass of a halo*, *Astron. Astrophys.* **367** (2001) 27, [astro-ph/0011495].

[141] J.-W. Lee and S. Lim, *Minimum mass of galaxies from BEC or scalar field dark matter*, *JCAP* **01** (2010) 007, [0812.1342].

[142] J. M. Comerford, M. Meneghetti, M. Bartelmann and M. Schirmer, *Mass distributions ofHubble space TelescopeGalaxy clusters from gravitational arcs*, .

[143] P. Bull et al., *Beyond ΛCDM: Problems, solutions, and the road ahead*, *Phys. Dark Univ.* **12** (2016) 56–99, [1512.05356].

[144] J. E. Kim and G. Carosi, *Axions and the Strong CP Problem*, *Rev. Mod. Phys.* **82** (2010) 557–602, [0807.3125].

[145] D. J. E. Marsh and A.-R. Pop, *Axion dark matter, solitons and the cusp-core problem*, *Mon. Not. Roy. Astron. Soc.* **451** (2015) 2479–2492, [1502.03456].

[146] B. Schwabe, J. C. Niemeyer and J. F. Engels, *Simulations of solitonic core mergers in ultralight axion dark matter cosmologies*, *Phys. Rev.* **D94** (2016) 043513, [1606.05151].

[147] E. Madelung, *Eine anschauliche deutung der gleichung von schrödinger*, *Naturwissenschaften* **14** (Nov, 1926) 1004–1004.

[148] J. Zhang, Y.-L. S. Tsai, J.-L. Kuo, K. Cheung and M.-C. Chu, *Ultralight Axion Dark Matter and Its Impact on Dark Halo Structure in N-body Simulations*, *Astrophys. J.* **853** (2018) 51, [1611.00892].

[149] V. Springel, *The Cosmological simulation code GADGET-2*, *Mon. Not. Roy. Astron. Soc.* **364** (2005) 1105–1134, [astro-ph/0505010].

[150] "https://github.com/liambx/axion-gadget."

[151] M. Nori and M. Baldi, *AX-GADGET: a new code for cosmological simulations of Fuzzy Dark Matter and Axion models*, *Mon. Not. Roy. Astron. Soc.* **478** (2018) 3935, [1801.08144].

[152] P. Mocz and S. Succi, *Numerical solution of the nonlinear Schrödinger equation using smoothed-particle hydrodynamics*, *Phys. Rev.* **E91** (2015) 053304, [1503.03869].

[153] J. Veltmaat and J. C. Niemeyer, *Cosmological particle-in-cell simulations with ultralight axion dark matter*, *Phys. Rev.* **D94** (2016) 123523, [1608.00802].

[154] A. Almgren, J. Bell, M. Lijewski, Z. Lukic and E. Van Andel, *Nyx: A Massively Parallel AMR Code for Computational Cosmology*, *Astrophys. J.* **765** (2013) 39, [1301.4498].

[155] A. J. Benson, *Galacticus: A Semi-Analytic Model of Galaxy Formation*, *New Astron.* **17** (2012) 175–197, [1008.1786].

[156] X. Du, C. Behrens and J. C. Niemeyer, *Substructure of fuzzy dark matter haloes*, *Mon. Not. Roy. Astron. Soc.* **465** (2017) 941–951, [1608.02575].

[157] V. Springel, *E pur si muove: Galilean-invariant cosmological hydrodynamical simulations on a moving mesh*, *Mon. Not. Roy. Astron. Soc.* **401** (2010) 791, [0901.4107].

[158] P. Mocz, M. Vogelsberger, V. H. Robles, J. Zavala, M. Boylan-Kolchin, A. Fialkov et al., *Galaxy formation with BECDM - I. Turbulence and relaxation of idealized haloes*, *Mon. Not. Roy. Astron. Soc.* **471** (2017) 4559–4570, [1705.05845].

[159] H.-Y. Schive, Y.-C. Tsai and T. Chiueh, *GAMER: a GPU-Accelerated Adaptive Mesh Refinement Code for Astrophysics*, *Astrophys. J. Suppl.* **186** (2010) 457–484, [0907.3390].

[160] "https://github.com/gamer-project/gamer/wiki."

[161] F. M. Edwards, *On the stability of soliton cores of ultra-light axion-like dark matter haloes*, 2017.

[162] A. Paredes and H. Michinel, *Interference of Dark Matter Solitons and Galactic Offsets*, *Phys. Dark Univ.* **12** (2016) 50–55, [1512.05121].

[163] R. Easther, H. Finkel and N. Roth, *PSpectRe: A Pseudo-Spectral Code for (P)reheating*, *JCAP* **1010** (2010) 025, [1005.1921].

[164] M. A. Amin, R. Easther and H. Finkel, *Inflaton Fragmentation and Oscillon Formation in Three Dimensions*, *JCAP* **1012** (2010) 001, [1009.2505].

[165] M. A. Amin, R. Easther, H. Finkel, R. Flauger and M. P. Hertzberg, *Oscillons After Inflation*, *Phys. Rev. Lett.* **108** (2012) 241302, [1106.3335].

[166] S.-Y. Zhou, E. J. Copeland, R. Easther, H. Finkel, Z.-G. Mou and P. M. Saffin, *Gravitational Waves from Oscillon Preheating*, *JHEP* **10** (2013) 026, [1304.6094].

[167] "https://hgomersall.github.io/pyfftw/."

[168] M. Frigo and S. G. Johnson, "http://www.fftw.org/."

[169] N. Padmanabhan, E. Ronaghan, J. Zagorac and R. Easther, *Simulating ultralight dark matter in chapel*, in *2020 IEEE International Parallel and Distributed Processing Symposium Workshops (IPDPSW)*, (Los Alamitos, CA, USA), pp. 678–678, IEEE Computer Society, may, 2020. DOI.

[170] I. Dabo, B. Kozinsky, N. E. Singh-Miller and N. Marzari, *Electrostatics in periodic boundary conditions and real-space corrections*, *Phys. Rev. B* **77** (Mar, 2008) 115139.

[171] G. Agrawal, *Nonlinear Fiber Optics*. Optics and Photonics Series. Academic Press, 2013.

[172] Q. Zhang and M. I. Hayee, *Symmetrized split-step fourier scheme to control global simulation accuracy in fiber-optic communication systems*, *Journal of Lightwave Technology* **26** (Jan, 2008) 302–316.

[173] O. V. Sinkin, R. Holzlohner, J. Zweck and C. R. Menyuk, *Optimization of the split-step fourier method in modeling optical-fiber communications systems*, *Journal of Lightwave Technology* **21** (Jan, 2003) 61–68.

[174] M. Frigo and S. G. Johnson, *The design and implementation of FFTW3*, *Proceedings of the IEEE* **93** (2005) 216–231.

[175] "http://numexpr.readthedocs.io/."

[176] M. A. Ajaib, *Numerical Methods and Causality in Physics*, 1302.5601.

[177] T. R. Taha and M. J. Ablowitz, *Analytical and Numerical Aspects of Certain Nonlinear Evolution Equations. II. Numerical, Nonlinear Schrodinger Equation*, *J. Comput. Phys.* **55** (1984) 203–230.

[178] A. Suárez and T. Matos, *Structure Formation with Scalar Field Dark Matter: The Fluid Approach*, *Mon. Not. Roy. Astron. Soc.* **416** (2011) 87, [1101.4039].

[179] X. Du, B. Schwabe, J. C. Niemeyer and D. Bürger, *Tidal disruption of fuzzy dark matter subhalo cores*, *Phys. Rev.* **D97** (2018) 063507, [1801.04864].

[180] A. Suárez and P.-H. Chavanis, *Hydrodynamic representation of the Klein-Gordon-Einstein equations in the weak field limit*, *J. Phys. Conf. Ser.* **654** (2015) 012008, [1504.01164].

[181] R. Johnston, A. N. Lasenby and M. P. Hobson, *Cosmological fluid dynamics in the Schrödinger formalism*, 0904.0611.

[182] M. Kopp, K. Vattis and C. Skordis, *Solving the Vlasov equation in two spatial dimensions with the Schrödinger method*, *Phys. Rev.* **D96** (2017) 123532, [1711.00140].

[183] T. C. Wallstrom, *Inequivalence between the Schrodinger equation and the Madelung hydrodynamic equations*, *Phys. Rev.* **A49** (1994) 1613–1617.

[184] R. E. Wyatt, *Quantum Dynamics with Trajectories. Introduction to quantum hydrodynamics*, vol. 28. 2005, 10.1007/0-387-28145-2.

[185] S. Chandrasekhar, *The Equilibrum and the Stability of the Riemann Ellipsoids. I.*, *Astrophys. J.* **142** (Oct., 1965) 890.

[186] T. Rindler-Daller and P. R. Shapiro, *Angular Momentum and Vortex Formation in Bose-Einstein-Condensed Cold Dark Matter Haloes*, *Mon. Not. Roy. Astron. Soc.* **422** (2012) 135–161, [1106.1256].

[187] D. G. Levkov, A. G. Panin and I. I. Tkachev, *Gravitational Bose-Einstein condensation in the kinetic regime*, 1804.05857.

[188] B. Chamberlain, D. Callahan and H. Zima, *Parallel programmability and the chapel language*, *The International Journal of High Performance Computing Applications* **21** (2007) 291–312.

[189] J. L. Zagorac, E. Kendall, I. Sands, N. Padmanabhan and R. Easther, *Parametrizing ultralight dark matter halos through head-on binary soliton core mergers*, *(manuscript in preparation)* .

[190] Y. Wang and R. Easther, *Dynamical Friction From Ultralight Dark Matter*, 2110.03428.

[191] E. Y. Davies and P. Mocz, *Fuzzy dark matter soliton cores around supermassive black holes*, *Monthly Notices of the Royal Astronomical Society* **492** (01, 2020) 5721–5729.

[192] N. Glennon and C. Prescod-Weinstein, *Modifying PyUltraLight to model scalar dark matter with self-interactions*, *Phys. Rev. D* **104** (2021) 083532, [2011.09510].

[193] N. Musoke, S. Hotchkiss and R. Easther, *Lighting the Dark: Evolution of the Postinflationary Universe*, *Phys. Rev. Lett.* **124** (2020) 061301, [1909.11678].

[194] V. Springel et al., *Simulating the joint evolution of quasars, galaxies and their large-scale distribution*, *Nature* **435** (2005) 629–636, [astro-ph/0504097].

[195] Boomerang collaboration, P. de Bernardis et al., *A Flat universe from high resolution maps of the cosmic microwave background radiation*, *Nature* **404** (2000) 955–959, [astro-ph/0004404].

[196] S. Hanany et al., *MAXIMA-1: A Measurement of the cosmic microwave background anisotropy on angular scales of 10 arcminutes to 5 degrees*, *Astrophys. J.* **545** (2000) L5, [astro-ph/0005123].

[197] N. W. Halverson et al., *DASI first results: A Measurement of the cosmic microwave background angular power spectrum*, *Astrophys. J.* **568** (2002) 38–45, [astro-ph/0104489].

[198] Boomerang collaboration, C. B. Netterfield et al., *A measurement by Boomerang of multiple peaks in the angular power spectrum of the cosmic microwave background*, *Astrophys. J.* **571** (2002) 604–614, [astro-ph/0104460].

[199] A. T. Lee et al., *A High spatial resolution analysis of the MAXIMA-1 cosmic microwave background anisotropy data*, *Astrophys. J.* **561** (2001) L1–L6, [astro-ph/0104459].

[200] W. Hu and S. Dodelson, *Cosmic microwave background anisotropies*, *Ann. Rev. Astron. Astrophys.* **40** (2002) 171–216, [astro-ph/0110414].

[201] B. Moore, *Evidence against dissipationless dark matter from observations of galaxy haloes*, *Nature* **370** (1994) 629.

[202] A. A. Dutton, A. V. Macciò, T. Buck, K. L. Dixon, M. Blank and A. Obreja, *NIHAO XX: The impact of the star formation threshold on the cusp-core transformation of cold dark matter haloes*, 1811.10625.

[203] J. I. Read, M. G. Walker and P. Steger, *The case for a cold dark matter cusp in Draco*, *Mon. Not. Roy. Astron. Soc.* **481** (2018) 860–877, [1805.06934].

[204] A. Benitez-Llambay, C. S. Frenk, A. D. Ludlow and J. F. Navarro, *Baryon-induced dark matter cores in the EAGLE simulations*, *arXiv e-prints* (Oct, 2018) arXiv:1810.04186, [1810.04186].

[205] M. Schumann, *Direct Detection of WIMP Dark Matter: Concepts and Status*, 1903.03026.

[206] L. L. Watkins, R. P. van der Marel, S. T. Sohn and N. W. Evans, *Evidence for an Intermediate-mass Milky Way from Gaia DR2 Halo Globular Cluster Motions*, **873** (Mar., 2019) 118, [1804.11348].

[207] A. V. Maccio', A. A. Dutton and F. C. v. d. Bosch, *Concentration, Spin and Shape of Dark Matter Haloes as a Function of the Cosmological Model: WMAP1, WMAP3 and WMAP5 results*, *Mon. Not. Roy. Astron. Soc.* **391** (2008) 1940–1954, [0805.1926].

[208] D. Suto, T. Kitayama, K. Osato, S. Sasaki and Y. Suto, *Confrontation of Top-Hat Spherical Collapse against Dark Halos from Cosmological N-Body Simulations*, *Publ. Astron. Soc. Jap.* **68** (2016) 14, [1511.06935].

[209] D. Herrera, I. Waga and S. E. Jorás, *Calculation of the critical overdensity in the spherical-collapse approximation*, *Phys. Rev.* **D95** (2017) 064029, [1703.05824].

[210] J. Richings, C. Frenk, A. Jenkins and A. Robertson, *Subhalo destruction in the Apostle and Auriga simulations*, *arXiv e-prints* (Nov, 2018) arXiv:1811.12437, [1811.12437].

[211] A. D. Ludlow, J. F. Navarro, R. E. Angulo, M. Boylan-Kolchin, V. Springel, C. Frenk et al., *The mass–concentration–redshift relation of cold dark matter haloes*, *Mon. Not. Roy. Astron. Soc.* **441** (2014) 378–388, [1312.0945].

[212] A. Ragagnin, K. Dolag, L. Moscardini, A. Biviano and M. D'Onofrio, *Dependency of halo concentration on mass, redshift and fossilness in Magneticum hydrodynamic simulations*, 1810.08212.

[213] Y. Sofue, M. Honma and T. Omodaka, *Unified Rotation Curve of the Galaxy – Decomposition into de Vaucouleurs Bulge, Disk, Dark Halo, and the 9-kpc Rotation Dip –*, *Publ. Astron. Soc. Jap.* **61** (2009) 227, [0811.0859].

[214] L. Amendola and R. Barbieri, *Dark matter from an ultra-light pseudo-Goldsone-boson*, *Phys. Lett.* **B642** (2006) 192–196, [hep-ph/0509257].

[215] B. Bozek, D. J. E. Marsh, J. Silk and R. F. G. Wyse, *Galaxy UV-luminosity function and reionization constraints on axion dark matter*, *Mon. Not. Roy. Astron. Soc.* **450** (2015) 209–222, [1409.3544].

[216] E. Armengaud, N. Palanque-Delabrouille, C. Yèche, D. J. E. Marsh and J. Baur, *Constraining the mass of light bosonic dark matter using SDSS Lyman-α forest*, *Mon. Not. Roy. Astron. Soc.* **471** (2017) 4606–4614, [1703.09126].

[217] Y. Ni, M.-Y. Wang, Y. Feng and T. Di Matteo, *Predictions for the Abundance of High-redshift Galaxies in a Fuzzy Dark Matter Universe*, 1904.01604.

[218] O. Nebrin, R. Ghara and G. Mellema, *Fuzzy Dark Matter at Cosmic Dawn: New 21-cm Constraints*, *JCAP* **2019** (2020) 051, [1812.09760].

[219] A. R. Liddle, *How many cosmological parameters?*, *Mon. Not. Roy. Astron. Soc.* **351** (2004) L49–L53, [astro-ph/0401198].

[220] N. Bar, D. Blas, K. Blum and S. Sibiryakov, *Galactic rotation curves versus ultralight dark matter: Implications of the soliton-host halo relation*, *Phys. Rev.* **D98** (2018) 083027, [1805.00122].

[221] M. Castellano, N. Menci, A. Grazian, A. Merle, N. G. Sanchez, A. Schneider et al., *Constraining Dark Matter models with extremely distant galaxies*, in *Proceedings, Vulcano Workshop 2018: Frontier Objects in Astrophysics and Particle Physics: Vulcano Island, Sicily, Italy, May 20-26, 2018*, pp. 200–213, 2018. 1903.12580.

[222] A. Lidz and L. Hui, *Implications of a prereionization 21-cm absorption signal for fuzzy dark matter*, *Phys. Rev.* **D98** (2018) 023011, [1805.01253].

[223] H. Davoudiasl and P. B. Denton, *Ultra Light Boson Dark Matter and Event Horizon Telescope Observations of M87**, 1904.09242.

[224] J. D. Simon et al., *Testing the Nature of Dark Matter with Extremely Large Telescopes*, 1903.04742.

[225] S.-C. Lin, H.-Y. Schive, S.-K. Wong and T. Chiueh, *Self-consistent construction of virialized wave dark matter halos*, *Phys. Rev.* **D97** (2018) 103523, [1801.02320].

[226] K. Clough, T. Dietrich and J. C. Niemeyer, *Axion star collisions with black holes and neutron stars in full 3D numerical relativity*, *Phys. Rev.* **D98** (2018) 083020, [1808.04668].

[227] H. Y. J. Chan, E. G. M. Ferreira, S. May, K. Hayashi and M. Chiba, *The Diversity of Core Halo Structure in the Fuzzy Dark Matter Model*, 2110.11882.

[228] R. Genzel, S. H. Price, H. Übler, N. M. Förster Schreiber, T. T. Shimizu, L. J. Tacconi et al., *Rotation Curves in $z \sim$ 1-2 Star-forming Disks: Evidence for Cored Dark Matter Distributions*, **902** (Oct., 2020) 98, [2006.03046].

[229] D. Dutta Chowdhury, F. C. van den Bosch, V. H. Robles, P. van Dokkum, H.-Y. Schive, T. Chiueh et al., *On the Random Motion of Nuclear Objects in a Fuzzy Dark Matter Halo*, **916** (July, 2021) 27, [2105.05268].

[230] B. T. Chiang, H.-Y. Schive and T. Chiueh, *Soliton Oscillations and Revised Constraints from Eridanus II of Fuzzy Dark Matter*, *Phys. Rev. D* **103** (2021) 103019, [2104.13359].

[231] B. Schwabe and J. C. Niemeyer, *Deep zoom-in simulation of a fuzzy dark matter galactic halo*, 2110.09145.

[232] L. E. Padilla, T. Rindler-Daller, P. R. Shapiro, T. Matos and J. A. Vázquez, *Core-halo mass relation in scalar field dark matter models and its consequences for the formation of supermassive black holes*, *Phys. Rev. D* **103** (Mar, 2021) 063012.

[233] A. Burkert, *Fuzzy Dark Matter and Dark Matter Halo Cores*, **904** (Dec., 2020) 161, [2006.11111].

[234] the AMReX Development Team, A. Almgren, V. Beckner, J. Blaschke, C. Chan, M. Day et al., *Amrex-codes/amrex: Amrex 21.10*, Oct., 2021. 10.5281/zenodo.5544070.

[235] A. Mead, *Spherical collapse, formation hysteresis and the deeply non-linear cosmological power spectrum*, *Mon. Not. Roy. Astron. Soc.* **464** (2017) 1282–1293, [1606.05345].

[236] Ya. B. Zeldovich, *Gravitational instability: An Approximate theory for large density perturbations*, *Astron. Astrophys.* **5** (1970) 84–89.

[237] J. L. Zagorac, I. Sands, N. Padmanabhan and R. Easther, *Schrödinger-Poisson Solitons: Perturbation Theory*, 2109.01920.

[238] J. C. Niemeyer, *Small-scale structure of fuzzy and axion-like dark matter*, 1912.07064.

[239] X. Li, L. Hui and T. D. Yavetz, *Oscillations and Random Walk of the Soliton Core in a Fuzzy Dark Matter Halo*, *Phys. Rev. D* **103** (2021) 023508, [2011.11416].

[240] J. Veltmaat, B. Schwabe and J. C. Niemeyer, *Baryon-driven growth of solitonic cores in fuzzy dark matter halos*, *Phys. Rev. D* **101** (Apr, 2020) 083518.

[241] J. I. Read, G. Iorio, O. Agertz and F. Fraternali, *Understanding the shape and diversity of dwarf galaxy rotation curves in CDM*, *Monthly Notices of the Royal Astronomical Society* **462** (07, 2016) 3628–3645.

[242] A. D. Ludlow, M. Borzyszkowski and C. Porciani, *The formation of CDM haloes – I. Collapse thresholds and the ellipsoidal collapse model*, *Monthly Notices of the Royal Astronomical Society* **445** (11, 2014) 4110–4123.

[243] H.-Y. Schive, T. Chiueh and T. Broadhurst, *Soliton random walk and the cluster-stripping problem in ultralight dark matter*, *Phys. Rev. Lett.* **124** (May, 2020) 201301.

[244] P. Mocz et al., *First star-forming structures in fuzzy cosmic filaments*, *Phys. Rev. Lett.* **123** (2019) 141301, [1910.01653].

[245] J. Shim, S. Codis, C. Pichon, D. Pogosyan and C. Cadiou, *The clustering of critical points in the evolving cosmic web*, *Mon. Not. Roy. Astron. Soc.* **502** (2021) 3885–3910, [2011.04321].

[246] A. Mead, S. Brieden, T. Tröster and C. Heymans, *HMcode-2020: Improved modelling of non-linear cosmological power spectra with baryonic feedback*, 2009.01858.

[247] Euclid collaboration, M. Knabenhans et al., *Euclid preparation: II. The EuclidEmulator – A tool to compute the cosmology dependence of the nonlinear matter power spectrum*, *Mon. Not. Roy. Astron. Soc.* **484** (2019) 5509–5529, [1809.04695].

[248] M. Buehlmann and O. Hahn, *Large-Scale Velocity Dispersion and the Cosmic Web*, *Mon. Not. Roy. Astron. Soc.* **487** (2019) 228–245, [1812.07489].

[249] J. Lee, O. Hahn and C. Porciani, *The Anisotropic Two-Point Correlation Functions of the Nonlinear Traceless Tidal Field in the Principal-Axis Frame*, *Astrophys. J.* **705** (2009) 1469–1472, [0906.5163].

[250] J. Harnois-Déraps, N. Martinet and R. Reischke, *Cosmic shear beyond 2-point statistics: Accounting for galaxy intrinsic alignment with projected tidal fields*, 2107.08041.

[251] I. CATTO, J. DOLBEAULT, O. SÁNCHEZ and J. SOLER, *Existence of steady states for the maxwell–schrÖdinger–poisson system: Exploring the applicability of the concentration–compactness principle*, *Mathematical Models and Methods in Applied Sciences* **23** (2013) 1915–1938.

[252] M. Nori and M. Baldi, *Scaling relations of fuzzy dark matter haloes – I. Individual systems in their cosmological environment*, *Mon. Not. Roy. Astron. Soc.* **501** (2021) 1539–1556, [2007.01316].